Linköping Studies in Science and Technology
Thesis No. 1463

Compressor Modeling for Control of Automotive Two Stage Turbochargers

Oskar Leufvén

Linköpings universitet
INSTITUTE OF TECHNOLOGY

Department of Electrical Engineering
Linköpings universitet, SE–581 83 Linköping, Sweden

Linköping 2010

Compressor Modeling for Control of Automotive Two Stage Turbochargers

oleufven@isy.liu.se
http://www.vehicular.isy.liu.se
Department of Electrical Engineering
Linköpings universitet
SE–581 83 Linköping
Sweden.

ISBN ISBN 978-91-7393-254-7
ISSN 0280-7971
LIU-TEK-LIC-2010:32

Typeset with LaTeX 2ε
Printed by LiU-Tryck, Linköping, Sweden 2010

Abstract

There is a demand for increasing efficiency of automotive engines, and one way to achieve this is through downsizing and turbocharging. In the design compromises are made, for example the maximum power of the engine determines the size of the compressor, but since the compressor mass flow range is limited, this affects the torque for low engine speeds. A two stage system, with two different sized turbochargers, reduces this compromise, but the system complexity increases. To handle the complexity, models have come to play a central role where they aid engineers in the design. Models are used in simulation, for design optimization and also in the control synthesis. In all applications it is vital that the models have good descriptive capabilities for the entire operating range studied.

A novel control oriented compressor model is developed, with good performance in the operating regions relevant for compressors in a two stage system. In addition to the nominal operating regime, also surge, choke and operation at pressure ratios less than unity, are modeled. The model structure can be automatically parametrized using a compressor map, and is based on static functions for low computational cost. A sensitivity analysis, isolating the important characteristics that influence surge transients in an engine is performed, and the gains of a novel surge controller are quantified.

A compressor map is usually measured in a gas stand, that has different surrounding systems, compared to the application where the compressor is used. A method to automatically determine a turbo map, when the turbo is installed on an engine in an engine test stand is developed. The map can then be used to parametrize the developed compressor model, and effectively create a model parametrized for its intended application.

An experimental analysis of the applicability of the commonly used correction factors, used for estimating compressor performance when the inlet conditions deviate from nominal, is presented. Correction factors are vital, to e.g. estimate turbocharger performance for driving at high altitude or to analyze second stage compressor performance, where the variations in inlet conditions are large. The experimental campaign uses measurements from an engine test cell and from a gas stand, and shows a small, but clearly measurable trend, with decreasing compressor pressure ratio for decreasing compressor inlet pressure, for points with equal corrected shaft speed and corrected mass flow. A method is developed, enabling measurements to be analyzed with modified corrections. An adjusted shaft speed correction quantity is proposed, incorporating also the inlet pressure in the shaft speed correction. A high altitude example is used to quantify the influence of the modified correction.

Acknowledgment

I first of all want to express my grateful gratitude to my supervisor Lars Eriksson for all valuable input and appreciated discussions during the last three years work: master thesis, licentiate thesis, and the long hours spent with the papers. It was also nice to get to know you personally, and our unintentional US tour, due to the Icelandic volcano, together with Andreas Thomasson is a memory I will carry with me.

Lars Nielsen is gratefully acknowledged for letting me join the Vehicular Systems group. The whole Vehicular Systems group deserves a place in this acknowledgment, for creating a nice and pleasant atmosphere, not only during the work hours. If you want to lose more poker money, or be beaten in "Folkrace", just let me know. Erik Frisk, Per Öberg and Erik Hellström are acknowledged for their never ending computer support.

I also thank the LNF engine for providing me with large amounts of measurement data, even though I ran you "slightly" boosted without the coolant line turned on... The industrial support with both hardware, software and knowledge is also acknowledged: Per Andersson, Ragnar Burenius, Patrik Martinsson, Per-Inge Larsson, Mikael Gellerstedt, Mika Heinonen, Richard Backman, and Jonas Dyrssen. Elbert Hendricks is acknowledged for his support with the LFE3. Tobias Lindell is acknowledged for help with all measurements, and Kristoffer Lundahl for his services as a research engineer.

Jonas Cornelsen is greatly acknowledged for all invaluable support for the rapid prototyping control system. Johannes Andersen is acknowledged for supplying me with engine map data, during my year as international student in Austria, a time when I did not even know what an engine map was. The spark you ignited started my research engine, and here I am now. It was also a pleasant surprise to randomly meet you a couple of years later on, and to be able to thank you in person.

Thanks also goes to Erik Höckerdal and Christofer Sundström for proofreading this licentiate thesis manuscript. "Höckis" is further acknowledged for have been fooled into joining Slätmons BK, so that I had someone to share the 40 km single way trip with, to the trainings and games. Mr "Sundtsröm" also deserves a special acknowledgment for the never ending stream of questions and discussions of any form, shape and contents, that we have had over the past two years.

My love goes to you Maria, for always being here with me, and for your endless support and encouragement.

Contents

Introduction to combustion engine turbocharging

1

Introduction

Combustion engines have for a long time been the most important prime mover for transportation globally. A combustion engine is simple in its nature; a mix of fuel and air is combusted, and work is produced in the operating cycle.

> "Air, fuel, compression and a spark, and it should start."[†]

The amount of combusted air and fuel controls the amount of work the engine produces. The engine work has to overcome friction and pumping losses, and a smaller engine has smaller losses and is therefore more efficient. Increasing engine efficiency in this way is commonly referred to as downsizing. Downsizing has an important disadvantage; a smaller engine can not take in as much air and fuel as a larger one, and is therefore less powerful, which can lead to less customer acceptance. By increasing the charge density the smaller engine can be given the power of a larger engine, and regain customer acceptance. A number of charging systems can be used for automotive application, e.g. supercharging, pressure wave charging or turbocharging. Turbocharging has become the most commonly used charging system, since it is a reliable and robust system, that utilizes some of the energy in exhaust gas, otherwise lost to the surroundings. It is outside the scope of this thesis to give a comprehensive summary of basic engine operations and the interested reader is referred to [1, 2, 3].

There are however some drawbacks and limits of a turbo. The compressor of a single stage turbo system is sized after the maximum engine power, which is tightly coupled to the maximum mass flow. The mass flow range of a compressor is limited, which imposes limits on the pressure build up for small mass flows and thereby engine torque at low engine speed. Further, a turbo needs to spin with high rotational speed to increase air density, and due to the turbo inertia it takes time to spin up the turbo. This means that the torque response of

[†]Free translation from a seminar, held in Swedish by Per Gillbrand.

a turbocharged engine is slower than an equally powerful naturally aspirated engine, which also lead to less customer acceptance.

A two stage turbo system combines two different sized turbo units, where the smaller mass flow range of the smaller unit, means that pressure can be increased for smaller mass flows. Further, due to the smaller inertia of the smaller unit, it can be spun up faster and thereby speed up the torque response of the engine. The smaller unit can then be bypassed for larger mass flows, where instead the larger turbo unit is used to supply the charge density needed [4, 5]. A brief summary of the most important turbo characteristics, is found in Chapter 2, and the more interested reader is referred to [6, 7].

The use of two turbochargers adds actuators and complexity to the engine system. This illustrates that in the process of designing more efficient engines, they are made more flexible to reduce design trade-offs and enable optimization. As a side effect, this also increases the system complexity, and models are used as the foundation for concept development and implementation of control systems, that meet the increased demand for engine performance combined with increasingly stringent emission legislation. To be useful it is vital that the models have good descriptive capabilities over the relevant operating range. Development and validation of control oriented compressor models for two stage systems, is the scope of this thesis, and Chapter 3 presents related research in the compressor modeling area.

1.1 Contributions

Paper 1 [8] extends a mean value engine modeling framework, with surge description capability. A sensitivity analysis is performed, showing the important characteristics that influence surge properties in an engine. This knowledge is used in the design of a novel surge controller, that avoids surge and improves the vehicle acceleration performance.

Paper 2 [9] contributes with a method for determining turbocharger performance on engine test bench installations. An analysis of the limits that an engine installation imposes on the reachable points in the compressor map is performed, in particular it shows what these limits depend on. The novel use of a throttle before the compressor is proposed, enabling the engine system to span a larger region in corrected flow. An engine and test cell control structure, that can be used to automate and monitor the measurements by controlling the system to the desired operating points, is also proposed. Two methods that compensate for the deviation between measured and desired speed are proposed and investigated.

The contribution in Paper 3 [10] is the development of a compressor model, capable of representing mass flow and pressure characteristic for three different regions: surge, normal operation, as well as for when the compressor acts as a restriction. Both the parametrization and validation are supported by measured data. The proposed model is shown to have good agreement with measured data for all regions, without the need for extensive geometric information or data.

An analysis of the corrections used to scale compressor performance for varying inlet conditions is presented in Paper 4 [11]. A novel surge avoidance strategy is proposed, where the result is that a reduction in inlet pressure can

increase the surge margin. The method to investigate the applicability of the strategy is straight forward and general. An experimental analysis of the correction factors, commonly used to determine compressor performance when inlet conditions deviate from nominal conditions, is then presented. Experimental data from an engine test cell and a gas stand shows a small, but clearly measurable trend, with decreasing compressor pressure ratio for decreasing compressor inlet pressure. A method is developed, enabling measurements to be analyzed with modified corrections. An adjusted shaft speed correction quantity is proposed, incorporating also the inlet pressure in the shaft speed correction.

1.2 Future work

This section briefly presents continuations of this thesis, or research topics that have been found along the way, but that did not gain the deserved attention due to the time constraints.

A turbocharger consists of two main parts, a compressor and a turbine, and a natural continuation of this thesis is therefore found in its title. To evaluate and validate control oriented turbine models, can be motivated by the development and increased use of twin scroll turbines, mixed flow turbines, variable geometry or variable nozzle turbines.

To investigate and evaluate observer designs based on the developed compressor models is also an interesting continuation. To accurately know the two stage system states, e.g. pressures, temperatures and turbo speeds, is important for a controller. Especially to estimate the shaft speed of the bypassed high pressure stage is an interesting scope. This is important for transients involving a stage switch, where the charging effort is transferred from one of the stages to the other. Further investigation of shaft friction can be motivated by experimental experience from the engine test stand, where the bypassed second stage sometimes stops in friction. For transient two stage control, it is important for the controller to know the shaft speed of the turbos; if the high pressure turbo has stopped or is rotating along in 30.000 rpm is then vital information.

Diagnosis and supervision of the actuator system of the two stage system is also interesting, e.g. to supervise the high pressure stage bypass valve. Such a path would include evaluation and actuator modeling, which is also beneficial for control purposes. To use a model based feed-forward term to remove a difficult non linearity of a system, has been successfully used in many applications. Also diagnostic and modeling of automotive sensors is an interesting path. To be able to measure accurately, and to trust the measurement reading is the foundation for any feedback control.

More measurements of turbo performance for larger variations in inlet conditions, and for more units, compared to the reference conditions, is also a research scope. Such an investigation is also closely coupled to interesting investigations of how engine system geometries and properties affect both compressor and turbine performance, compared to the gas stand measured maps.

2

Turbo and experimental setup

This chapter starts with a description of the main components of a turbo, followed by a presentation of turbo maps and the correction equations, used to adjust turbo performance to inlet conditions that deviate from the conditions used when the map was measured. The last section presents the experimental setup used in Paper 2 and in Paper 4.

2.1 Main components of a turbo

An automotive turbo consists of a compressor and a turbine on a common shaft, supported by bearings in a center housing. An example of a turbo is shown in Figure 2.1, where some of the important parts are marked. The turbo extracts some of the energy in the exhaust gas, and transfers this as power to the compressor. The compressor increases the intake air density, and thereby the engine power.

2.1.1 Compressor

Almost all automotive compressors are centrifugal compressors. They are referred to as centrifugal, or radial compressors since the air enters axially, but leaves the compressor impeller in the radial direction. Axial compressors also exist, but are used mainly in e.g. aircraft or power generation applications.

The air is collected in the compressor inlet, and lead to the first part of the impeller, referred to as the inducer section. The impeller consists of many impeller vanes, that rotate at a high velocity and transfers energy to the air. The maximum shaft velocity of an automotive turbo is approximately 200.000 rpm. The transferred energy increases the air velocity and thereby the kinetic energy. The air then leaves the compressor impeller in the radial and tangential

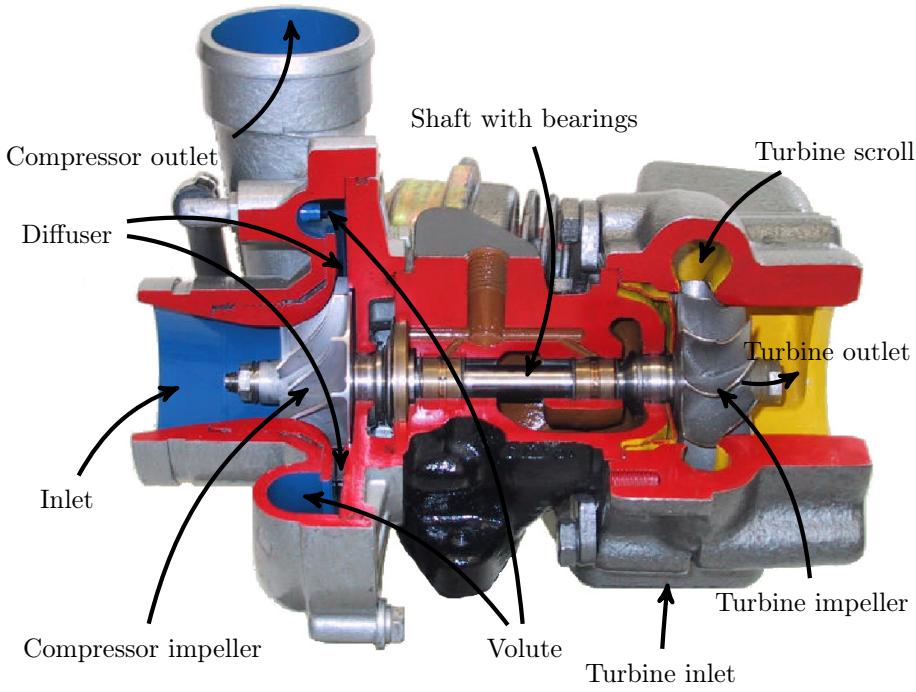

Figure 2.1: Picture of a turbo. The air enters the compressor through the inlet (left) and through the impeller. The heated and pressurized air is then collected in the volute and delivered to the outlet connection (up). The exhaust gas enters the turbine through the turbine inlet (hidden behind the turbo), is lead through the volute into the impeller, where energy is transferred to the impeller vanes and then exits through the outlet (right).

direction. The kinetic energy is partly converted into potential energy in the impeller passages, and partly in the diffuser section when the air is decelerated. Both air pressure and temperature increase in the compression process. The temperature increase is inevitable but undesired, since an increase in temperature decreases the air density. The air with increased pressure and temperature leaves the diffuser section and is collected in the volute, that leads the air to the compressor outlet connection.

A valve can be mounted in close connection to the compressor. This valve is referred to as a surge or recirculation valve, and is used to decrease the pressure after the compressor. The valve opens a connection from the pipes after the compressor to the pipes before, to avoid compressor surge, that is described in Section 2.2.1. Control of the surge valve is connected to engine performance, and is studied in Paper 1. How a compressor can be modeled is presented in Chapter 3.

2.1.2 Housing and bearings

The bearings of the turbo shaft are mounted in the center housing of the turbo, and are critical components, needed to support the shaft at high speeds. Fluid bearings and ball bearings are commonly used, and are supplied with oil to reduce friction. The oil supplied, or additional water cooling, is used to cool the turbo. Turbo bearing friction is analyzed and measured e.g in [12], and modeled e.g in [13]. The effect of the heat transfer in an automotive turbo system is analyzed e.g. in [14, 15, 16, 17].

2.1.3 Turbine

The turbine recycles some of the otherwise lost energy from the hot exhaust gas of the combustion engine. The exhaust gas flows through a turbine impeller, where energy is extracted and transferred to the compressor side. A waste gate valve is commonly used to control the amount of exhaust gas that flows through the turbine, and thereby the turbine power. Some turbines use a variable nozzle, or a variable geometry, to control the turbine power, instead of a waste gate. These actuators effectively change the flow geometry within the turbine.

Turbine performance measurements and analysis is presented e.g. in [18] and models of the turbine can be found e.g. in [13, 19].

2.2 Turbo maps

Turbo performance is usually presented in maps using corrected performance variables. The corrections are important, since the performance maps are otherwise only valid for the conditions under which they were measured. The basis for the corrections is dimensional analysis [20], and the correction equations relevant for turbochargers are presented e.g. in [7, 21, 22]. The correction equations scale the turbine and compressor performance variables, based on the current inlet temperature and pressure. An experimental investigation of the correction quantities for the compressor is presented in Paper 4.

There are standards describing the procedures involved in measuring a turbo map, see e.g. [23, 24, 25, 26]. The definition of when surge occurs, which gives the smallest mass flow point for a corrected compressor speed, have been discussed in recent works [27, 28]. A summary of some different turbocharger test facilities is presented in [27]. Methodology to measure turbo performance on an engine in a test stand is presented in Paper 2.

2.2.1 Compressor map

There are four performance variables for the compressor map: corrected mass flow, pressure ratio, corrected shaft speed and adiabatic efficiency. The *corrected compressor mass flow* is given by

$$\dot{m}_{c,corr} = \dot{m}_c \frac{\sqrt{\frac{T_{01}}{T_{c,std}}}}{\frac{p_{01}}{p_{c,std}}} \quad [\text{kg/s}] \tag{2.1}$$

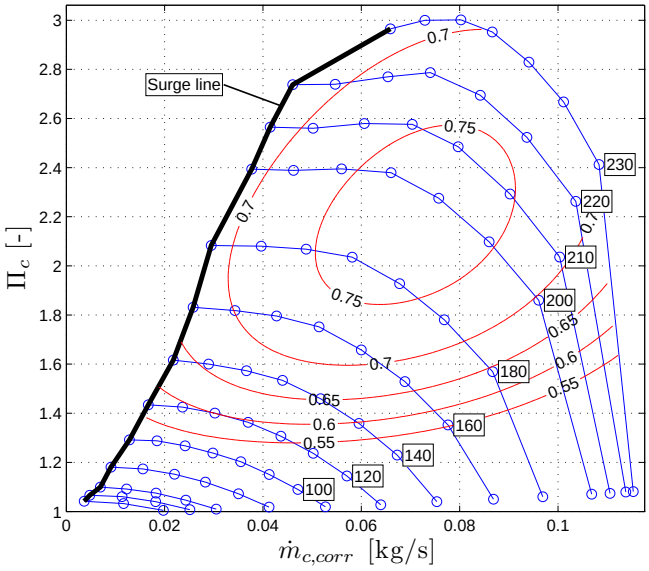

Figure 2.2: Example of a compressor map. The numbers in boxes indicate corrected shaft speeds in krpm, i.e 180 means 180000 rpm. Circles indicate measured points, and the contours represent the adiabatic efficiency. The surge line is also marked.

where $\dot{m}_c$ [kg/s] is the compressor mass flow, T_{01} [K] is the compressor inlet temperature, and p_{01} [Pa] is the compressor inlet pressure. The temperature $T_{c,std}$ [K] and the pressure $p_{c,std}$ [Pa] are the reference states. The reference states must be supplied with the compressor map, since these states are used to correct the performance variables. The *compressor pressure ratio* is given by

$$\Pi_c = \frac{p_{02}}{p_{01}} \quad [\text{-}] \tag{2.2}$$

where p_{02} [Pa] is the compressor outlet pressure. The *corrected shaft speed* is defined as

$$N_{c,corr} = N_{tc} \frac{1}{\sqrt{\frac{T_{01}}{T_{c,std}}}} \quad [\text{rpm}] \tag{2.3}$$

where N_{tc} is the turbo shaft speed. The *adiabatic efficiency* of the compressor

$$\eta_c = \frac{\left(\frac{p_{02}}{p_{01}}\right)^{\frac{\gamma_c - 1}{\gamma_c}} - 1}{\frac{T_{02}}{T_{01}} - 1} \quad [\text{-}] \tag{2.4}$$

where γ_c [-] is the ratio of specific heats for air. The adiabatic efficiency describes how efficient the compression of the gas is, compared to an ideal adiabatic process. Or in other words, how much the pressure increases, compared to how much the temperature increases.

Points measured with equal $N_{c,corr}$ are connected in the compressor map, and are referred to as speed lines. A speed line consists of a number of measure-

ments of Π_c and $\dot{m}_{c,corr}$, and gives the characteristics of the compressor. Compressor efficiency η_c is also measured for each point, and contours of constant η_c are normally superimposed over the speed lines. The mass flows measured on each speed line range from the surge line into the choke region. An example of a compressor map is shown in Figure 2.2.

The surge line is the boundary of stable operation of the compressor. A compressor will enter surge if the mass flow is reduced below this point. Surge is an unstable condition, where the mass flow oscillates. These oscillations can destroy the turbo. Compressor choke is found for high mass flows, and indicates that the speed of sound is reached in some part of the compressor. Measurements are conducted at different $N_{c,corr}$ up to the maximum allowable, and mechanical failure of the turbo can result if the speed is increased further.

2.2.2 Turbine map

As for the compressor map, there are four performance variables used in the turbine performance map: corrected mass flow, expansion ratio, corrected speed and adiabatic efficiency. It is further common to define two more variables for the turbine: turbine flow parameter and turbine speed parameter. The *corrected turbine mass flow* is given by

$$\dot{m}_{t,corr} = \dot{m}_t \frac{\sqrt{\frac{T_{03}}{T_{t,std}}}}{\frac{p_{03}}{p_{t,std}}} \quad [\text{kg/s}] \tag{2.5}$$

where $T_{t,std}$ [K] and $p_{t,std}$ [Pa] can be other standard states, than are used in the compressor map. The turbine mass flow $\dot{m}_t$ [kg/s], is the combustion products and thus normally the sum of fuel and air. The pressures p_{03} [Pa] and p_{04} [Pa] are the turbine inlet and outlet pressure, respectively, and T_{03} [K] and T_{04} [K] are the turbine inlet and outlet temperature, respectively. It is common to neglect the standard states in (2.5), and present turbine data using the *turbine flow parameter*, or TFP

$$\text{TFP} = \dot{m}_t \frac{\sqrt{T_{03}}}{p_{03}} \quad [\text{kg } \sqrt{\text{K}}/\text{ s kPa}] \tag{2.6}$$

where p_{03} is usually in [kPa], as indicated by the unit of (2.6). The *turbine expansion ratio* is given by

$$\Pi_t = \frac{p_{03}}{p_{04}} \quad [\text{-}] \tag{2.7}$$

Some authors prefer to have the pressure after the component divided by the pressure before, as is the case for the compressor pressure ratio (2.2). The *corrected turbine shaft speed* is given by

$$N_{t,corr} = N_{tc} \frac{1}{\sqrt{\frac{T_{03}}{T_{t,std}}}} \quad [\text{rpm}] \tag{2.8}$$

It is common to neglect T_{std} in (2.8) and define the *turbine speed parameter*, or TSP as

$$\text{TSP} = N_{tc} \frac{1}{\sqrt{T_{03}}} \quad [\text{rpm}/\text{K}^{0.5}] \tag{2.9}$$

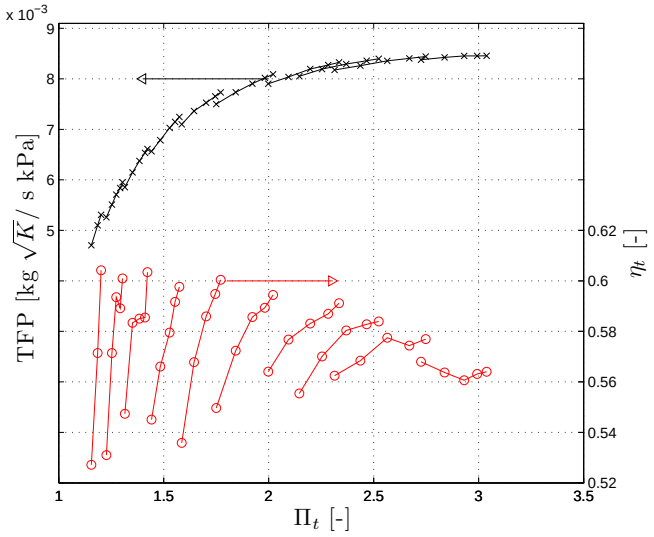

Figure 2.3: Example of a turbine map. Circle is the turbine adiabatic efficiency, and cross is the turbine flow parameter.

Since p_{std} and T_{std} are constants, neglecting them in equations (2.5) and (2.8) to give equations (2.6) and (2.9) respectively, gives only a scaling. The *adiabatic efficiency* of the turbine is given by

$$\eta_t = \frac{1 - \frac{T_{03}}{T_{04}}}{1 - \left(\frac{p_{04}}{p_{03}}\right)^{\frac{\gamma_t - 1}{\gamma_t}}} \quad [\text{-}] \tag{2.10}$$

where γ_t [-] is the ratio of specific heats for the exhaust gas.

The high temperatures on the turbine side cause large heat fluxes. Measurement of T_{04} can have substantial systematic errors, due to the heat fluxes. An alternative efficiency definition for the turbine side is therefore commonly used, where no measurement of T_{04} is needed. The heat transfer effects are less pronounced on the compressor side, and the compressor power

$$P_c = \dot{m}_c \cdot c_p \left(T_{02} - T_{01}\right) \tag{2.11}$$

can be used to define an alternative efficiency. This alternative turbine efficiency definition includes the shaft friction, and the equation is

$$\tilde{\eta}_t = \eta_t \cdot \eta_m = \frac{\dot{m}_c c_{p,c} \left(T_{02} - T_{01}\right)}{\dot{m}_t c_{p,t} T_{03} \left(1 - \left(\frac{p_{04}}{p_{03}}\right)^{\frac{\gamma_t - 1}{\gamma_t}}\right)} \tag{2.12}$$

where the shaft friction is included in the mechanical efficiency η_m. Figure 2.3 shows an example of a turbine map.

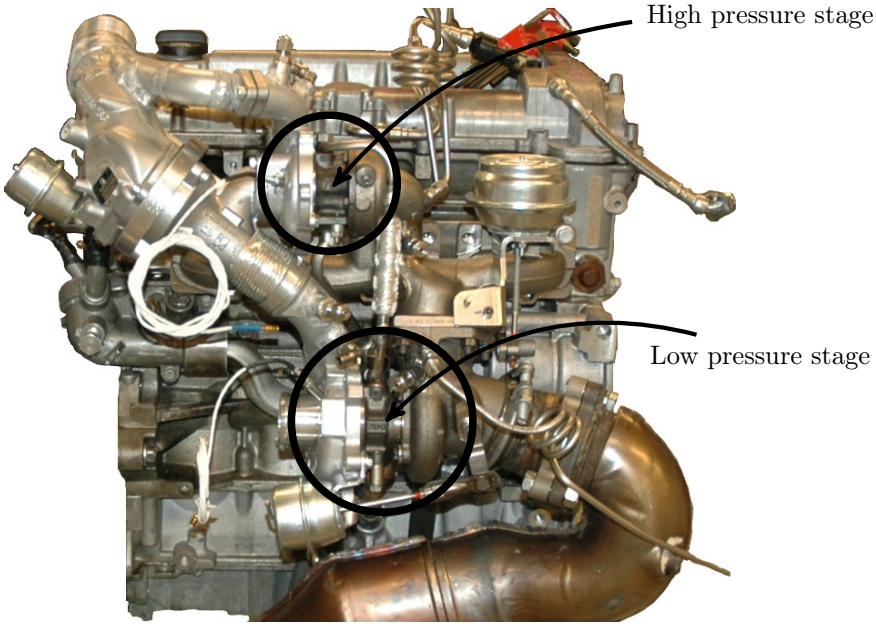

Figure 2.4: Photo of the engine with the two stage system.

2.3 Experimental setup

This section describes the experimental setup used for the measurements presented in Paper 2 and in Paper 4. The experimental setup varied slightly between the measurements, but most parts were kept intact. The experimental setup used in Paper 1 and in Paper 3 is described in [13].

2.3.1 Engine, dynamometer and measurement systems

The base line engine is a GM LNF, and is a four cylinder, SI DI 2.0 liter gasoline engine. It has a rated power of approximately 190 kW (260 hp), and a rated torque of 350 Nm. The original single stage turbocharger is exchanged for a two stage system, see Figure 2.4. The maximum power of the engine, using the two stage system, is reduced. This since the largest compressor of the two stage system is smaller than the single stage system compressor, as discussed in Chapter 1. The engine control system is based on a dSPACE MicroAutoBox and RapidPro architecture. The control system is built around a Simulink model. The model is compiled using Real Time Workshop, and executed in real time on the MicroAutoBox.

The dynamometer is a Schenck Dynas3 LI 250. The rated speed of the dynamometer is 10000 rpm, the rated power 250 kW and the rated torque 480 Nm. The dynamometer also acts as the start motor for the engine. The electricity the dynamometer generates, is fed back to the electric grid, and the heat expelled by the engine to the coolant system, supports the heating of the university buildings.

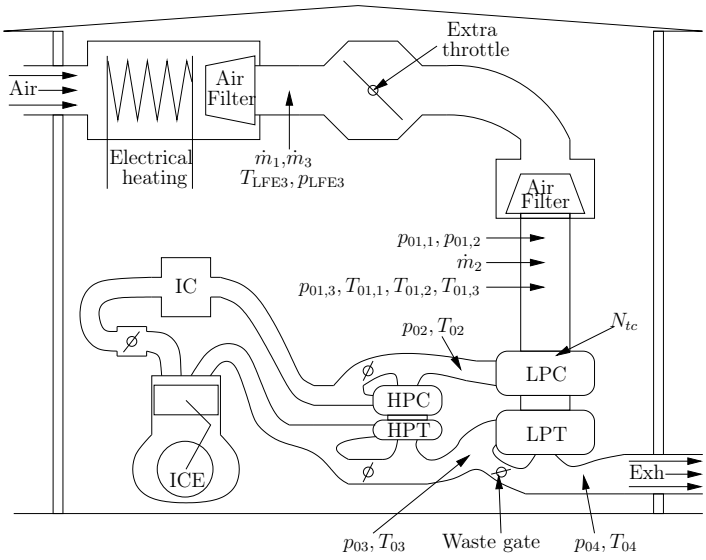

Figure 2.5: Schematic picture of the experimental setup. The electrical heating section is removed when not required. The extra throttle is used to decrease compressor inlet pressure. The air filters are used to straighten the air flow for the mass flow and pressure measurement locations. Air comes in from the left, runs through the compressor inlet variation rig, goes through the compressor stages, the engine, the turbine stages, catalyst, muffler and are expelled to the right.

The test cell measurement system consists of a HP VXi system, with a HPE1415A module and a HPE1433A module. The HPE1415A module is used to measure analog and digital signals, with a sample frequency of up to 2000 Hz, and has built in support for thermocouples. The HPE1433A module is a fast 8 channel converter with separate A/D-converters for each channel. It is used with sampling frequencies of up to 192 kHz, and can also be used to sample in the crank angle domain.

The signals are measured by the HP VXi system, where the most important signals are measured with both the HPE1415A and the HPE1433A modules. A sampling frequency of 1000 Hz is used for the HPE1415A and 128 kHz is used on the HPE1433A.

2.3.2 Sensors

Temperature

All temperature sensors are K-type thermocouples from Pentronic. A sensor width of 1.5 mm is used for T_{02}, and 3 mm sensor widths are used for $T_{01,1}$, $T_{01,2}$, $T_{01,3}$, T_{03} and T_{04}. The temperature sensor T_{LFE3} is used by the LFE3 mass flow sensor, and is also 3 mm in width.

The recovery factor, used to calculate the total temperature from a measured temperature [25], is assumed to be 1. This means that the measured temper-

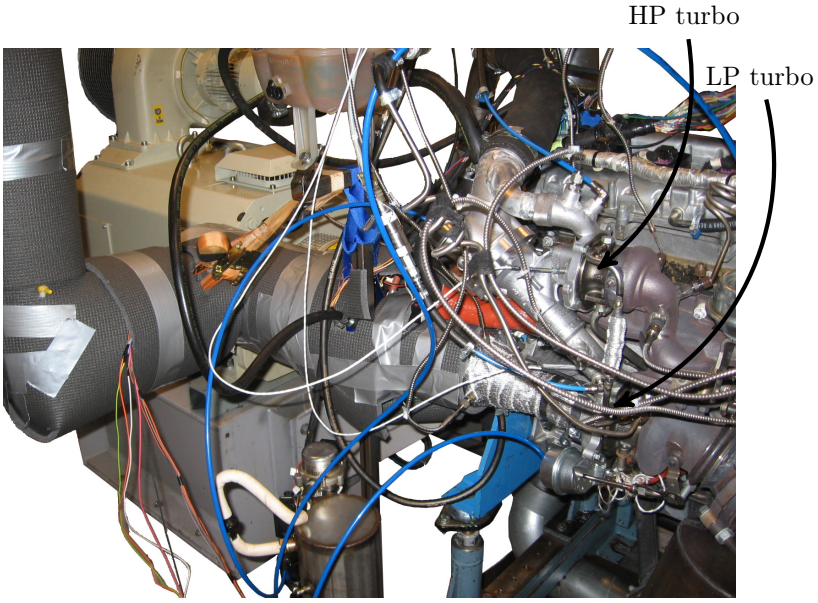

Figure 2.6: Photo from the engine test cell, showing the compressor inlet condition variation rig, the Schenk dynamometer and the engine test stand with the two stage system mounted to the LNF engine. The high pressure turbo (HP) and the low pressure turbo (LP) are marked.

ature is assumed to be the total temperature. Ice water and boiling water are used to calibrate the temperature sensors, before the measurement series.

The sensor width introduces dynamic to the measured temperature. The sensing element is mounted within a sensor body, and it takes time to heat the body. This gives a low pass filter effect on the measured temperature [29, 30]. However, this is not a problem for the measurements of Paper 2 and Paper 4 since they are stationary.

Pressure

The pressure sensors are either the 4260-series or the 4295-series from Kistler, except p_{LFE3} which is measured internally by the LFE3 mass flow sensor system. The pressure sensors for the compressor inlet pressure measurement, $p_{01,1}$, $p_{01,2}$ and $p_{01,3}$ in Figure 2.5, are placed on a straight pipe, following an air filter to reduce flow disturbances. Four pressure taps are connected together, and the sensors $p_{01,1}$ and $p_{01,2}$ are connected to the four taps, while $p_{01,3}$ uses a single pressure tap. The positioning of the pressure taps for p_{02}, p_{03} and p_{04} are restricted due to the packaging, but placed at the most straight sections of the respective pipes. The exhaust side pressure sensors, p_{03} and p_{04}, are mounted on pipes approximately 0.50 m in length, due to restricted temperature limits of the sensors.

The total pressure is calculated from each pressure measurement using the

measured mass flow, measured temperature and the pipe area using the equation

$$p_0 = p + {}^1\!/_2 \rho v^2 = p + \frac{\dot{m}^2}{2A^2\rho}$$

where p_0 is the total pressure, p is the measured static pressure, v is the flow velocity, ρ is gas density, $\dot{m}$ is measured mass flow and A is the cross sectional area at the measurement location. The difference between p_0 and p is the dynamic pressure, describing the increase in pressure that the gas experiences when it is brought to stand still.

All pressure sensors are measured at engine off conditions, both before and after each measurement sequence, to indicate any sensor drift during the measurements. A reference sensor is also used to calibrate the pressure sensors for the measurements. Using long connection pipes between the measurement location and the sensor can cause a low pass filtering effect [30]. This is not a problem here, since the measurements are stationary.

Mass flow

Three different mass flows are measured. $\dot{m}_1$ in Figure 2.5 is measured using the LFE3 system. The LFE3 sensor system is purpose built for automotive research by the Technical University of Denmark (DTU), and uses the differential pressure principle. The differential pressure is measured over a laminar flow element, that gives the volumetric flow. T_{LFE3} and p_{LFE3} are then used to calculated the density, and the mass flow is determined according to

$$\dot{m}_1 = \dot{V} \cdot \rho_{\mathrm{LFE3}} \tag{2.13}$$

where $\dot{V}$ is the volumetric flow and ρ_{LFE3} is the density at the measurement location. The LFE3 differential pressure sensor is a 164PC0137 from Micro Switch Honeywell. The second mass flow sensor, $\dot{m}_2$, is a production sensor, based on the hot-wire principle, and produces a digital signal. An extra differential pressure sensor, is mounted in parallel with the LFE3 differential pressure, for diagnosis purposes. An extra mass flow, $\dot{m}_3$ is calculated also for extra differential pressure sensor, using T_{LFE3} and p_{LFE3} to calculate the air density. The extra differential pressure sensor is a Kistler 4264AB03-sensor.

Both mass flow measurement locations are located on straight pipe sections following air filters, to straighten the air flow.

Turbo speed

The turbo speed N_{tc} of Figure 2.5 is measured using an ACAM PicoTurn BM-V6 system. The BM-V6 system is capable of both analog and digital output signal, where the latter is used to reduce noise sensitivity. The speed sensor position is adjusted using the built in sensor positioning functions of the BM-V6, to ensure the quality of the turbo speed measurement.

3

Compressor modeling

This chapter gives a summary of some of the research that is relevant for automotive compressor modeling, and related to the work in this thesis. A description of the operation and modeling of turbomachinery in general is found in the literature [1, 7, 21]. The chapter begins with a discussion of model based control and mean value engine modeling, while the rest of the chapter is devoted to compressor modeling. The compressor modeling presentation is divided into three parts: modeling of nominal operation, choke or a restriction like operation, and surge, see Figure 3.1 for a sketch of the different regions.

3.1 Model based control and mean value engine modeling

The use of mathematical models in an automotive control system is gaining increased interest from the industry. This increased interest comes from the complex engine concepts used, where additional actuators and degrees of freedom are added to the systems. Model based control is proposed as a way of handling the increased complexity. The models are used for a number of things. Simulation environments can be constructed around the models to aid for example in controller design, in concept evaluations, or in the parametrization process of other controller structures [8, 31, 32]. Observers can be built around the models to estimate non measured states of the system [13]. A direct use of an inverse model can be made, to handle a nonlinearity of a system [33, 34]. The model based control approach have been studied for different automotive control applications, for example in [14, 35, 36, 37].

Mean Value Engine Modeling [38, 39, 40, 41, 42] (MVEM) is a modeling framework used in the automotive society. Here it is used for the full engine simulations in Paper 1, Paper 3 and Paper 4. MVEM usually means that the

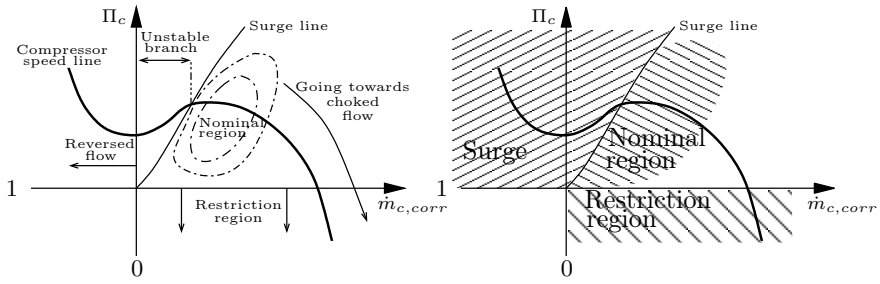

Figure 3.1: Schematic picture of the different compressor operating regions discussed in the text. The nominal region can be approximated with the efficiency contours shown. A decrease in mass flow to the left of the surge line puts the compressor in surge. The compressor is a restriction for $\Pi_c < 1$.

model is based on average values of the engine cycle, i.e. in-cylinder processes such as valve opening and closing are averaged out. This simplification means that vehicle test cycles, consisting of many minutes of driving, can be simulated on a normal PC, with short calculation times.

3.2 Different model families

Modeling of nominal compressor operation is divided into three subsections, depending on the model structure.

3.2.1 3D and 1D models

Gas motion can be modeled in 3D, e.g. solving the Navier-Stokes equations of gas motion numerically. Such modeling needs accurate geometric information of the system, see e.g. the complex impeller geometries of Figure 3.2 and Figure 3.3. The boundary conditions of the model are further important, i.e. how the gas enters and leaves the modeled component. Due to the complexity and the computational effort, these models are most often only used to model components of the engine [43, 44, 45]. The solutions obtained, give valuable information of for example the gas motion, that can be used also for less complex model families. Also the reverse is true [46]; good models from less complex model structures can be used on a component level for a 3D simulation.

Another level of detail that is frequently used, is the 1D model family. They model the gas flow along pipes and account for properties in this dimension. 1D models of compressors are however rarely found. The computational cost is reduced, compared to 3D models, and large parts of an engine system can be simulated with reasonably short simulation times.

3.2.2 Physical 0D compressor models

For the physical compressor model, an ideal compression process is frequently assumed, and different losses are then described and subtracted from the ideal

Figure 3.2: Picture of the low pressure stage impeller (left) and high pressure stage impeller (right) used for the measurements presented in Paper 2 and Paper 4. Both impellers rotate clockwise.

component performance. This model structure often makes use of the velocity triangles, exemplified for the impeller entry in Figure 3.3.

This section follows a gas element through the compressor, and describes important losses along the way, that are compiled to the model. The air flow into the compressor is assumed to have no circumferential velocity, i.e. no pre-whirl, and the diffuser section is assumed to be vane-less. An automotive compressor is normally vane-less and without intentional pre-whirl, due to the fact that a vaned diffuser normally has a narrower flow range, and a pre-whirl system is avoided due to additional cost and packaging constraints.

The first losses occur since the gas has to comply with the vane geometry at the impeller inlet. These losses are referred to as incidence losses [47], and are due to that the inducer relative velocity vector W does not agree with the vector parallel to the vane surface, V, see Figure 3.3. The impeller vane angle varies with the radius of the impeller, since the outer points on the impeller have higher relative velocities [48]. Studying Figure 3.3, the incidence losses are minimized if $I = 0$, however [47] states that the actual velocity vectors are not given simply by the geometries of the compressor, due to inertial effects of the gas.

The fluid friction losses due to the gas viscosity and motion through the compressor are modeled e.g. in [22, 35, 49], where slip is used to model the gas flow through the impeller. Slip describes how well the gas is guided by the impeller vanes, and is discussed and modeled in [7, 21, 50]. Generally, the less guidance the gas attracts from the vanes the more slip. The more guidance, the more friction.

Due to the potentially large pressure gradient through the compressor, flow can recirculate unintentionally. These flow recirculation losses occur due to the clearance between the impeller, rotating at high velocity, and the compressor housing. Flow recirculates both from the pressure side of the impeller vanes to the suction side, and along the compressor housing, from after the impeller,

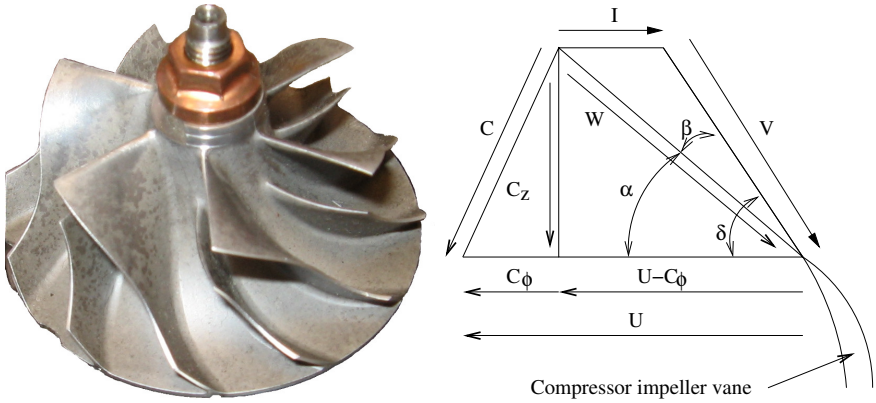

Figure 3.3: Picture of the impeller used for the measurements presented in Paper 1 and the inducer velocity triangle. The Z-axis goes through the turbo shaft, W is the relative flow vector between the gas velocity vector C and the vane velocity vector U. The incidence loss in the inducer is connected to the velocity I. δ denotes the vane angle.

to the impeller entry. Models of these losses are presented e.g in [47, 51]. The air that recirculates to the impeller entry, is already heated by the compression process. In [52] it is stated, that the temperature of the recirculated air increases with increased compressor pressure ratio, and that the amount of recirculated air is a function of pressure ratio and not turbo speed. In [45], this recirculation is said to occur, where the local gas pressure is high and velocity is low. Experimental data of recirculation is also presented in the literature, see e.g [28]. The radial temperature profile at the impeller entry, discussed in [52], is experimentally shown in [28].

For compressors with vaned diffusers, an incidence loss can be associated with the air leaving the impeller, and entering the diffuser passages. These losses are however not simply given by the geometries of the impeller and diffuser vanes, but also of the flow physics inside the impeller [48]. Experimental investigations of the gas motion in the diffuser is found e.g in [53]. The main cause of the diffusion process losses, are in [7] said to be separation of boundary layers and fluid friction.

Losses in the volute [1], and losses due to disc friction [54] and choking [46] can also be modeled. The losses associated with the volute are more pronounced for a vaned diffuser, and are modeled in [47]. In [51] it is noted that the relative magnitude of the clearance, backflow and volute losses decreases with increasing mass flow, since the losses associated with incidence and friction increase more.

3.2.3 Curve fitting 0D based models

The curve fitting based approach is another subset of the 0D model family, and recognizes that all performance variables are conveniently given by the speed lines and the efficiency contours of the map. The modeling effort is then to fit different curves to the map, or to a transformed map.

Semi-physical modeling usually transforms the compressor map variables into the dimensionless head parameter Ψ and the dimensionless mass flow coefficient Φ. A connection between Ψ and Φ is then parametrized and used as a model [39, 55, 56].

Curve fitting directly to the map variables is another way to produce a model. The modeling effort is then to create functions describing the speed lines and iso-contours of efficiency of the map. A summary of curve fitting models for automotive control applications is presented in [57], and both speed line shapes [58] and efficiency contours [13, 59, 60] are modeled.

Both the models of Paper 1 and Paper 3 use a parametrized ellipse to represent the speed lines of the map, and are therefore of the curve fitting family. Curve fitting is also used to represent the efficiency contours of the map in both papers.

3.3 Choke flow and restriction modeling

The previous section described nominal compressor operation and these section presents research relevant for modeling choked flow, and when the compressor only restricts the air, i.e. compressor operation with a pressure ratio lower than unity.

If the inlet section of the compressor chokes, the choking is independent of compressor speed. This since the flow is choked, before it reaches the impeller blades. A varying choke mass flow with shaft speed, can be expected if choking conditions are established further into the compressor. This since the density of the gas arriving at the choking section, can be increased through an increase in compressor speed. In [49] the choke mass flow, assuming that choking occurs in the impeller, is described as an increasing function in shaft speed. A model that extrapolates compressor performance maps to smaller pressure ratios, including choking effects, is described in [46]. For pressure ratios lower than unity the compressor is assumed to work as an restriction for the flow, and the behavior of the compressor is compared to a nozzle discharge characteristic in [61], where further a constant efficiency of 20 % is assumed in this operating region.

Paper 3 uses a choke mass flow model that is affine in corrected shaft speed. This is physically motivated by that a compressor impeller that stands still has a non-zero choke flow, and an increase in choke flow can be expected for increases in corrected shaft speed, up to the point where the compressor inlet chokes. The speed line model of Paper 1 focuses on a the nominal compressor map, but the speed lines are extended to also cover pressure ratios less than unity. Constant compressor efficiency is assumed in this region in both Paper 1 and Paper 3.

3.4 Surge and zero mass flow modeling

The last region of the compressor map is the one left of the surge line in Figure 3.1. When the compressor operating point moves beyond this line, surge will occur since the compressor is unable to maintain flow. When the flow breaks down completely, the highly pressurized air travels upstream, reversing the mass

flow. This reversed flow reduces the pressure ratio, until the compressor is able to maintain positive mass flow. The pressure ratio then increases again and, if no other changes are applied to the system, the compressor enters a new surge cycle. Surge in automotive applications can be encountered for example during a gear change in an acceleration phase. When the accelerator pedal is released, a sharp reduction in throttle mass flow results. Due to the inertia of the turbo, the compressor wheel does not slow down fast, and the compressor continues to build pressure.

To model surge many authors follow the Moore-Greitzer approach [62]. An extra state is introduced in the model to handle changes in mass flow through the compressor, where, due to the gas inertia, the compressor mass flow deviates from stationary performance curves for a transient [63].

Surge can be established from low to high turbo speeds [64]. The frequency of the surge phenomenon is mainly given by the system properties, where the downstream volume is most important. Most of the time in a surge cycle, is spent in either emptying or filling the downstream volume [27, 58, 62], and measurements of a clear connection between increased surge frequency and decreased downstream volume is presented in [63]. The filling period of the cycle is longer than the emptying, due to the flow through the throttle downstream of the compressor [62]. The surge frequency also depends on the compressor characteristic, and compressor speed will therefore also affect the surge frequency [27, 62].

The surge phenomenon has a hysteresis effect, where the breakdown of the flow does not follow the same path in the compressor map as the build up of flow [28, 62]. Mass flow measurements of surge presented in [28], show that the flow reversal is conducted at nearly constant pressure, followed by an increasing mass flow at lower pressure, and finally a rapidly increasing mass flow to a steady flow compressor speed line.

The unstable branch of a compressor speed line is modeled using a third order polynomial in [52], and is said to influence the modeled surge cycles to a small degree, since the time spent there is small [64]. Compressor pressure ratio at zero mass flow has been modeled in different versions in [52, 63, 65, 66]. The negative flow branch of an extended compressor map, is modeled using a parabola with good accuracy in [64], and as a second order polynomial in [52]. Further, [52] assumes an efficiency for surged mass flow of 20 %, and an isothermal expansion is assumed in [63].

The Moore-Greitzer approach is followed in both Paper 1 and Paper 3, and a third order polynomial in corrected mass flow is used in both papers for the unstable branch. This polynomial is parametrized to give zero derivative for the zero mass flow pressure build up point. The model of Paper 3 then uses a turbine flow characteristic for the negative flow branch, while Paper 3 uses the third order polynomial also for reversed flow. Constant compressor efficiency is assumed for surging mass flows in both papers.

Bibliography

[1] N. Watson and M.S. Janota. *Turbocharging the internal combustion engine.* MacMillan London, 1982.

[2] J.B. Heywood. *Internal Combustion Engine Fundamentals.* McGraw-Hill series in mechanical engineering. McGraw-Hill, 1988.

[3] Richard Stone. *Introduction to Internal Combistion Engines.* MacMillan London, second edition, 1992.

[4] B. Lee, Z Filipi, D. Assanis, and D. Jung. Simulation-based assessment of various dual-stage boosting systems in terms of performance and fuel economy improvements. SAE Technical Paper 2009-01-1471, 2009.

[5] J. Galindo, H. Climent, C. Guardiola, and A. Tiseira. Assessment of a sequantially turbocharged diesel engine on real-life driving cycles. *International Journal of Engine Research*, 49(1/2/3):214 – 234, 2009.

[6] Karl Zinner. *Aufladung von Verbrennungsmotoren. Grundlagen, Berechnungen, Ausführungen.* Springer Verlag, 1985.

[7] S.L. Dixon. *Fluid Mechanics and Thermodynamics of Turbomachinery.* Butterworth-Heinemann, fourth edition, 1998.

[8] Oskar Leufven and Lars Eriksson. Time to surge concept and surge control for acceleration performance. IFAC World Congress, Seoul, Korea, 2008.

[9] O. Leufven and L. Eriksson. Engine test bench turbo mapping. SAE Technical Paper 2010-01-1232, 2010.

[10] O. Leufven and L. Eriksson. Surge and choke capable compressor model. Submitted to IFAC World Congress, Milano, Italy, 2011.

[11] O. Leufven and L. Eriksson. Investigation of compressor correction quantities for automotive applications. *Submitted to International Journal of Engine Research*.

[12] Thierry Lamquin and Kostandin Gjika. Power losses identification on turbocharger hydrodynamic bearing systems: test and prediction. In *GT2009-59599*, Proceedings of ASME Turbo Expo, Orlando Florida, USA, June 2009.

[13] P. Andersson. *Air Charge Estimation in Turbocharged Spark Ignition Engines*. PhD thesis 989, Department of Electrical Engineering, Linköpings Universitet, Linköping, Sweden, 2005.

[14] Marcus Ammann. *Modellbasierte Regelung des Ladedrucks und der Abgasrückführung beim aufgeladenen PKW-Common-Rail-Dieselmotor*. PhD thesis 15166, Eidgenössischen Technischen Hochschule Zürich, 2003.

[15] Michael V. Casey and Thomas M. Fesich. On the effiency if compressors with diabatic flows. In *GT2009-59015*, Proceedings of ASME Turbo Expo, Orlando Florida, USA, June 2009.

[16] Nick Baines, Karl D. Wygant, and Antonis Dris. The analysis of heat transfer in automotive turbochargers. In *GT2009-59353*, Proceedings of ASME Turbo Expo, Orlando Florida, USA, June 2009.

[17] Matthias Mrosek and Rolf Isermann. On the parametrisation of turbocharger power and heat transfer models. In *IFAC Symposium Advances in Automotive Control*, Munich, Germany, 2010.

[18] Colin D. Copeland, Ricardo Martinez-Botas, and Martin Seiler. Unsteady performance of a double entry turbocharger turbine with a comparison to steady flow conditions. In *GT2008-50827*, Proceedings of ASME Turbo Expo, Berlin, Germany, June 2008.

[19] Jan F. Suhrmann, Dieter Peitsch, Marc Gugau, Tom Heuer, and Uwe Tomm. Validation and development of loss models for small size radial turbines. In *GT2010-22666*, Proceedings of ASME Turbo Expo, Glasgow, UK, June 2010.

[20] Edward S. Taylor. *Dimensional analysis for engineers*. Clarendon Press, Oxford, 1974.

[21] R. I. Lewis. *Turbomachinery Performance Analysis*. Arnold, 1996.

[22] F.M White. *Fluid Mechanics*. McGraw-Hill, 2005.

[23] SAE. SAE J1826 – Turbocharger Gas Stand Test Code. SAE standard, 1995.

[24] SAE. SAE J922 – Turbocharger Nomenclature and Terminology. SAE standard, 1995.

[25] ASME. PTC 10-1997, Performance test code on compressors and exhausters. American Society of Mechanical Engineers, New York, 1997.

[26] Kirby S. Chapman and Jacque Shultz. Guidelines for: Testing large-bore engine turbochargers. Technical report, The National Gas Machinery Laboratory, Kansas State University, 245 Levee Drive, 2003.

[27] J. Galindo, J.R. Serrano, C. Guardiola, and C. Cervelló. Surge limit definition in a specific test bench for the characterization of automotive turbochargers. *Experimental Thermal and Fluid Science*, 30(5):449 – 462, 2006.

[28] J. Andersen, F. Lindström, and F. Westin. Surge Definitions for Radial Compressors in Automotive Turbochargers. *SAE International Journal of Engines*, 1(1):218, 2008.

[29] M.H. Westbrook and J.D. Turner. *Automotive sensors*. IOP Publishing, 1994.

[30] Per Erik Lindahl and William Sandqvist. *Mätgivare, mätning av mekaniska storheter och temperatur*. Studentlitteratur, 1996.

[31] Johan Wahlström. *Control of EGR and VGT for Emission Control and Pumping Work Minimization in Diesel Engines*. PhD thesis, Linköpings universitet, 2009.

[32] Andreas Thomasson, Lars Eriksson, Oskar Leufven, and Per Andersson. Wastegate actuator modeling and model-based boost pressure control. IFAC Workshop on Engine and Powertrain Control, Simulation and Modeling, Paris, France, 2009.

[33] I. Criscuolo, O. Leufven, A. Thomasson, and L. Eriksson. Model-based boost pressure control with system voltage disturbance rejection. Submitted to IFAC World Congress, Milano, Italy, 2011.

[34] Andras Thomasson and Lars Eriksson. Model-based throttle control using static compensators and IMC based PID-design. IFAC Workshop on Engine and Powertrain Control, Simulation and Modeling, Paris, France, 2009.

[35] J.T. Gravdahl, F. Willems, B. de Jager, and O. Egeland. Modeling for surge control of centrifugal compressors: comparison with experiment. In *Decision and Control, 2000. Proceedings of the 39th IEEE Conference on*, volume 2, pages 1341 –1346 vol.2, 2000.

[36] M. Ammann, N.P. Fekete, L. Guzzella, and A.H. Glattfelder. Model-based control of the VGT and EGR in a turbocharged common-rail diesel engine: Theory and passenger car implementation. SAE Technical Paper 2003-01-0357, Detroit, USA, March 2003.

[37] Jan-Ola Olsson. Boost limitation in a torque based engine management system. 5th IFAC Symposium on Advances in Automotive Control, 2007.

[38] E. Hendricks. A compact, comprehensive model of a large turbocharged, two-stroke diesel engine. SAE Technical Paper 861190, 1986.

[39] J.-P. Jensen, A.F. Kristensen, S.C. Sorenson, N. Houbak, and E. Hendricks. Mean value modeling of a small turbocharged diesel engine. SAE Technical Paper 910070, Detroit, USA, Februar 1991.

[40] E. Hendricks. Isothermal vs. adiabatic mean value SI engine models. In *3rd IFAC Workshop, Advances in Automotive Control, Preprints, Karlsruhe, Germany*, pages 373–378, March 2001.

[41] Lars Eriksson, Lars Nielsen, Jan Brugård, Johan Bergström, Fredrik Pettersson, and Per Andersson. Modeling of a turbocharged SI engine. *Annual Reviews in Control*, 26(1):129 – 137, 2002.

[42] Lars Eriksson. Mean value models for exhaust system temperatures. *SAE Transactions, Journal of Engines, 2002-01-0374*, 111(3), September 2002.

[43] Donghui Zhang, Jean-Luc Di Liberti, and Michael Cave. Blade thickness effect on impeller slip factor. In *GT2010-22164*, Proceedings of ASME Turbo Expo, Glasgow, UK, June 2010.

[44] Fahua Gu, Abraham Engeda, Mike Cave, and Jean-Luc Di Liberti. A numerical investigation on the volute/diffuser interaction due to the axial distortion at the impeller exit. *Journal of Fluids Engineering*, 123(3):475–483, 2001.

[45] Fredrik Hellström. *Numerical computations of the unsteady flow in turbochargers*. PhD thesis, KTH, Fluid Physics, 2010.

[46] M.V Casey and M Schlegel. Estimation of the performance of turbocharger compressors at extremely low pressure ratios. *Proceedings of the Institution of Mechanical Engineers, Part A: Journal of Power and Energy*, 224(2):218, 2010.

[47] J.T. Gravdahl and O. Egeland. Centrifugal compressor surge and speed control. *Control Systems Technology, IEEE Transactions on*, 7(5):567 –579, sep 1999.

[48] J. Galindo, J.R. Serrano, X. Margot, A. Tiseira, N. Schorn, and H. Kindl. Potential of flow pre-whirl at the compressor inlet of automotive engine turbochargers to enlarge surge margin and overcome packaging limitations. *International Journal of Heat and Fluid Flow*, 28(3):374 – 387, 2007.

[49] J.T. Gravdahl and O. Egeland. Speed and surge control for a low order centrifugal compressor model. In *Control Applications, 1997., Proceedings of the 1997 IEEE International Conference on*, pages 344 –349, 5-7 1997.

[50] Xuwen Qiu, Dave Japikse, Jinhui Zhao, and Mark R. Anderson. Analysis and validation of a unified slip factor model for impellers at design and off-design conditions. In *GT2010-22164*, Proceedings of ASME Turbo Expo, Glasgow, UK, June 2010.

[51] Wei Jiang, Jamil Khan, and Roger A. Dougal. Dynamic centrifugal compressor model for system simulation. *Journal of Power Sources*, 158(2):1333 – 1343, 2006.

[52] Panagiotis Grigoriadis. *Experimental Erfassung und Simulation instantionärer Verdichterphänomene bei Turboladern von Fahrzeugmotoren*. PhD thesis, Technischen Universität Berlin, 2008.

[53] T Sato, J M Oh, and A Engeda. Experimental and numerical investigation of the flow in a vaneless diffuser of a centrifugal compressor stage. part 1: Experimental investigation. *Proc. of the IMechE, Part C: J. of Mech. Eng. Science*, 219(10), September 2005.

[54] M. Yang, X Zheng, Y. Zhang, and Z Li. Improved performance model of turbocharger centrifugal compressor. In *GT2008-50009*, Proceedings of ASME Turbo Expo, Berlin, Germany, June 2008.

[55] Spencer C. Sorenson, Elbert Hendrick, Sigurjon Magnusson, and Allan Bertelsen. Compact and accurate turbocharger modelling for engine control. In *Electronic Engine Controls 2005 (SP-1975)*, number SAE Technical Paper 2005-01-1942, 2005.

[56] Lars Eriksson. Modeling and control of turbocharged SI and DI engines. *Oil & Gas Science and Technology - Rev. IFP*, 62(4):523–538, 2007.

[57] Paul Moraal and Ilya Kolmanovsky. Turbocharger modeling for automotive control applications. SAE Technical Paper 1999-01-0908, March 1999.

[58] J. Bergström and O. Leufven. Surge modeling and control of automotive turbochargers. Master's thesis LiTH-ISY-EX-3999, Department of Electrical Engineering, Linköpings Universitet, Linköping, Sweden, June 2007.

[59] A.A. Sokolov and S.T. Glad. Identifiability of turbocharged IC engine models. SAE Technical Paper 1999-01-0216, March 1999.

[60] Olof Erlandsson. *Thermodynamic Simulation of HCCI Engine Systems*. PhD thesis 989, Department of Heat and Power Engineering, Lund Institute of Technology, 2002.

[61] M. Müller, S. Sumser, P. Fledersbacher, K. Rößler, K. Fieweger, and HJ Bauer. Using the Centrifugal Compressor as a Cold-Air Turbine. In *8th international conference on turbochargers and turbocharging, Imperial College London*, 2005.

[62] E. M. Greitzer. The stability of pumping systems - The 1980 Freeman Scholar Lecture. *ASME Transactions Journal of Fluids Engineering*, 103:193–242, June 1981.

[63] J. Galindo, J.R. Serrano, H. Climent, and A. Tiseira. Experiments and modelling of surge in small centrifugal compressor for automotive engines. *Experimental Thermal and Fluid Science*, 32(3):818 – 826, 2008.

[64] K. E. Hansen, P. Jorgensen, and P. S. Larsen. Experimental and theoretical study of surge in a small centrifugal compressor. *ASME Journal Fluids Engineering*, (103):391–395, 1981.

[65] G. Theotokatos and N.P. Kyrtatos. Diesel engine transient operation with turbocharger compressor surging. 2001.

[66] J.T. Gravdahl, O. Egeland, and S.O. Vatland. Active surge control of centrifugal compressors using drive torque. In *Decision and Control, 2001. Proceedings of the 40th IEEE Conference on*, volume 2, 2001.

Papers

Paper 1

1

Time to surge concept and surge control for acceleration performance[†]

Oskar Leufven and Lars Eriksson

Vehicular Systems, Department of Electrical Engineering,
Linköping University, S-581 83 Linköping,
Sweden.

Abstract

Surge is a dangerous instability that can occur in compressors. It is avoided using a valve that reduces the compressor pressure. The control of this valve is important for the compressor safety but it also has a direct influence on the acceleration performance.

Compressor surge control is investigated by first studying the surge phenomenon in detail. Experimental data from a dynamic compressor flow test bench and surge cycles measured on an engine is used to tune and validate a model capable of describing surge. A concept named *time to surge* is introduced and a sensitivity analysis is performed to isolate the important characteristics that influence surge transients in an engine. It is pointed out that the controller clearly benefits from a feed-forward term due to the small time frames associated with the transition to surge. In the next step this knowledge is used in the design of a novel surge controller. This surge controller is then compared to two other controllers and it is shown that it avoids surge and improves the acceleration performance by delivering both higher engine torque and turbo shaft speed after a gear change.

[†]This is a formatted version of "Time to surge concept and surge control for acceleration performance" by Oskar Leufven and Lars Eriksson, IFAC World Congress 2008, Seoul, Korea.

1 Introduction

From being used exclusively in sports and performance cars, turbochargers are now common even in ordinary family cars. Ever increasing fuel prices and focus on the environment have moved the automotive industry from using large bigbore engines to using the advantages of downsized and turbocharged engines instead [1].

An important component in the turbocharger is the compressor as it influences the engine power and thus acceleration performance. In the compressor a dangerous instability phenomenon called surge can occur. It is a small time frame phenomenon caused by the relatively slow dynamics of the turbo shaft. If an automotive turbocharger is driven in deep surge cycles for too long the turbo charger will break down. An effective fail safe method for avoiding surge using a surge valve is implemented in today's production cars. However, in order to ensure safety in all cases, this method wastes much of the valuable pressurized air and turbo shaft speed. Surge control is most important during a gear change since the compressor pressure directly influences the torque available when the new gear is engaged.

The approach is to use experimental surge data from both a compressor surge test stand and an engine test bench to build and validate a compressor and engine model that can describe surge. Then a sensitivity analysis is performed to investigate what properties are most important when considering the time to reach surge and then it is studied what can be done to increase the engine acceleration performance through surge valve control. Based on the knowledge gained from the surge investigation a novel control structure for surge control is developed. One important part is the feedforward term, motivated by the short time frames associated with surge control. The developed controller is then compared to two other controllers.

2 Modeling

To investigate surge and different control strategies a surge capable compressor model has been developed. It is implemented as part of a Mean Value Engine Model (MVEM) [2] of a turbocharged Spark Ignited (SI) engine in Simulink. The model structure is component based using restrictions (air filter, compressor, intercooler, throttle, engine, turbine, exhaust system) interconnected with control volumes, and further extended with surge and wastegate valves. Component based MVEM of turbocharged engines is outlined in [3] and [4] while the implemented model is developed and validated in [5]. The generel structure of the model is shown in figure 1 and the states and notation used is given in the appendix. There are in all 14 states; six pairs of control volume pressures and temperatures, shaft speed and, for the surge capability, compressor mass flow.

2.1 Surge region modeling

The original MVEM has been extended to handle surge [6, 7]. The extension utilizes the model by Moore-Greitzer [4, 8] and introduces a compressor mass

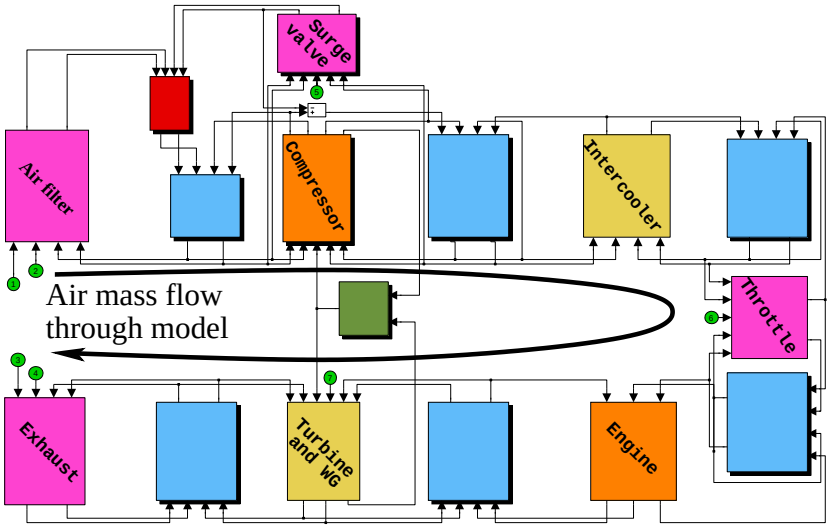

Figure 1: Engine model with a surge capable compressor model. The mass flow path starts in the air filter (upper left corner) and continues through the compressor, intercooler, throttle, intake manifold, cylinder(s), exhaust manifold, turbine to the exhaust system (lower left corner). These different components are interconnected with control volumes. The turbocharger shaft is seen between the compressor and the turbine. The model also contains a wastegate and a surge valve.

flow state, given by

$$\frac{dW_c}{dt} = \frac{\pi D_c^2}{4L_c} \cdot (\hat{p}_c - p_c) \tag{1}$$

Here $\hat{p}_c = \hat{p}_c(T_{af}, p_{af}, p_c, \omega_{tc}, W_c)$ describes the compressor pressure build up using the parameterized Ellipse model developed in [6] which handles both forward as well as backward (surging) compressor mass flows. Methods for determining and tuning the parameters of the surge capable compressor model are also described in [6].

2.2 Surge region validation

To ensure that the model captures real surge phenomena the implemented compressor model is validated against measured data. Validation data from both a separate compressor surge test stand and surge measurements on a real engine are used. The surge test stand validation is shown in figure 2. It is shown that the surge cycle time and compressor pressure ratio behavior during surge is well described by the model. The full MVEM is validated in figure 3 with respect to compressor pressure ratio and turbo shaft speed variations for a rapid throttle closing transient. The validations show that the model gives good description of surge properties, which will be important for the control development, in particular: where surge starts, cycle times, pressure fluctuations and also turbo shaft speed changes.

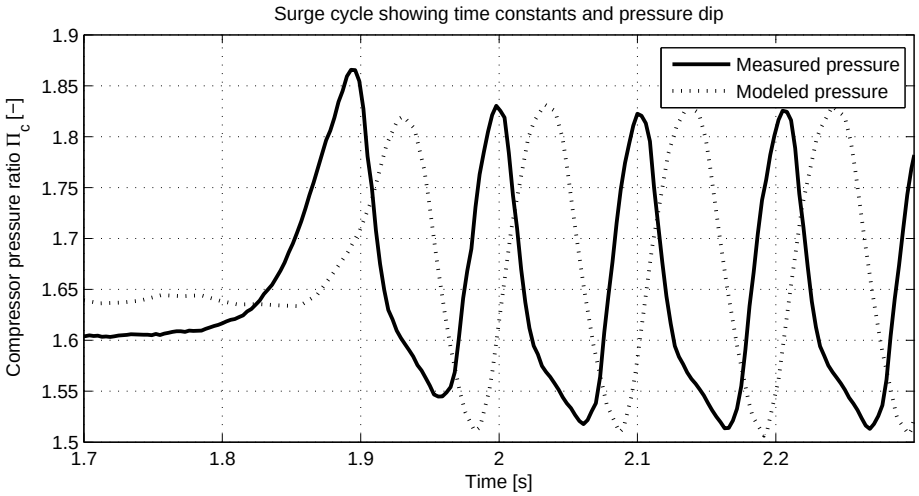

Figure 2: Measured (solid) and modeled (dashed) surge cycle pressures. The figure shows that the compressor model captures both the surge cycle time as well as pressure dynamics during surge as the measurements.

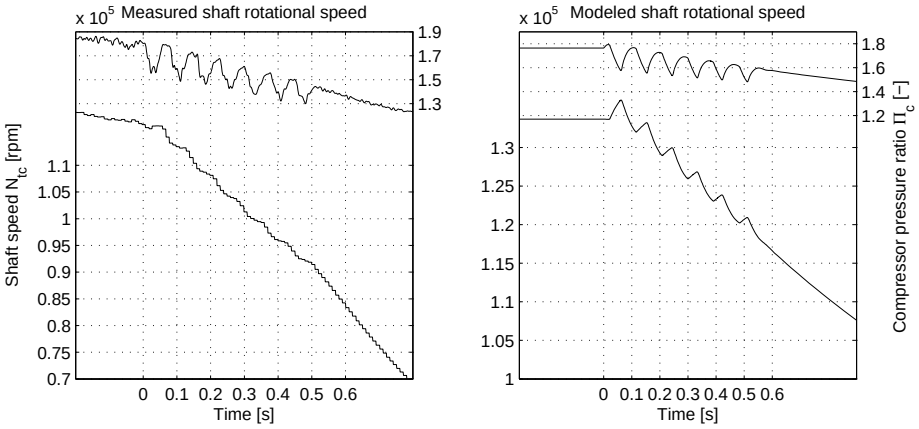

Figure 3: Turbo shaft speed and pressure variations for a rapid throttle closing transient. Left–measured, right–modeled for an operating point close to measured data. It is seen that the turbo shaft speed does not change much from the surge initiation until the compressor has entered the first surge cycle, which motivates the assumption that the shaft dynamics can be neglected when TTS is investigated.

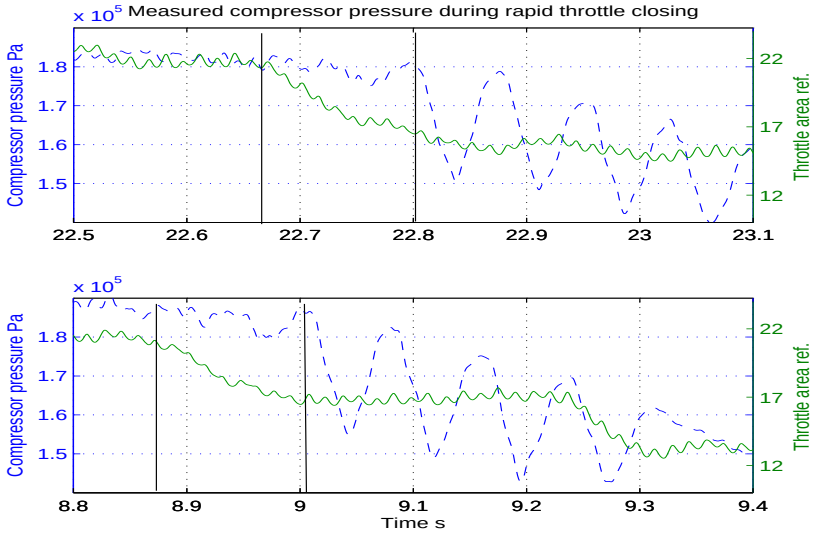

Figure 4: Pressure measured after the compressor (dashed) from two fast throttle closings are plotted together with the throttle area reference signal (solid). Lines are also shown to emphasize where the step is applied and where the compressor starts surging. For both these finite closing speed transients TTS is about 0.1s. The measured signals are filtered offline using a low pass filter with zero phase shift.

3 Time to surge – TTS

As a first step in the controller design the requirements are investigated. The surge phenomenon is very fast and thus puts stringent requirements on the necessary controller reaction time. To facilitate an analysis of this requirement a concept called *Time To Surge* (TTS) is introduced. TTS describes how long time it takes for the compressor to enter surge for every operating point in the compressor map, thus showing the needed response time of the control system. Measured compressor pressure from two fast throttle closings are plotted together with the throttle area reference signal in figure 4. It is seen that the throttle closing is not instantaneous and that the TTS is slightly larger than 0.1s.

The most common cause for surge in an automotive turbocharged engine is a fast throttle closing, e.g. associated with a gear change. Therefore the calculation of TTS is based on the following scenario: the compressor starts in an initial operating point, then there is a sudden drop in throttle mass flow which will lead the compressor into surge. The compressor is said to enter surge when the compressor mass flow equals the surge mass flow for the current shaft speed. The surge mass flow is given by the compressor map and the line formed by the surge mass flows for all shaft speeds is called the surge line, SL.

TTS depends on many system properties and to study what is most important a sequence of increasingly complex systems are studied in the following sections.

3.1 System 1: Instantaneously zero throttle mass flow

In the first system both the intercooler restriction and temperature differences/dynamics are neglected. Furthermore the turbo shaft speed is assumed constant, due to the small time frames of the surge phenomenon compared to the turbo shaft dynamics (see figure 3). The conditions in the air filter control volume (p_{af}, T_{af}) are also kept constant. Finally it is assumed that the throttle mass flow immediately goes to zero in the transient. The differential equations for this simple system now become

$$\frac{dp}{dt} = \frac{RT}{V}(W_c - W_{th}) \tag{2a}$$

$$\frac{dW_c}{dt} = \frac{\pi D_c^2}{4L_c}(\hat{p}_c - p_c) \tag{2b}$$

$$W_{th} = 0 \qquad \text{for } t > t_{init} \tag{2c}$$

where the assumption of an isothermal model, [9], for the lumped control volume is used. A normal temperature increase of 80K over the compressor is assumed as well as a constant control volume temperature before the compressor of 290K. The resulting TTS from this approach is shown in figure 5. The figure shows a worst case, smallest time, originating from a throttle mass flow instantaneously going from $W_{c,init}$ to 0. Even for large mass flows far away from the SL, the time is rather small and a feedback control system thus has to be fast and combined with fast actuators to be able to avoid surge.

3.2 System 2: Dynamic throttle behavior

In the next step the instantaneous stop in throttle mass flow is extended with a first order system for the throttle mass flow. This models the finite response time of a throttle system. The system is now described by (2) but where equation (2c) is exchanged for

$$\begin{aligned} \tfrac{dW_{th}}{dt} &= -\tau_{th} W_{th} + u_{th} \\ u_{th} &= \begin{cases} W_{th,init} & t < t_{init} \\ 0 & t \geq t_{init} \end{cases} \end{aligned} \tag{3}$$

Since the throttle dynamics is not known exactly, two different first order system time constants, τ_{th}, are used. The results from the calculations for $\tau_{th} = 0.025$s are shown in figure 6. Compared to system 1, figure 5, the TTS is larger for every operating point, which is expected. The differences between the two time constants, τ_{th}, are obvious. The behavior is similar but the slowly closing throttle has a much larger TTS. This shows that the throttle closing time constant has a significant impact on TTS.

3.3 System 3: Temperature dynamics in intermediate control volumes

The next extension is to add the temperature dynamics, i.e. using the adiabatic model [9], of the lumped control volume. Compressor upstream conditions are

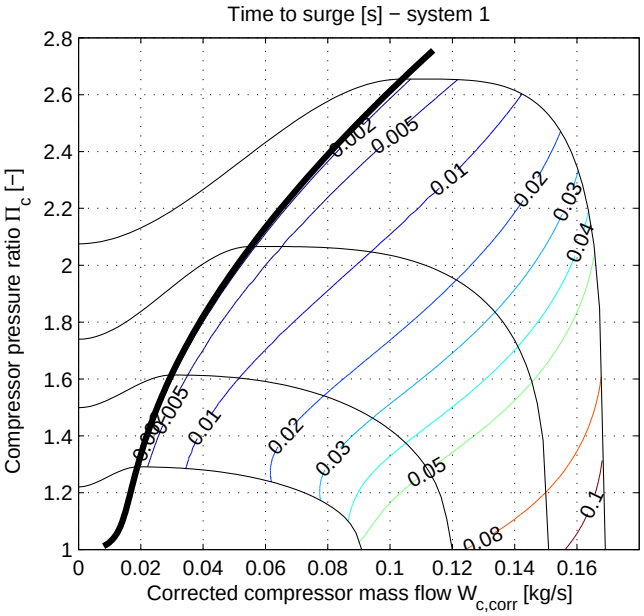

Figure 5: TTS for system 1. The approach assumes an instantaneous stop in throttle mass flow and underestimates the TTS, showing a worst case scenario.

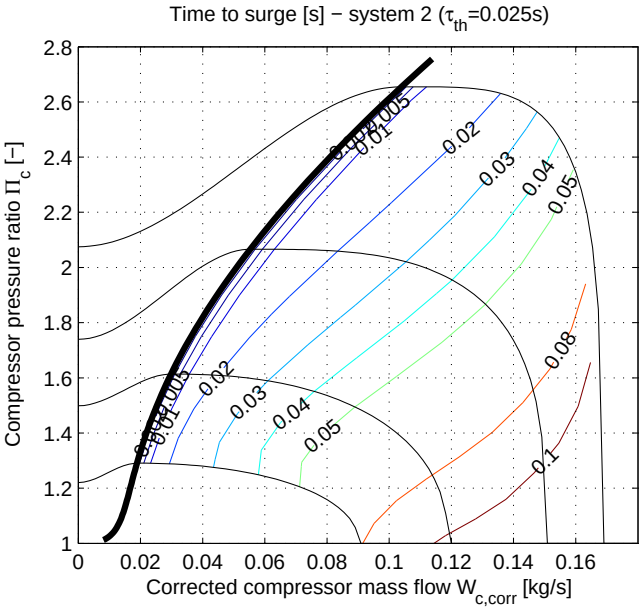

Figure 6: TTS for system 2. Shown is the TTS map for a throttle time constant of $\tau_{th} = 0.025$s. Larger constants have the same qualitative behavior but differs in the numerical values.

still kept constant for this system, as is the turbo shaft speed. The states for this system are $W_c, p_{cv}, T_{cv}, W_{th}$.

If TTS for this system, shown in figure 3.4, is compared to figure 6 it is easy to see that the extra temperature dynamics introduced has only minor effect. Also the qualitative behavior of the TTS is preserved. The temperature dynamics can thus be neglected.

3.4 System 4: Complete 14 states MVEM

As a final investigation the full 14 states MVEM is used to see if there are other effects that have a major impact on TTS. In the previously investigated systems three simplifying assumptions have been made; constant inlet conditions, lumped control volume and constant shaft speed. These will be addressed here. The first by adding an air filter restriction and control volume, which allows the compressor inlet conditions to vary. In particular the inlet pressure will be slightly lowered and mass flow dependent. The second by introducing the intercooler restriction and an extra control volume between compressor and throttle. The third by the introduction of turbo shaft dynamics, allowing the compressor speed to vary (see figure 3).

For the complete model with $\tau_{th} = 0.025$s the TTS-map is shown in figure 8. TTS for $\tau_{th} = 0.1$s is as expected larger. Even for this multi state system it is obvious that the throttle closing speed, essentially τ_{th}, has a major effect on the time it takes before the compressor enters surge.

The differences between the complete MVEM model and the three simple approaches presented earlier are small. TTS is around $10-15\%$ larger throughout the compressor map compared to system 2 and 3. Using any of the simpler approaches to calculate TTS would thus give a control system some margin.

3.5 Conclusions of the TTS-investigation

Throughout the investigation a clear trend in parameter sensitivity can be seen. The single most important factor is how fast the throttle closes, due to the close connection between effective throttle area and throttle mass flow. In summary, these are the main results from the investigation

- The most important parameter is the throttle time constant τ_{th}.
- Shaft speed variations can be neglected with a good result because of the relatively slow dynamics.
- Temperature dynamics can be neglected unless very small control volumes are being used.

As can be seen in the small differences between the full MVEM model and the three simpler approaches, even a less complex method for determining TTS gives satisfactory performance.

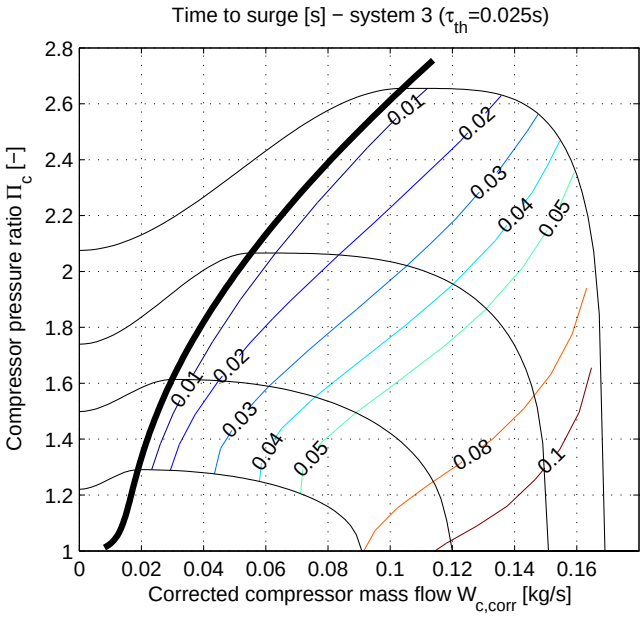

Figure 7: TTS for Approach 3 for the throttle time constant $\tau_{th} = \frac{1}{40} = 0.025$s. A comparison with figure 6 shows that the introduction of control volume temperature dynamics as a state has only very minor effect.

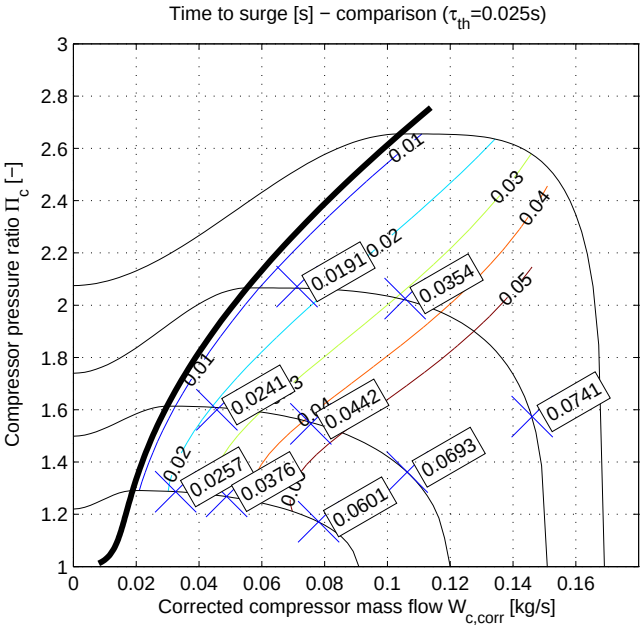

Figure 8: TTS using the full 14 states model, $\tau_{th} = 0.025$s. Isolines in the background are from system 3 with the same τ_{th}.

4 Construction of a surge control system

There are two actuators available for surge control, wastegate and surge valve. The wastegate valve effects the driving torque from the turbine and the surge valve releases pressurized air after to before the compressor. The wastegate has almost no effect due to the slow dynamics of the turbine shaft. The main actuator is therefore the surge valve.

4.1 Feedforward or feedback control

The discussion so far supports the claim that a feedforward control system is needed. The largest TTS for the throttle closings studied are all less than around 0.2s. If only real operating points are considered this maximum time is reduced even further and for normal operating points it is closer to 0.05s. The necessary reaction times of a control system are thus even faster. If feedback control is to be used, the reaction time of the control system can be divided into three parts: control system sample time, feedback sensor response time and actuator response time. Reducing any of these parts almost always implies a large increase in production costs.

One way to enhance the possibilities to avoid surge is to add a surge valve controlled not only by the Electronic Control Unit (ECU) but also controlled by a pressure difference. To add even more safety to the system the control system could be constructed to close the surge valve and leave the opening to a pressure difference system, see [6].

4.2 Surge valve characteristic

The surge valve of the MVEM is implemented as

$$\begin{aligned} T &= T_c \\ W_{sv} &= A_{sv} \frac{p_c}{\sqrt{T_c R}} \sqrt{\frac{2\gamma}{\gamma-1}\left(p_r^{\frac{2}{\gamma}} - p_r^{\frac{\gamma+1}{\gamma}}\right)} \end{aligned} \tag{4}$$

with $p_r = \max\left(\frac{p_{af}}{p_c}, \left(\frac{2}{\gamma+1}\right)^{\frac{\gamma}{\gamma-1}}\right)$. A surge valve has a maximum effective opening area and the surge valve maximum mass flow is shown in figure 9 for two different effective areas. Only surge control for cases where the surge valve can recycle the compressor surge mass flow are considered, thus meaning shaft speeds where

$$W_{sv,max} > W_{c,surge,noncorr} \tag{5}$$

effectively giving an upper limit for the shaft speeds to be considered. The flow $W_{c,surge,noncorr}$ is the real mass flow, i.e. not corrected, at the surge line for the given shaft speed. Due to the fact that the maximum mass flow through the surge valve is also inversely proportional to the square root of the compressor control volume temperature, the possible control region is further reduced. The air filter control volume temperature is also assumed to vary little from the ambient temperature due to the heated recycled air, effectively meaning that the recycled air mass is considered small compared to the control volume mass.

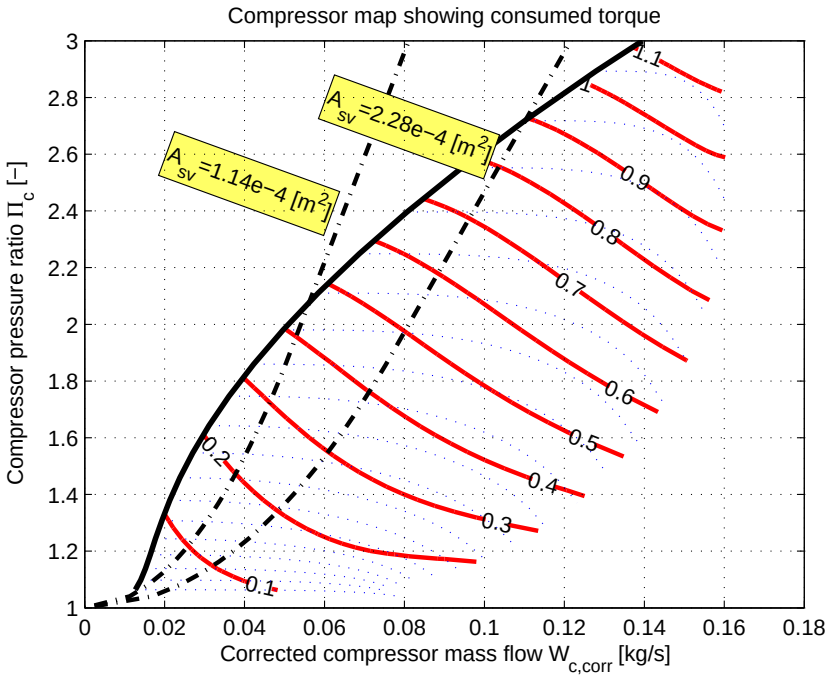

Figure 9: Consumed compressor torque shown with solid line. Dashed line shows compressor speed line. Seen is that for every speed line the minimum consumed torque is to be found at the surge line (or left of this). Surge valve characteristics are also shown for two different effective areas, $1.14 \cdot 10^{-4}\mathrm{m}^2$ and $2.28 \cdot 10^{-4}\mathrm{m}^2$, from [7].

4.3 Formulation of control goal

To retain high turbo shaft speeds, during e.g. gear changes, the goal for the control system is to keep the operating point on the highest possible shaft speed. The spool up time for the turbo is then reduced when the new gear is engaged and the demand for engine torque rises again. Retaining turbo shaft speed means keeping the driving torque from the turbine high and keeping the torque consumed by the compressor low. This can be seen in the turbo shaft dynamics

$$\begin{aligned} \frac{d(N_{tc}\frac{\pi}{30})}{dt} &= \frac{d\omega_{tc}}{dt} = \frac{1}{J_{tc}}(Tq_t - Tq_c - Tq_{tc,f}) \\ Tq_c &= \frac{30}{\pi}\frac{(T_c - T_{af})\cdot c_p \cdot W_c}{N_{tc}} \end{aligned} \tag{6}$$

The consumed torque is proportional to both the temperature difference over the compressor as well as the compressor mass flow. Further it is inversely proportional to the shaft speed. To be able to find the most interesting compressor operating point consumed compressor torque isolines are shown in figure 9. It can be seen that for every shaft speed the least amount of torque is consumed for operating points at the surge line.

4.4 Control algorithm

The control algorithm for the feedforward controller is as follows: when the throttle closing is commanded, calculate the time it takes for the operating point to reach the surge line, TTS. When the surge line (SL) is reached open the surge valve directly to a mass flow according to the following

$$\begin{array}{ll} W_{sv} & = 0 \qquad\qquad\qquad\quad t_{init} < t < t_{init} + t_{TTS} \\ W_{sv} & = W_{th} - W_{c,surge} \quad t = t_{init} + t_{TTS} \end{array} \tag{7}$$

meaning that the surge valve is closed for the first TTS seconds and thereafter opened to stabilize W_c at the SL. When this is done, engage a PI(D)-controller that follows the SL.

5 Controller evaluation

A test scenario is used for evaluation. It consists of a one second long gear change where the throttle area is dropped to a minimum. The time constant used for the throttle is $\tau_{th} = 0.025$s giving a fast system to control. The controller described in the previous section is compared to two other controllers, one using a simple blow-off-technique that keeps the surge and waste gate valve fully open and one using feedback from mass flows and utilizing a PI-controller. A first order system surge valve, having a time constant of $\tau_{sv} = 0.02$s was used for all three controllers as well as a maximum effective surge valve area of $1.14 \cdot 10^{-4}\text{m}^2$, see [7]. The effect from more realistic cases having pulse width modulated control signals and time delays in the system are studied in [6].

The results from the gear change test case is shown in figure 10. It is seen that the feedforward controller has a up to 8% higher engine output torque and up to 20% higher turbo shaft speed. The difference is, as expected, decreasing slowly after the gear change and in the long run the operating points of all three systems will converge.

6 Conclusions

A measurement, called Time To Surge (TTS), of how long time it takes for a compressor to enter surge after a fast throttle closing is proposed. Different methods, of increasing complexity, for determining TTS are compared through the usage of a validated surge capable mean value engine model, having 14 states. The MVEM model is parameterized and validated using experimental data. The TTS parameter sensitivity is studied and TTS is found to depend mainly on throttle closing speed. There are no significant changes when taking the temperature or turbo shaft dynamics into account. A system that uses only three states (p_c, W_c, W_{th}) and an isothermal assumption gives a good description and has only a maximum deviation of 10% compared to the complete MVEM model. The largest TTS for normal compressor operating points is found to be around 0.1s which gives a strong motive for a feedforward loop in the control system.

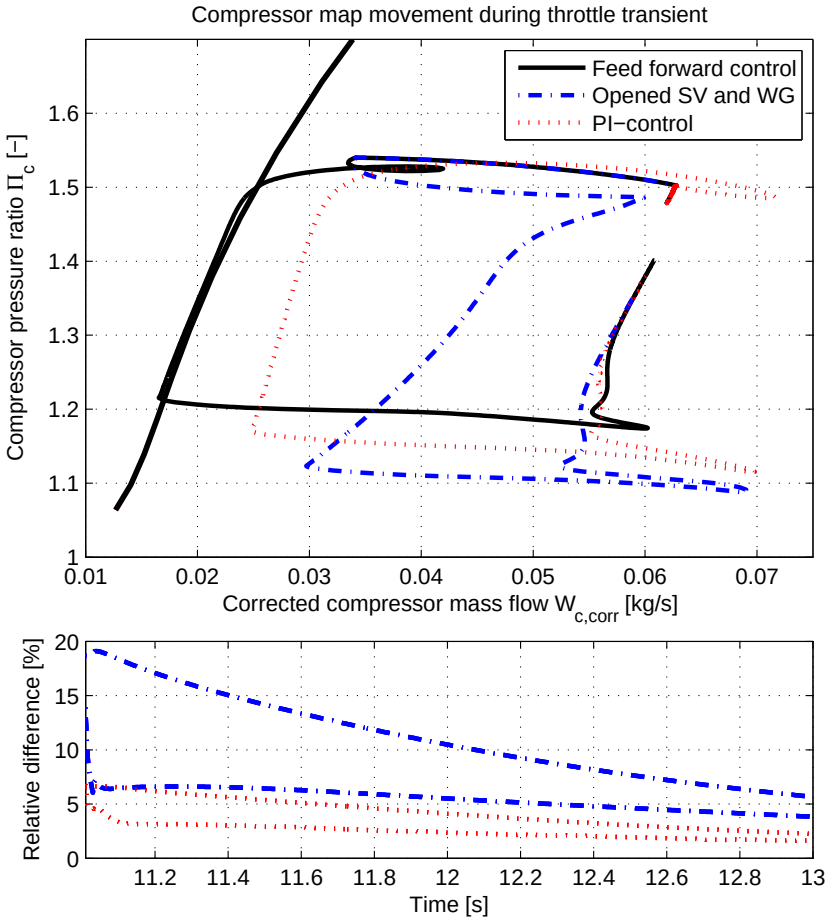

Figure 10: The figure shows different compressor map movements in corrected quantities for the three different controllers described in section 5. The feedforward controller map movement is closest to the SL and the corresponding relative increase in both shaft speed as well as engine torque after the gear change is seen. The shaft speed difference is at most 20% between the feedforward controller and the simple "blow open"-controller.

An investigation is conducted to find the optimal compressor map movement that will maintain as high turbo shaft speeds as possible during rapid throttle transients. The investigation shows that, for every shaft speed, the path of least consumed torque coincides with the surge line.

A throttle transient during a gear change is used as a test case in a simulation setup. A new controller based on feedforward and the TTS concept is compared to two other controllers; a fast control system using feedback and a simple "blow-open"-controller. Comparisons show the gains with a feedforward system. The increase in shaft speed and engine net torque when the next gear is engaged is found to be 20% and 8% respectively compared to the simplest "blow-open"-controller.

A Nomenclature

State	Description	Unit
p_{af}	Air filter control volume pressure	Pa
T_{af}	Air filter control volume temperature	K
p_c	Compressor control volume pressure	Pa
T_c	Compressor control volume temperature	K
p_{ic}	Intercooler control volume pressure	Pa
T_{ic}	Intercooler control volume temperature	K
p_{im}	Intake manifold control volume pressure	Pa
T_{im}	Intake manifold control volume temperature	K
p_{em}	Exhaust manifold control volume pressure	Pa
T_{em}	Exhaust manifold control volume temperature	K
p_{es}	Exhaust system control volume pressure	Pa
T_{es}	Exhaust system control volume temperature	K
N_{tc}	Turbo shaft speed	$\frac{1}{min}$
W_c	Compressor mass flow	$\frac{kg}{s}$
Symbol	Description	Unit
V	Volume	m^3
CV	Control Volume subscript	
R	Specific gas constant	$\frac{J}{kgK}$
D_c	Compressor diameter	m
L_c	Compressor duct length	m
η_c	Compressor efficiency	$-$
γ	Ratio of specific heats	$-$
Π_c	Compressor pressure ratio	$-$
W_{th}	Throttle mass flow	$\frac{kg}{s}$
τ	1st order system time constant	
$init$	Initial condition subscript	
Tq_c	Compressor torque	Nm

References

[1] L. Guzzella, U. Wenger, and R. Martin. IC-engine downsizing and pressure-wave supercharging for fuel economy. *SAE Technical Paper 2000-01-1019*, 2000.

[2] E. Hendricks. The analysis of mean value engine models. *SAE Technical Paper No. 890563*, 1989.

[3] Lars Eriksson, Lars Nielsen, Jan Brugård, Johan Bergström, Fredrik Pettersson, and Per Andersson. Modeling of a turbocharged SI engine. *Annual Reviews in Control*, 26(1):129 – 137, 2002.

[4] Lars Eriksson. Modeling and control of turbocharged SI and DI engines. *Oil & Gas Science and Technology - Rev. IFP*, 62(4):523–538, 2007.

[5] P. Andersson. *Air Charge Estimation in Turbocharged Spark Ignition Engines*. PhD thesis 989, Department of Electrical Engineering, Linköpings Universitet, Linköping, Sweden, 2005.

[6] J. Bergström and O. Leufven. Surge modeling and control of automotive turbochargers. Master's thesis LiTH-ISY-EX-3999, Department of Electrical Engineering, Linköpings Universitet, Linköping, Sweden, June 2007.

[7] E. Wiklund and C. Forssman. Bypass valve modeling and surge control for turbocharged SI engines. Master's thesis LiTH-ISY-EX-3712, Department of Electrical Engineering, Linköpings Universitet, Linköping, Sweden, August 2005.

[8] E. M. Greitzer. The stability of pumping systems - The 1980 Freeman Scholar Lecture. *ASME Transactions Journal of Fluids Engineering*, 103:193–242, June 1981.

[9] E. Hendricks. Isothermal vs. adiabatic mean value SI engine models. In *3rd IFAC Workshop, Advances in Automotive Control, Preprints, Karlsruhe, Germany*, pages 373–378, March 2001.

Paper 2

Engine Test Bench Turbo Mapping[†]

2

Oskar Leufven and Lars Eriksson

Vehicular Systems, Department of Electrical Engineering,
Linköping University, S-581 83 Linköping,
Sweden.

Abstract

A method for determining turbocharger performance on installations in an engine test bench is developed and investigated. The focus is on the mapping of compressor performance but some attention is also given to the turbine mapping. An analysis of the limits that an engine installation imposes on the reachable points in the compressor map is performed, in particular it shows what corrected flows and pressure ratios can be reached and what these limitations depend on. To be able to span over a larger region of the corrected flow a throttle before the compressor is suggested and this is also verified in the test bench.

Turbocharger mapping is a time consuming process and there is a need for a systematic process that can be executed automatically. An engine and test cell control structure that can be used to automate and monitor the measurements by controlling the system to the desired operating points is also proposed.

In experiments, used for constructing the compressor speed lines, it is virtually impossible to control the turbocharger to the exact corrected speed that is postulated by the speed line. To overcome this two methods that compensate for the deviation between measured speed and the desired speed are proposed and investigated. Detailed data from a gas stand is used to evaluate the measurements compared to those that are generated in the engine test cell installation. The agreements are generally good but there is more noise in the engine data and there are also some small systematic deviations.

[†]This is a formatted version of "Engine Test Bench Turbo Mapping" by Oskar Leufven and Lars Eriksson, SAE Technical Paper 2010-01-1232, SAE World Congress and Exhibition 2010, Detroit, USA

1 Introduction

Downsizing and turbocharging of SI engines plays an important role when developing fuel efficient vehicles. To further reduce fuel consumption and emissions more advanced and complicated concepts are being investigated and used, such as for example two-stage charging. In the development of the engine and its control system the information about turbocharger performance plays an important role. Turbocharger performance is expressed using maps, as representations and tabulated data, that are often provided by the compressor and turbine manufacturers or they can also be determined in a gas stand.

Turbocharger performance characteristics are not always readily available, and the manufacturer gas stand measurements are, in some cases, not reliable or can be influenced by the engine installation. Differences occur between stationary gas stand maps and on-engine performance, due to for example flow pulsations, flow geometry differences, and heat transfer. Another situation that frequently occurs when modeling turbocharged engines is that the provided manufacturer map is insufficient, i.e. it only covers a small portion of the operating region. There is thus a demand for turbocharger maps among researchers and engine developers.

To meet this demand this paper develops and investigates methods for measuring and determining turbocharger performance on installations in an engine test bench. This has wide applicability. For example the procedure helps determine the performance on the engine test stand and the mapping also provides valuable input to the modeling where the interaction between the engine and turbocharger is also visible.

2 System description and turbo maps

This section describes the engine test cell system that is used in the study as well as general compressor and turbine maps with examples. A detailed turbo map that is larger than normal manufacturer maps will be presented.

2.1 System description

The engine test bench used is an electric dynamometer that is capable of both motoring and braking the engine as well as emulating driveline transients. It is however, in the mapping, only run in brake mode and under constant speeds. The engine is a 4 cylinder, 2 liter, direct injected, spark ignited engine that is equipped with variable cam phasing for both intake and exhaust valves. Furthermore it has a two stage prototype turbo system fitted to it. However the two stage system is only used in single stage mode in the turbo mapping investigation here.

The engine control system is a prototype system capable of changing all relevant control signals in real time. Compared to a standard turbo-charged gasoline engine this particular engine is equipped with an extra butterfly valve throttle upstream of the first compressor stage. This throttle is also controlled by the control system. An overview of the system is shown in Fig. 1.

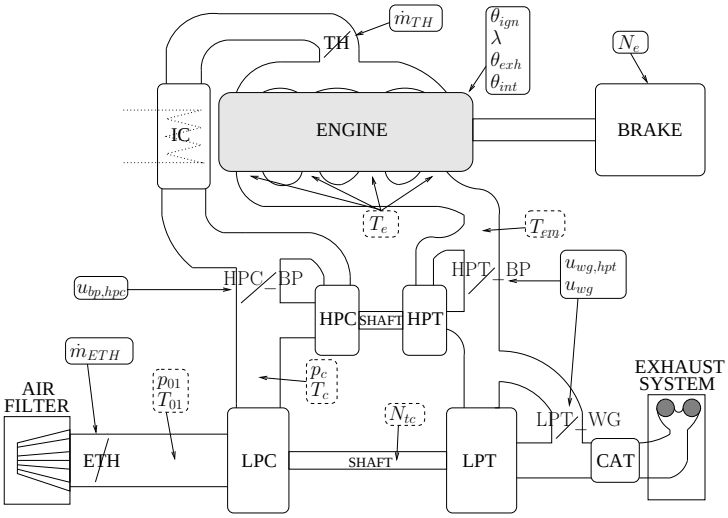

Figure 1: Illustration of the two stage system connected to the engine brake. Note especially the location of the extra throttle at the inlet of the first compressor stage. Also shown in the figure are the, main, available control signals (in solid rectangles) as well as the important system states (in dashed rectangles).

2.2 Compressor and turbine maps

A typical compressor map is shown in Fig. 2, which is a graphical representation of the measurement data that is provided by the manufacturer, see [14, 15] for more examples of maps. Procedures for determining turbo performance, in gas stands, are given in for example [10, 11].

The compressor map in Fig. 2 is not the same as the one on the engine, but it is larger than a normal manufacturer map. It thus both gives a better view of the turbo characteristics and is also more suitable for the analysis of the reachable region. The performance variables $\Pi_c = \frac{p_{02}}{p_{01}}$ and η_c in (25) are described using the corrected quantities in (26). In the compressor map corrected flow $\dot{m}_{c,corr}$,

$$\dot{m}_{c,corr} = \dot{m}_c \frac{\sqrt{\frac{T_{01}}{T_{std}}}}{\frac{p_{01}}{p_{std}}} \tag{1}$$

is on the x-axis, pressure ratio, Π_c on the y-axis, solid lines show constant corrected speed $N_{tc,corr}$

$$N_{tc,corr} = N_{tc} \frac{1}{\sqrt{\frac{T_{01}}{T_{std}}}} \tag{2}$$

The dotted lines show iso-efficiency lines for η_c.

A turbine map is shown in Fig. 3, which shows expansion ratio $1/\Pi_t$, efficiency η_t, and corrected compressor mass flow $\dot{m}_{t,corr}$.

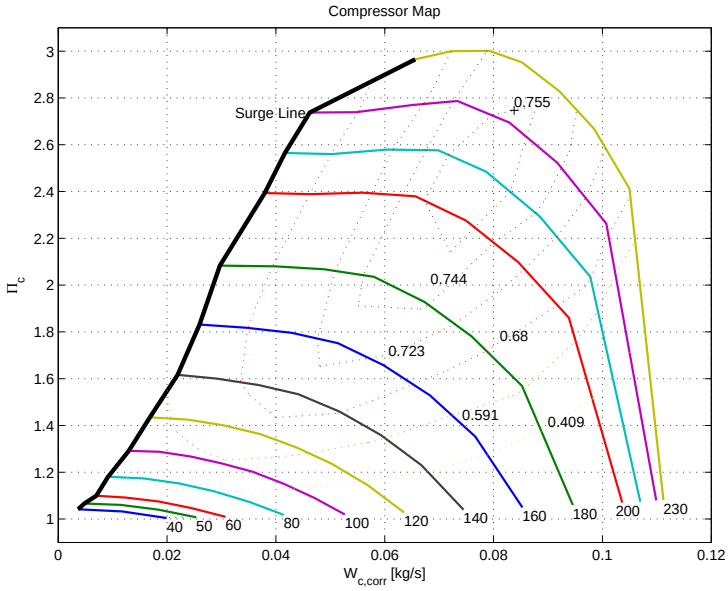

Figure 2: Compressor map showing the compressor efficiency map as a function of the pressure ratio Π_c and corrected mass flow $\dot{m}_{c,corr}$, with lines of constant corrected speed, and the surge line. The numbers $40 - 230$ are the shaft speeds given in $kRPM$.

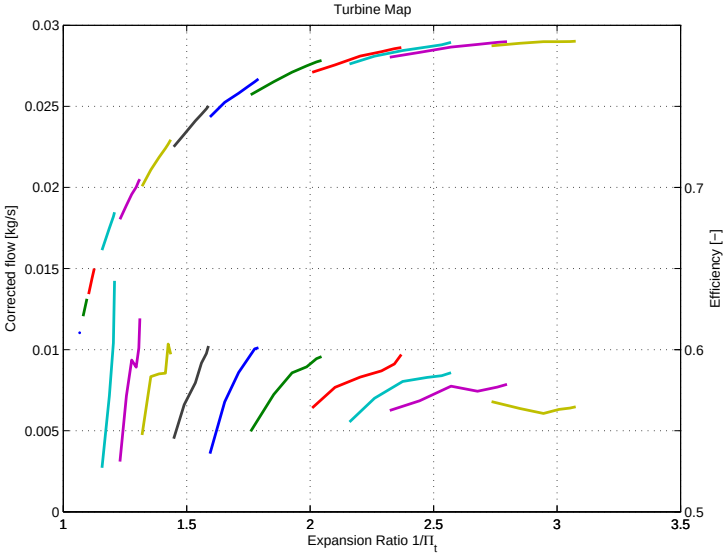

Figure 3: Turbine map showing the flow characteristic and the efficiency, for various lines of constant corrected speed. The x-axis gives the expansion ratio $1/\Pi_t$, the left y-axis the corrected mass flow $\dot{m}_{t,corr}$, and the right y-axis gives the efficiency.

3 Measurements

3.1 Gas stand measurements

The gas stand turbo map, used for experimental validation of the proposed method, has 12 operating points on each of the total 9 constant compressor speed lines. The measurements were done on another turbo individual but of the same model as the one installed on the engine, there can however be discrepancies between different individuals.

3.2 Engine test stand measurements

The measurements were conducted using both a MicroAutoBox (dSPACE) as well as a VXi (HP) system with Kistler pressure sensors and Pentronic thermoelements and the data was bias compensated using cold measurements. The sampling frequencies used were 80[Hz] and 1[kHz] depending on signal measured. Mass flow was measured with both a hot wire sensor as well as a laminar flow meter on the cold inlet air. The turbine mass flow was estimated using the compressor air mass flow and fuel flow calculated from a wide-band lambda signal. Furthermore the wastegate spring was assumed to fully close the wastegate valve in the turbine mapping measurements.

No extra thermal insulation was provided, the installation was kept as close to a production system as possible. This implies that temperatures measured in the engine test stand were influenced by heat transfer, both due to convection, conduction as well as radiation.

Pressures were measured with static pressure taps and the total pressure was calculated using the pipe area and mass flow. For cross sections where exact measurements were not available the areas were approximated, given outer dimensions and estimated thickness.

The measurements were taken when the system was stabilized, which took up to 10-15 minutes depending on operating point. Data was recorded during multiple days and using the same fuel quality. The signals were low pass filtered using non-phase-shifting filters offline.

4 Engine test bench imposed limits

Compared to gas stand turbo mapping there are obviously some differences when mapping a turbo system on an engine test stand. These limits are described in this section. This is followed by a theoretical investigation as well as a experimental investigation. The limits are

- $T_{exh} < T_{exh,lim}$, exhaust temperature limit for turbine protection
- $p_c > p_{amb}$, due to that soft pipes, after the compressor stage, would otherwise collapse
- $N_{tc} < N_{tc,lim}$, turbocharger over speeding protection
- $\Delta T_c = T_c - T_{af}$, temperature rise over compressor stage
- $\lambda_{min} < \lambda < \lambda_{max}$, air-fuel-ratio limitations due to stable combustion and stable power delivery to the turbine

- The variable cam-phasing were actuated in order to ensure stable combustion and stable power delivery to the turbine
- $N_e < N_{e,lim}$, engine speed upper bound
- $Tq_e < Tq_{e,lim}(N_e)$, engine torque limit
- $A_{wg} \leq A_{wg,max}$ wastegate opening area is limited
- $\dot{m}_t$-determination, no mass flow measurements on the "hot" side

Listed limits are imposed on the system by the test stand setup and not by the proposed method.

5 Theoretical investigation of limits

This section presents a theoretical investigation of the reachable operating region for the turbo setup given an engine setup with its limits.

5.1 Turbine inlet temperature

The temperature of the gases leaving the engine, T_e is in [4] well described by an affine function in mass flow

$$T_e = T_{cyl,0} + \dot{m}_e K_t \tag{3}$$

where $(T_{cyl,0}, K_t)$ are tuning constants. This holds as long as the air-to-fuel-ratio is kept at unity ($\lambda = 1$). The exhaust temperature is reduces through heat transfer when passing the exhaust valves and through the exhaust manifold. This leads to a lower turbine inlet temperature than predicted by Eq. (3). This temperature loss is modeled in [4], and it is described by

$$T_{em} = T_a + (T_e - T_a)\, e^{-\frac{h(\dot{m}_e)\, A}{\dot{m}_e\, c_p}} \tag{4}$$

where T_a is the external temperature, $h(\dot{m}_e)$ effective heat transfer coefficient, A pipe wall surface area, and c_p specific heat at constant pressure.

To avoid turbine damage the control system tries to control the gas temperature through fuel enrichment, i.e. $\lambda < 1$. This cools the gases through increased fuel vaporization as well as increasing the mass that is heated by the combustion. Fig. 4 shows the turbine inlet temperature as function of mass flow where fuel enrichment has been used to limit the temperature for larger mass flows.

This insufficient exhaust enthalpy limits the reachable compressor region, in particular a lower temperature moves the limit away from the surge line as shown in Fig. 5.

For small mass flows though, it is possible to increase T_e by moving away from optimal ignition angle and simply start the combustion later. This lowers the engine efficiency since less energy is extracted from the gas during the expansion stroke, thus increasing the temperature of the gas that enters the exhaust system T_e, see e.g. [7, 9].

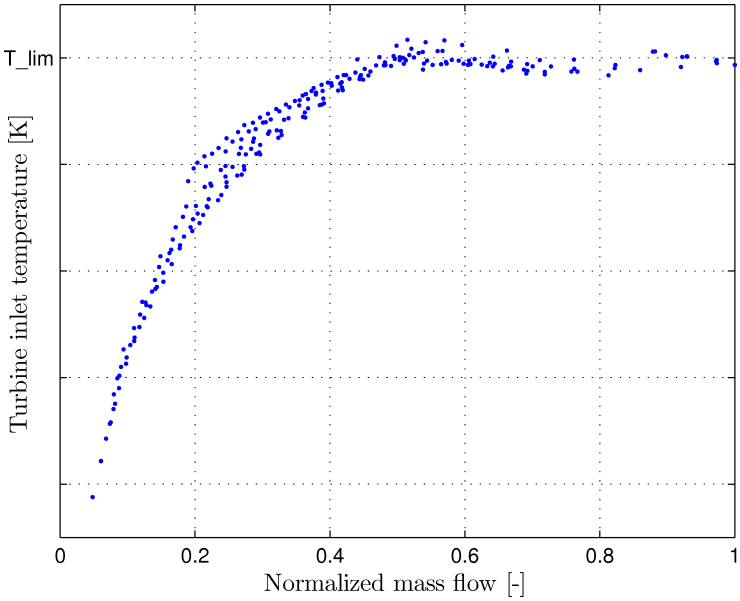

Figure 4: Measured exhaust temperature with temperature control through fuel enrichment.

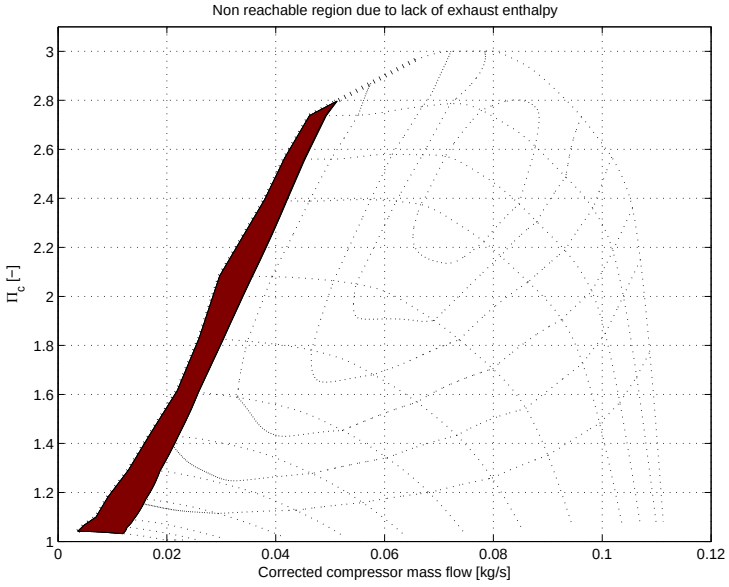

Figure 5: The limited exhaust temperature limits the amount of energy that can be provided for the compressor and thereby reduces the reachable region. The dark region, is due to this, unreachable.

5.2 Turbine mass flow

The turbine will extract power even for a fully opened wastegate valve. This is due to the fact that the effective opening area of the wastegate valve is limited. A pressure ratio will thus effectively be established as soon as there is a mass flow in the system, putting a restriction on how small turbo speed that is achievable given a mass flow. On the other hand, for a fully closed wastegate valve the compressor could be driven into the unstable region for some mass flow. Using the equation for a compressible restriction [7] to describe the wastegate mass flow

$$\dot{m}_{wg} = \frac{p_{em}}{\sqrt{RT_{em}}} A_{wg} C_d \Psi(\Pi_t) \tag{5}$$

it is easy to see how a finite A_{wg} will limit the control of how much power that is extracted by the turbine. For a stable turbo operating points the compressor power P_c and the turbine power P_t must be equal, i.e.

$$\underbrace{\dot{m}_c c_{p,c} T_{01} \frac{\Pi_c^{\frac{\gamma_c - 1}{\gamma_c}} - 1}{\eta_c}}_{=P_c} = \underbrace{\dot{m}_t c_{p,t} T_{03} (1 - \Pi_t^{\frac{\gamma_t - 1}{\gamma_t}}) \eta_t}_{=P_t} \tag{6}$$

where the mechanical efficiency is included in η_t. This equation can be used together with a model for the compressor and turbine and Eq. (5) to gain insight into how the wastegate area limits the reachable operating points in the compressor map. In Fig. 6 these equations are solved for different values of A_{wg}. It is assumed that the turbine inlet temperature is kept at the maximum allowable. This is normally not the case for smaller mass flows as shown in Fig. 4, but can be achieved through later ignition angles as discussed previously. The region to the left of $A_{wg} = 0$ in Fig. 6 is restricted due to that even with fully closed wastegate there is not enough power to reach larger speeds. The left most line corresponds to fully closed wastegate and the other have increasing area. For a given system the maximum area $A_{wg,max}$ gives a limit on how far down in the compressor map the system can operate. For a given maximum value of $A_{wg,max}$ there is therefore a lowest turbo speed given for a given mass flow.

5.3 Turbine mass flow measurement

The wastegate valve has to be closed, since the air mass flow is only measured on the intake side giving the following turbine mass flow

$$\dot{m}_t = \dot{m}_a + \dot{m}_f = \dot{m}_a \left(1 + \frac{1}{(A/F)_s \lambda}\right) \tag{7}$$

Note that this flow can be distributed through both the wastegate and turbine unless the wastegate is closed. This restriction, combined with the fact that the wastegate valve spring is unable to close the valve for large expansion ratios, limits the reachable turbine map considerably. Large deviations from $\lambda = 1$ were avoided in the turbine mapping, due to the possible introduction of measurement errors and uncertainties in the calculation of γ. This limits the turbine mapping since the exhaust temperature limit is reached earlier when fuel enrichment is not allowed.

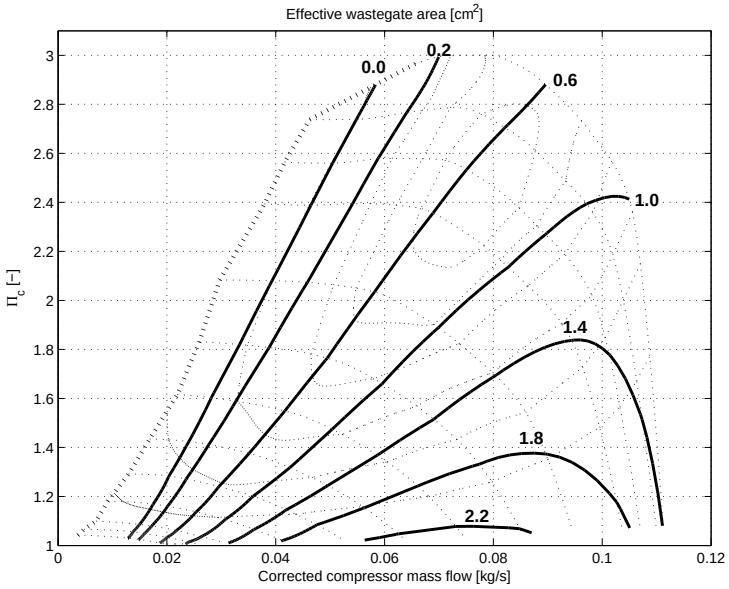

Figure 6: A figure showing the coupling between wastegate area and the position in the compressor map. The left most line depends on the turbine inlet temperature and it has been selected as the highest allowed turbine temperature.

5.4 Compressor temperature increase

If the compressor is driven in an operating point with too large pressure ratio in combination with a too small efficiency the temperature rise over the compressor stage, $\Delta T_c = T_c - T_{01}$, will exceed the allowable limit for the system.

$$\Delta T_c = T_{01} \frac{\Pi_c^{\frac{\gamma-1}{\gamma}} - 1}{\eta_c} \tag{8}$$

The allowable region of the compressor map can be determined using this equation and the compressor map that contains the pressure ratio and efficiency. The result is presented in Fig. 7.

5.5 Flexible pipes

Due to that the pipes downstream of the compressor are flexible there will be a minimum absolute compressor pressure, p_c. This is due to the deformation of the pipes when $p_c < p_{amb}$. The following must therefore hold for all operating points

$$p_{01} \cdot \Pi_c = p_c > p_{amb} \tag{9}$$

This limit can be reached for lower turbo speeds since these have smaller Π_c for a given mass flow.

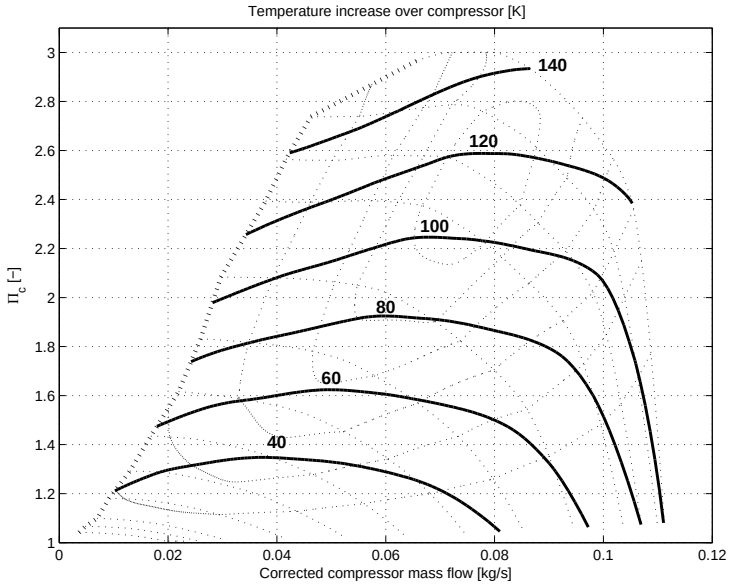

Figure 7: The plots shows the limit in compressor map resulting from the restriction in temperature rise over the compressor stage. Shown are lines of constant temperature increase.

5.6 All Constraints Overlaid

When combining the constraints that have been discussed one will receive a map similar to Fig. 8. In this figure the limits have been chosen to be very restrictive, to better show the contributions from each restriction. There are three limiting factors shown in the figure. The first one to the left, comes from the limited reachability using fully closed wastegate combined with maximum exhaust system temperature. The upper limit is due to the temperature increase limit of the compressor stage. The lower limit is due to a limited opening area of the wastegate valve.

Apart from these limitations there are also others that have to be accounted for. The combustion must be stable to supply a stable enough mass flow to the turbine. This restricts the control of fuel enrichment and spark timing as well as the cam phasing. There is also a limit due to the extra throttle combined with the need to keep $p_c > p_{amb}$; for small Π_c, the pressure at the compressor inlet can not be too low. The combustion engine may not exceed its limits on power and torque. Other natural limits are surge, choke and over speeding of the turbo. However these last ones are also equally applicable in a gas stand and are therefore not further discussed.

5.7 Extensions using pre-compressor throttle

Here it is assumed that the SAE-correction equation can be used, i.e. Eq. (1) and (2). (It is worth to note that there are typesetting errors in the SAE-standards [10, 11] that are derived from the normal quantities in [3].) A larger region

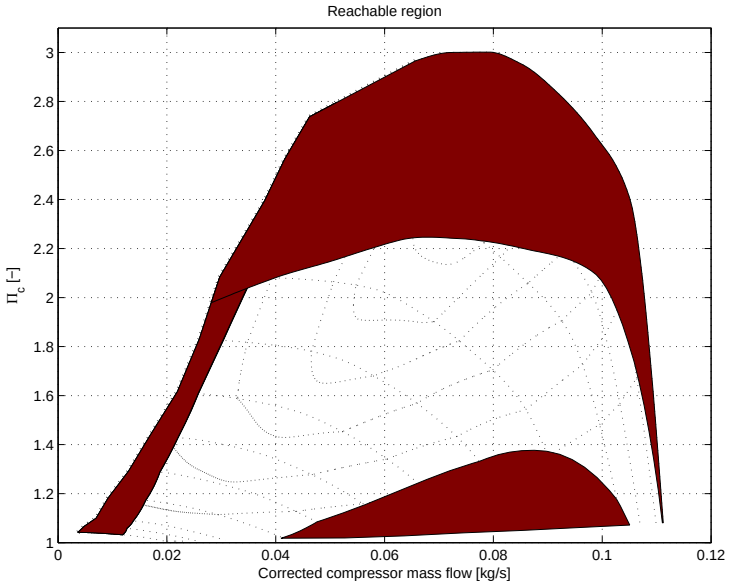

Figure 8: All constraints that have been discussed are now overlaid in the compressor map, showing the reachable set of operating points.

of the compressor map can spanned, using the $\frac{p_{01}}{p_{std}}$-factor in the denominator, compared to maintaining the inlet conditions close to the standard pressure and temperature (p_{std} and T_{std}). This is here recognized as an opportunity and used as a key feature of the proposed method. A pre-compressor throttle is used to lower the pressure before the compressor inlet, thus effectively increasing the corrected mass flow while keeping the actual mass flow within its limits.

The ability to change p_{01}, and thus P_c through Eq. (6), can also be used to achieve turbine speeds unreachable for standard conditions. This applies to small mass flows where P_t would otherwise be too small to reach the desired speed given the loading P_c with $p_{01} \approx p_{amb}$.

6 Turbo Mapping Method

Gas stand turbo mapping normally measures speed lines from choke to surge. As seen in section 4 and 5 this is not achievable for all speed lines when the turbo is mounted in an engine test stand. The engine test stand mapping therefore starts with finding the extreme points that are reachable, i.e. points 1 and 4 or 5 in Fig. 10. It is then decided how many points that are to be measured on the current desired corrected speed line ($N_{tc,corr,des}$), and starting at point 1 the reference values for corrected compressor mass flow ($\dot{m}_{c,corr,des}$) are fed to the control structure, seen in Fig. 9. Depending on mass flow, different actuators are used for control.

The overall structure of the mapping controller consists of three different controllers and they are all shown in Fig. 9. The proposed structure uses feed-

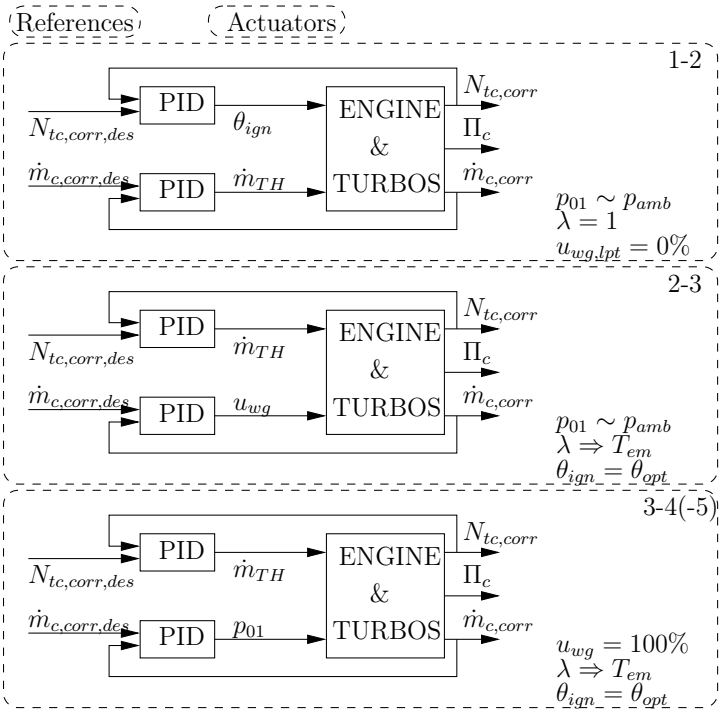

Figure 9: A control structure for the engine test stand turbo mapping. The numbers (e.g. 1-2) are presented in Fig. 10 and described in section 6. Three different controllers are used on different parts of a speed line. For example the top most controller is used between points 1-2 where θ_{ign} is used to effectively control exhaust enthalpy and thus, with fully closed wastegate valve ($u_{wg} = 0\%$), controlling turbo shaft speed ($N_{tc,corr}$). $\dot{m}_{c,corr}$ is controlled using the main throttle mass flow ($\dot{m}_{TH}$) since the pressure upstream of the compressor is kept at ambient ($p_{01} = p_{amb}$). The proposed structure uses feedback and PID controllers for $(\dot{m}_{c,corr}, N_{tc,corr})$.

back and PID controllers for the desired points on the speed line specified by $(\dot{m}_{c,corr,des}, N_{tc,corr,des})$. The function of each controller is described in the list below (where the numbers referred to are shown in Fig. 10)

(1-2): $\theta_{ign} \neq \theta_{opt}$ to increase available turbine energy is used combined with $u_{wg} = 0\%$ to achieve the desired corrected shaft speed, $N_{tc,corr,des}$. λ is kept at the standard conditions given by the engine control system. $\dot{m}_{c,corr}$ is controlled using $\dot{m}_{TH}$. The extra throttle keeps the pressure upstream of the compressor stage at maximum, i.e. $p_{01} \approx p_{amb}$.

(2-2b-2c-3): nominal engine conditions, where u_{wg} controls $N_{tc,corr,des}$. $\dot{m}_{c,corr}$ is controlled using $\dot{m}_{TH}$. At point 2b the temperature forces the use of $\lambda < 1$ to control the exhaust temperature (when $\theta_{ign} = \theta_{opt}$). For higher $N_{tc,corr,des}$ an increase in mass flow can be limited due to difficulties in keeping a stable combustion caused by too small λ, indicated by 2c in Fig. 10.

(3-4): At point 3 the engine utilizes fully opened wastegate valve. $\dot{m}_{c,corr}$

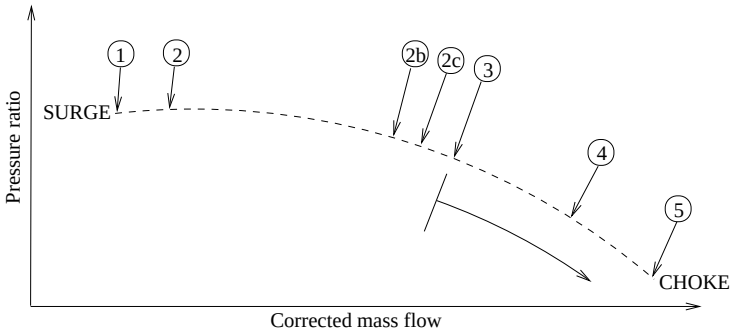

Figure 10: A generic compressor speed line, showing the different controller regions used in the compressor mapping, limited by the surge and choke point. The x-axis is the corrected mass flow, the y-axis shows pressure ratio. The regions made up by the encircled numbers are given by different system limitations and are explained in section 6. The extra throttle upstream of the first compressor stage is used from point 3 and on down to choke, marked with an arrow.

is instead controlled using the extra throttle which controls the inlet pressure, $p_{01} < p_{amb}$.

(4-5): For smaller turbo speeds, $N_{tc,corr}$, there is a limitation caused by the intake system of the engine that makes the measuring of larger mass flows, given the reference compressor speed, impossible. This is due to the soft pipes of the engine that forces the pressure after the compressor to always be greater than the ambient ($p_c > p_{amb}$).

During the turbine mapping the control signals are limited to, mainly, main throttle mass flow, $\dot{m}_{TH}$. This is due to the restrictions described in the Sections 4 and 5. The major limiting factor is the decision to keep $\lambda \approx 1$ and $u_{wg,lpt}$. The extra throttle has only a small influence on the achievable mass flow for the turbine mapping as it can reduce the compressor power by decreasing p_{01} below p_{amb}.

7 Correction Factors for Measurements

Compressor speed lines give a good description of the compressor flow characteristics and therefore plays an important role when selecting a compressor for a particular system. However when performing experiments and building up a speed line in engine tests it is virtually impossible to control the system to the exact corrected speed as is postulated by the speed line. Variations around the nominal speed is inevitable when constructing the maps, and depending on the variations it might be necessary to compensate for these variations. See Fig. 11 for an illustration. The amount of variations differs and for a gas stand the variations are small but for an engine installation the variations are larger and they distort the speed lines.

To solve this problem of map generation two methods are proposed and investigated for how to correct a measured data point with $N_{tc,corr}$ to the desired

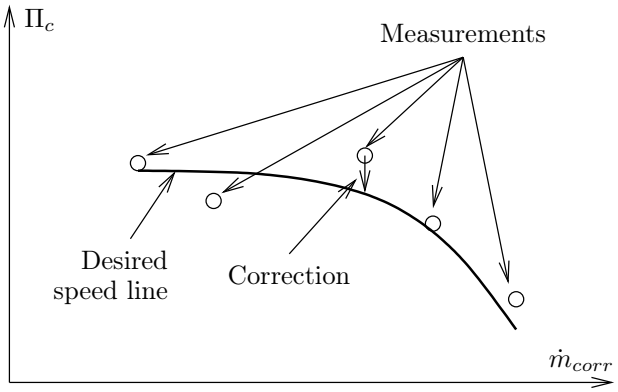

Figure 11: Example of a speed line and measurement points scattered around this line. The correction is desirable to perform such that the final product of the mapping will give a correct picture of the device performance.

speed $N_{tc,corr,des}$. In the first method the compressible dimensionless numbers are utilized and gives an adjustment that is motivated from the physics, that does not rely on any model parameters. The other utilizes a model when performing the correction. There are also other corrections that have been proposed for measurements of stationary machines, e.g. in [2].

7.1 Correction by Dimensionless Numbers

It is well known that the dimensional analysis gives valuable insight into the dominating effects and characteristics of turbomachinery and it is also the basis for the corrected quantities that are used in the maps. The two most important quantities are the energy transfer coefficient

$$\Psi = \frac{c_p\, T_{01} \left[\Pi_c^{\frac{\gamma-1}{\gamma}} - 1 \right]}{N^2\, D^2} \tag{10}$$

and the flow coefficient

$$\Phi = \frac{\dot{m}_c}{\rho_{01}\, N\, D^3} \tag{11}$$

Some material about the dimensionless numbers is collected in Appendix A.

The cornerstone in this method comes from the observation that both Ψ and Φ have only a very weak dependence on N (or equivalently the Mach number). This observation has been utilized in several models [1, 5, 13] for compressor modeling. Since these dimensionless numbers have only a weak dependence on N this can be used to adjust the map data. This is now utilized to determine how a speed change will influence the mass flow and pressure ratio for the same values of Ψ and Φ. This can be expressed mathematically as

$$\Delta\Psi = 0 \tag{12}$$

$$\Delta\Phi = 0 \tag{13}$$

It is worth to comment that one could allow Ψ and Φ to change and for example determine the variation along a constant flow path (as will be done in the pressure ratio model below). However this would require a model (i.e. an assumption) for how Ψ and Φ are connected along a speed line. A less restrictive assumption is that Ψ and Φ remain the same (i.e. Eq. (12) and (13)).

The changes in pressure ratio and mass flow can now be approximated with the aid of the Taylor expansion of Eq. (10) and (11) with respect to the corresponding changes in $\Delta\Pi_c$, $\Delta\dot{m}_c$, and ΔN. The first order Taylor expansion yields

$$\begin{aligned}\Delta\Psi &= \frac{c_p\, T_{01}}{N_{tc}^2\, D^2}\left(\frac{\gamma-1}{\gamma\,\Pi_c^{\frac{1}{\gamma}}}\Delta\Pi_c - 2\left[\Pi_c^{\frac{\gamma-1}{\gamma}}-1\right]\frac{\Delta N_{tc}}{N_{tc}}\right)\\ \Delta\Phi &= \frac{1}{\rho_{01}\, N_{tc}\, D^3}\left(\Delta\dot{m}_c - \dot{m}_c\frac{\Delta N_{tc}}{N_{tc}}\right)\end{aligned}$$

Using Eq. (12) and (13) now yield the changes in pressure ratio and mass flow that are associated with a change in speed

$$\frac{\Delta\Pi_c}{\Pi_c} = 2\frac{\gamma_c}{\gamma_c-1}\left[1-\Pi_c^{-\frac{\gamma_c-1}{\gamma_c}}\right]\frac{\Delta N_{tc}}{N_{tc}} \tag{14}$$

$$\frac{\Delta\dot{m}_c}{\dot{m}_c} = \frac{\Delta N_{tc}}{N_{tc}} \tag{15}$$

These expressions directly give the change from measurable quantities and are easy to apply directly to the data. For example when adjusting the data to a certain desired corrected speed line we get $N_{tc,des} = N_{tc,corr,des}\sqrt{\frac{T_{01}}{T_{std}}}$ and $\Delta N_{tc} = N_{tc,des} - N_{tc}$. In summary this correction relies upon measured quantities and the dimensional analysis together with the assumption of weak dependence of speed in the dimensionless quantities.

A correction that has a similar structure is proposed in [2], where the correction terms are expressed as

$$\frac{\Pi_{c,2}}{\Pi_{c,1}} = \left(\frac{N_2}{N_1}\right)^2 \tag{16}$$

$$\frac{\dot{V}_{c,2}}{\dot{V}_{c,1}} = \left(\frac{N_2}{N_1}\right) \tag{17}$$

where these relate the pressure ratio and volume flows to the rotational speed. For small changes these two expressions are similar to those in Eq. (14) and (15), which can be seen by Taylor expanding the expressions, but they are not identical.

7.2 Corrections With a Pressure Ratio Model

Another option for performing the correction analysis is to use a model for the connection between the pressure ratio, corrected mass flow, and corrected speed. Such a model can be expressed as follows

$$\Pi_c = f_{\Pi_c}(\dot{m}_{c,corr}, N_{tc,corr}) \tag{18}$$

This model structure also covers surge capable models, where the speed line expresses the ideal pressure that the compressor can generate. Here the user of the model can select among a variety of models, e.g. physically based models, curve fitting models, interpolation models. When the model structure has been determined its parameters can be determined (as long as the model is identifiable) with the aid of the least squares method.

Now it is straight forward to calculate the partial derivative of $\Pi_c = f_{\Pi_c}(\dot{m}_{c,corr}, N_{tc,corr})$ with respect to $N_{tc,corr}$ and we have the resulting expression

$$\Delta\Pi_c = \frac{\partial f_{\Pi_c}(\dot{m}_{c,corr}, N_{tc,corr})}{\partial N_{tc,corr}} \Delta N_{tc,corr} \tag{19}$$

This is a straight forward approach as long as there is a model available and that it is differentiable with respect to the corrected speed. The model structure should be selected such that it gives a good description of the data and it is of course beneficial if it is easily differentiable w.r.t. $N_{tc,corr}$.

Looking at Eq. (18) it is tempting to think that one could also use a model that has the following structure

$$\dot{m}_{c,corr} = f_{\dot{m}_{c,corr}}(\Pi_c, N_{tc,corr})$$

However this does not turn out to be a good choice, which is easily seen near the surge line or at higher speeds where it is difficult to define a unique function $f_{\dot{m}_{c,corr}}$. If one is successful in defining such a model in any way the flat lines close to the surge line will give a large partial derivative with respect to $N_{tc,corr}$ and this will make the transformation very sensitive to noise in measurement data and model parameters.

8 Experimental results

First the two correction approaches are illustrated, then the compressor flow and efficiency characteristics are examined, and finally the turbine map is investigated.

8.1 Correction factors

In the first approach everything is given while in the second approach a model structure is necessary. As model a simple polynomial is selected, that has a third order dependence in corrected mass flow and second order dependence in compressor speed.

$$\begin{aligned} f_{\Pi_c}(x, y) = \quad & a_9\, x^3 + a_8\, x^2\, y + a_7\, x\, y^2 + a_6\, x^2 + a_5\, x\, y + \\ & + a_4\, y^2 + a_3\, x + a_2\, y + a_1 \end{aligned}$$

This model is easily tuned to the measurement data with the aid of the (linear) least squares method and the partial derivative is also easy to calculate. For the compressor gas stand map the proposed polynomial gives a mean relative

Π_c-error between model and mapped value of $< 3\%$ with a largest value of 14%. The resulting partial derivative with respect to $N_{tc,corr}$ is

$$\begin{aligned}\Delta\Pi_c &= (a_8\dot{m}_{c,corr}^2 + 2a_7\dot{m}_{c,corr}N_{tc,corr} + a_5\dot{m}_{c,corr} + \\ &\quad +2a_4N_{tc,corr} + a_2)\cdot\Delta N_{tc,corr}\end{aligned}$$

The results are shown in Fig. 12 and presented in the following table

$\frac{\Delta N_{tc,corr}}{N_{tc,corr}}$ [-]	$\frac{\Delta N_{tc}}{N_{tc}}$ [-]	$\Delta\Pi_{c,1}$ [-]	$\Delta\dot{m}_{c,1}$ [g/s]	$\Delta\Pi_{c,2}$ [-]
−0.04	−0.04	−0.001	−0.032	−0.001
0.04	0.04	0.001	0.032	0.001
−0.37	−0.37	−0.005	−0.277	−0.008
1.19	1.19	0.015	0.879	0.024

The table shows the last 4 points of the upper speed line of Fig. 13. $\Delta\Pi_{c,1}$[-] and $\Delta\dot{m}_{c,1}$[g/s] are the correction quantities calculated using the dimensionless numbers, i.e. Eq. (14) and (15) and $\Delta\Pi_{c,2}$[-] is calculated using Eq. (19). Since $N_{tc,corr}\,C = N_{tc}$[-] and $N_{tc,corr,des}\,C = N_{tc,des}$[-] with $C = \sqrt{T_{01}/T_{std}}$ the following holds

$$\begin{aligned}\frac{\Delta N_{tc}}{N_{des}} = \frac{N_{tc,des} - N_{tc}}{N_{des}} = \frac{N_{tc,corr,des}\,C - N_{tc,corr}\,C}{N_{tc,corr}\,C} = \\ = \frac{N_{tc,corr,des} - N_{tc,corr}}{N_{tc,corr}} = \frac{\Delta N_{tc,corr}}{N_{tc,corr}}\end{aligned}$$

and the two first columns in the table will be the same. A negative $\Delta N_{tc,corr}$ for example produces a negative correction, $\Delta\Pi_{c,2}$[-] for the pressure ratio as expected. The largest deviation, ΔN_{tc} for this turbo shaft speed was 1.19%.

8.2 Compressor map

The measured and corrected compressor map is shown in Fig. 13 and parts are magnified in Fig. 12. Both the pressure characteristics as well as the efficiency curves agree well for the speed lines shown. The major restrictions for reaching larger mass flows on these speed lines was the fully opened throttle utilized combined with the problem with keeping $p_c > p_{amb}$ to ensure that the soft pipes were kept intact. The mean absolute relative errors in efficiency and pressure ratio for the two speed lines presented are $\Delta\eta_c = (3.1, 1.7)\%$ and $\Delta\Pi_c = (0.7, 0.6)\%$ for the smaller and larger speed respectively.

In Fig. 12, the uppermost engine test stand point has the largest actual mass flow from the engine test stand mapping. From that point on the extra throttle is used to decrease upstream pressure and thus increasing the corrected mass flow, marked with an arrow (see Fig. 10). The lowest pressure ratio point, with largest corrected mass flow, has about 3% lower actual flow and about 30% lower upstream pressure. This clearly shows the benefit of the proposed additional throttle.

It has to be noted that the measurements were on purpose conducted without any extra insulation which, at least for small speeds, affects especially η_c (see

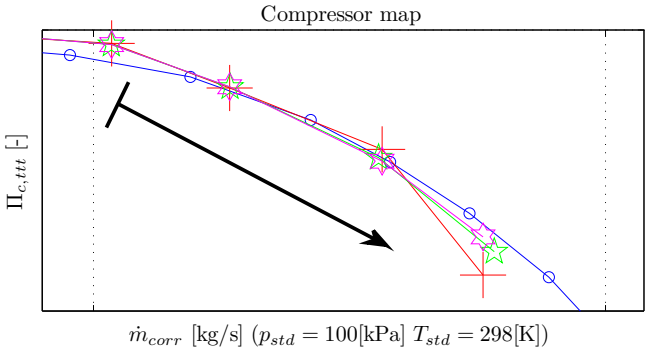

Figure 12: Illustration of the two correction methods. Blue circles show the measurement points from the gas stand. Red crosses show the measured data, green pentagrams corrections according to Eq. (14) and (15), and magenta hexagrams represent corrections according to Eq. (19). The point with largest mass flow is measured at a too small N_{tc} as well as $N_{tc,corr}$ which is seen in the figure were both correction methods increase Π_c, as expected. The first method (pentagrams) shows also deviation in corrected flow.

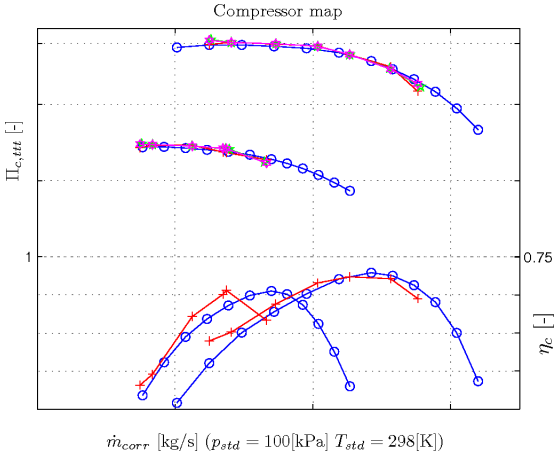

Figure 13: The compressor map measured using the proposed method compared to the gas stand map. Compared to the standard compressor map presentation it has here been chosen to not plot the compressor efficiency as contours. A "turbine map" approach is chosen instead to better see the differences. The upper two curves are the speed lines, whereas the lower lines show the efficiency. Two different constant corrected speed lines are shown. The pressure characteristics agree well for lower mass flows but start to differ for larger mass flows. Both proposed correction methods are shown. The efficiency curves are also well represented but differ slightly for the smallest and largest mass flows as well. $\Pi_c = 1$ as well as $\eta_c = 0.75$ are shown for reference on respective side.

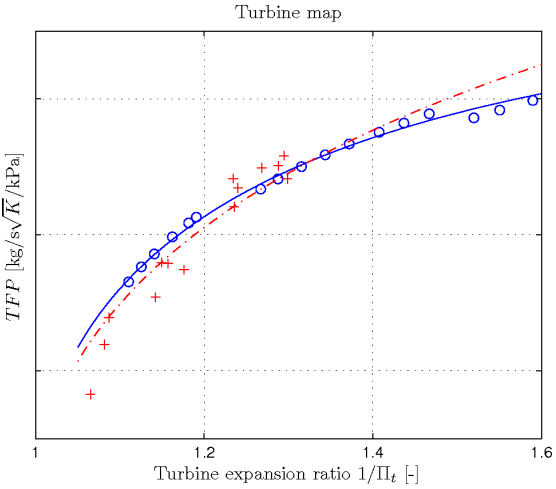

Figure 14: This figure shows the turbine map measured in the engine test stand (red crosses and dashed dotted line) compared to the map measured in the gas stand (blue circles and solid line). The reachable pressure ratios are though, as described in the text, rather limited. The two lines are a least squares fitted standard model ($\dot{m}_t = c_1\sqrt{1-\Pi_t^{c_2}}$, see e.g. [6]) to better show the differences.

[12]). Other aspects affecting the result is that the installation restricted the sensor placement and number of sensors which can lead to errors, in the pressure and temperature measurements, due to flow patterns.

8.3 Turbine map

The turbine map is shown in Fig. 14 where it is seen that the mass flow is slightly underestimated for small flows and slightly overestimated for large. As seen in the figure the turbine map agrees acceptable for the measured points. The turbine efficiency was calculated using

$$\eta_t = \frac{\dot{m}_c c_{p,c}(T_c - T_{01})}{\dot{m}_t c_{p,t} T_{em}\left(1-(\Pi_t)^{\frac{\gamma_t-1}{\gamma_t}}\right)}$$

from e.g. [7], where the mechanical efficiency is included in the turbine efficiency, η_t. This however overestimated η_t. Values exceeding 1 and in general 15% or more too large values were estimated, which is a well known problem for low flows in turbines. These values are therefore left out of Fig. 14. Note though that, due to the limitations only a small turbine map was measured. The largest limitation was the decision to maintain $\lambda = 1$ and not use fuel enrichment to not exceed the exhaust system temperature limit.

9 Conclusions and comments

A procedure for turbo mapping in engine test benches has been proposed and the potential of such a setup has been analyzed and investigated. The setup has

been implemented in an engine test cell and the performance has been studied. The added extra throttle upstream of the first compressor stage is shown to increase the reachable region of the turbo map.

It is shown that the procedure produces turbocharger performance data that matches well with those from a gas stand. The compressor map has been given most attention in the paper, but the turbine flow capacity is also studied.

A theoretical analysis shows how the engine operating limits are transformed to the reachable points in the compressor performance map. One important result is that it is beneficial to have a throttle at the compressor inlet, which will increase the reachable region in terms of the corrected compressor mass flow. The results from the theoretical analysis are confirmed experimentally.

A control structure based on SISO controllers is also proposed and it shows how the turbocharger and engine test bench can be controlled in a systematic manner to support the performance mapping procedure. This control structure has been applied in the engine test cell.

Two methods for adjusting the measured compressor data, when there are deviations between the measured speed and that which is desired when constructing a speed-line, have been proposed and investigated. The results show that the description of the speed line is improved and it was most clear for higher flows.

References

[1] Andersson, P. (2005). *Air Charge Estimation in Turbocharged Spark Ignition Engines*. PhD thesis 989, Department of Electrical Engineering, Linköpings Universitet, Linköping, Sweden.

[2] Chapman, K. S. and Shultz, J. (2003). Guidelines for: Testing large-bore engine turbochargers. Technical report, The National Gas Machinery Laboratory, Kansas State University, 245 Levee Drive.

[3] Dixon, S. (1998). *Fluid Mechanics and Thermodynamics of Turbomachinery*. Butterworth-Heinemann, fourth edition.

[4] Eriksson, L. (2002). Mean value models for exhaust system temperatures. *SAE Transactions, Journal of Engines, 2002-01-0374*, 111(3).

[5] Eriksson, L. (2007). Modeling and control of turbocharged SI and DI engines. *Oil & Gas Science and Technology - Rev. IFP*, 62(4):523–538.

[6] Eriksson, L., Nielsen, L., Brugård, J., Bergström, J., Pettersson, F., and Andersson, P. (2002). Modeling of a turbocharged SI engine. *Annual Reviews in Control*, 26(1):129 – 137.

[7] Heywood, J. (1988). *Internal Combustion Engine Fundamentals*. McGraw-Hill series in mechanical engineering. McGraw-Hill.

[8] Lewis, R. I. (1996). *Turbomachinery Performance Analysis*. Arnold.

[9] Nilsson, Y., Eriksson, L., and Gunnarsson, M. (2006). Modelling for fuel optimal control of SI VCR engines. In *Proceedings of New Trends in Engine Control, Simulation and Modelling*, IFP, Rueil-Malmasison, France.

[10] SAE (1995a). SAE J1826 – Turbocharger Gas Stand Test Code. SAE standard.

[11] SAE (1995b). SAE J922 – Turbocharger Nomenclature and Terminology. SAE standard.

[12] Shaaban, S. (2004). *Experimental Investigation and Extended Simulation of Turbocharger Non-adiabatic Performance*. PhD thesis, Leibniz Universität Hannover.

[13] Sorenson, S. C., Hendrick, E., Magnusson, S., and Bertelsen, A. (2005). Compact and accurate turbocharger modelling for engine control. In *Electronic Engine Controls 2005 (SP-1975)*, number SAE Technical Paper 2005-01-1942.

[14] Watson, N. and Janota, M. (1982). *Turbocharging the internal combustion engine*. MacMillan London.

[15] Zinner, K. (1985). *Aufladung von Verbrennungsmotoren. Grundlagen, Berechnungen, Ausführungen*. Springer Verlag.

A Dimensionless Numbers

For compressible flows there is a set of dimensionless numbers that are used in a central way when describing the compressor performance. Their properties and the way that they are used to introduce the corrected quantities are summarized in this appendix.

Dimensional analysis

Dimensional analysis gives insight into what effects and dependencies are important for the performance. In particular the measurements and determination of the turbo charger performance rely upon these to reduce the number of necessary measurements and to give a compact description of the performance.

A major benefit of using dimensionless numbers is that they reduce the amount of expensive measurements needed for determining turbocharger performance. A turbochargers performance is determined from measurements taken at several operating points with given inlet pressure, inlet temperature, mass flow, etc. To be able to use the measured performance we want to know how it changes with for example the inlet pressure, covering low and high altitudes, or temperature covering winter and summer driving. Dimensionless numbers give insight into many of these dependencies and reduces the number of necessary measurements. Furthermore, dimensionless numbers are also directly useful when modeling compressors and turbines.

Dimensionless numbers and their usage for determining turbo-machinery performance is given in [8, 14], and they are summarized below. The three performance parameters: isentropic stagnation enthalpy

$$\Delta h_{01} = c_p \, T_{01} \left[(p_{02}/p_{01})^{(\gamma-1)/\gamma} - 1 \right]$$

efficiency η, and delivered power P have the following functional expressions for a turbo-machine that operates with a compressible working fluid

$$[\Delta h_{01}, \eta, P] = f(D, N, \dot{m}, \rho_{01}, a_{01}, \mu, \gamma)$$

here the performance depends upon D–diameter, ρ_{01}–inlet density, $\dot{m}$–mass flow, N–rotational speed, a_{01}–inlet stagnation speed of sound, μ–dynamic viscosity, γ–ratio of specific heats. Modeling of the compressor is the task of determining the three functions $f(\ldots)$ above. This task is promoted by the dimensional analysis which reduces the dimensions to the following quantities (see e.g. [3])

$$\Psi = \frac{\Delta h_{0s}}{N^2\, D^2} = \quad f_1\left(\frac{\dot{m}}{\rho_{01}\, N\, D^3}, \frac{\rho_{01}\, N\, D^2}{\mu}, \frac{N\, D}{a_{01}}, \gamma\right) \tag{20}$$

$$\eta = \qquad\qquad f_2\left(\frac{\dot{m}}{\rho_{01}\, N\, D^3}, \frac{\rho_{01}\, N\, D^2}{\mu}, \frac{N\, D}{a_{01}}, \gamma\right) \tag{21}$$

$$\hat{P} = \frac{P}{\rho\, N^3\, D^5} = f_3\left(\frac{\dot{m}}{\rho_{01}\, N\, D^3}, \frac{\rho_{01}\, N\, D^2}{\mu}, \frac{N\, D}{a_{01}}, \gamma\right) \tag{22}$$

where $Re = \frac{\rho_{01}\, N\, D^2}{\mu}$ is a form of Reynolds number, ND/a_{01} is called the blade Mach number, and

$$\Phi = \frac{\dot{m}}{\rho_{01}\, N\, D^3} \tag{23}$$

is called the flow coefficient. The full expression for the head coefficient expressed using measured quantities is

$$\Psi = \frac{c_p\, T_{01}\left[\left(\frac{p_{02}}{p_{01}}\right)^{\frac{\gamma-1}{\gamma}} - 1\right]}{N^2\, D^2} \tag{24}$$

Corrected quantities

For an ideal gas the third dimensionless group is substituted into the first, and Ψ is exchanged for pressure ratio. The power parameter is also exchanged for the temperature quotient. With these manipulations the following expressions and variables are used.

$$\frac{p_{02}}{p_{01}}, \eta, \frac{\Delta T_0}{T_{01}} = f\left(\frac{\dot{m}\sqrt{R\, T_{01}}}{D^2\, p_{01}}, \frac{N\, D}{\sqrt{R\, T_{01}}}, Re, \gamma\right) \tag{25}$$

The influence of the Reynolds number is usually small, so it is often disregarded. Finally, when the performance is studied for a machine of given size and given fluid then R, γ, D remain constant and are therefore left out

$$\frac{p_{02}}{p_{01}}, \eta, \frac{\Delta T_0}{T_{01}} = f\left(\frac{\dot{m}\sqrt{T_{01}}}{p_{01}}, \frac{N}{\sqrt{T_{01}}}\right)$$

Note that the independent variables in the last expression are not dimensionless and these quantities are named *corrected mass flow* and *corrected speed*

$$\dot{m}_{corr} = \frac{\dot{m}\sqrt{T_{01}}}{p_{01}}, \qquad N_{corr} = \frac{N}{\sqrt{T_{01}}}$$

Compressor and turbine data are represented using maps with either those corrected quantities given above or the following ones that are also called *corrected mass flow* and *corrected speed*

$$\dot{m}_{corr} = \frac{\dot{m}\sqrt{(T_{01}/T_{\text{ref}})}}{(p_{01}/p_{\text{ref}})}, \qquad N_{corr} = \frac{N}{\sqrt{(T_{01}/T_{\text{ref}})}} \tag{26}$$

where T_{ref} and p_{ref} are reference conditions. In the majority of the turbocharger data reported in this paper the last one is most common but both are used. It is thus important to be very careful when interpreting the performance maps that are provided by manufacturer.

Paper 3

Parametrization and Validation of a Novel Surge Capable Compressor Model for MVEM using Experimental Data[†]

3

Oskar Leufven and Lars Eriksson

November 26, 2010

Vehicular Systems, Department of Electrical Engineering,
Linköping University, SE-581 83 Linköping, SWEDEN.

Abstract

A compressor model is developed. It is capable of representing mass flow and pressure characteristic for three different regions: surge, normal operation as well as for when the compressor acts as a restriction, i.e. having a pressure ratio of less than unity. Different submodels are discussed and methods to parametrize the given model structure are given. Both the parameterization and validation are supported extensively by measured data. Transient data sets include measurements from engine test stands and a surge test stand. The compressor model is further validated against a data base of stationary compressor maps. The proposed model is shown to have good agreement with measured data for all regions, without the need for extensive geometric information or data.

[†]This is a formatted version of "Parametrization and Validation of a Novel Surge Capable Compressor Model for MVEM using Experimental Data" by Oskar Leufven and Lars Eriksson, submitted to the IFAC World Congress 2011, Milano, Italy.

1 Introduction and motivation

A compressor model capable of handling all operating modes is beneficial when investigating control strategies and controller design for turbocharged (TC) engines. The operating modes to cover are: normal operation, compressor surge and choke.

Surge is a dangerous instability and can occur if the throttle is rapidly closed, e.g. during a gear shift under acceleration, where a throttle closing causes a fast reduction in mass flow. The mass flow reduction upstream produces an increase in pressure over the compressor and if the turbo does not slow down fast enough the pressure ratio will be too excessive and the mass flow will revert through the compressor.

Choke can lead to a pressure drop over the compressor. A single stage turbo compressor can be forced to operate with a pressure drop over it during short transients, before it has overcome inertia effects. For a two stage system this can also be obtained if the bypass valve does not function properly, or is forced closed when charging with the first compressor stage. A passively controlled bypass valve, that opens when a pressure drop is created over it, will always give a pressure ratio of less than unity for the second stage, when the high pressure stage is bypassed.

A comparison of other compressor modeling techniques can be found in [1].

1.1 Contribution

Compressor models describing and validated over all three regions simultaneously are, to the authors knowledge, not found in the literature. This paper describes the development and validation of a novel compressor model and its integration in an existing Mean Value Engine Model (MVEM). The developed and implemented model is parametrized using experimental data and finally a validation, also against measured data, is conducted.

1.2 Mean Value Engine Modeling

Component based MVEM of TC spark ignited (SI) engines is outlined in [2] and [3]. The baseline model is developed and validated in [4] and has been extended to handle surge in [5]. The extension utilizes the model by Moore-Greitzer [6] that introduces a compressor mass flow state.

The TCSI model structure, see Figure 1, uses restrictions (air filter, compressor, intercooler, throttle, engine, turbine, exhaust system) interconnected with control volumes, and further extended with surge and wastegate valves. There are 14 states: six pairs of control volume pressures and temperatures, one turbo shaft speed and the compressor mass flow for the surge modeling capability.

1.3 Experimental Data

Experimental data is collected from three different platforms: a compressor driven by a separate electric motor in a surge test stand [7], a compressor as

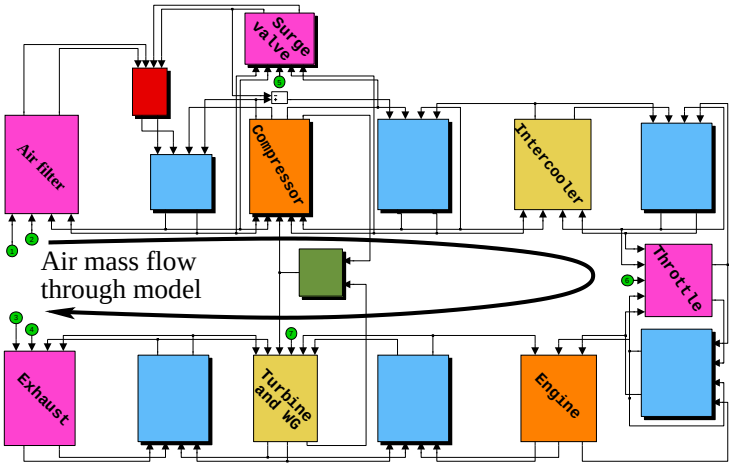

Figure 1: Surge capable MVEM. The mass flow path starts in the air filter and is indicated by the arrow. The different components are interconnected with control volumes. The turbocharger shaft is seen between the compressor and the turbine.

part of a single stage turbocharger installed in a test stand, and a two stage turbocharged engine mounted in an engine test stand.

Compressor maps

SAE-corrected compressor manufacturer maps [8] as well as externally measured maps are also in the evaluation. Most maps use corrected mass flow and shaft speed [9]

$$\begin{aligned} N_{corr} &= \frac{N_{noncorr}}{\sqrt{\mathrm{T}/\mathrm{T}_{\mathrm{std}}}} \\ W_{corr} &= W_{noncorr}\frac{\sqrt{\mathrm{T}/\mathrm{T}_{\mathrm{std}}}}{\mathrm{P}/\mathrm{P}_{\mathrm{std}}} \end{aligned} \tag{1}$$

where p_{std} and T_{std} are referred to as reference conditions which should be given along with the map data.

A map shows what pressure ratio, $\Pi_c = {}^{\mathrm{P}_{\mathrm{aft}}}/_{\mathrm{P}_{\mathrm{bef}}}$, a compressor achieves as a function of W_{corr} and N_{corr}, see Figure 5 for examples of maps. Points of equal N_{corr} are normally connected, giving a compressor speed line (SpL). The compressor adiabatic efficiency η_c is also given for each map point. Points are measured from the smallest mass flow, found at the surge line (SuL), to the largest mass flow where choking can occur. The compressor model in this paper is given in corrected quantities.

1.4 Surge properties

This paper considers full surge, where the compressor mass flow, $W_c < 0$ during parts of a surge cycle. To characterize a surge cycle, the following features are proposed

t_{sc} [s] Cycle time of a surge cycle

$\Gamma_{\Pi_{c,s}}$ [-] ${}^{(\Pi_{\mathrm{c,max}}-\Pi_{\mathrm{c,min}})}/_{(\Pi_{\mathrm{c,max}}-1)}$

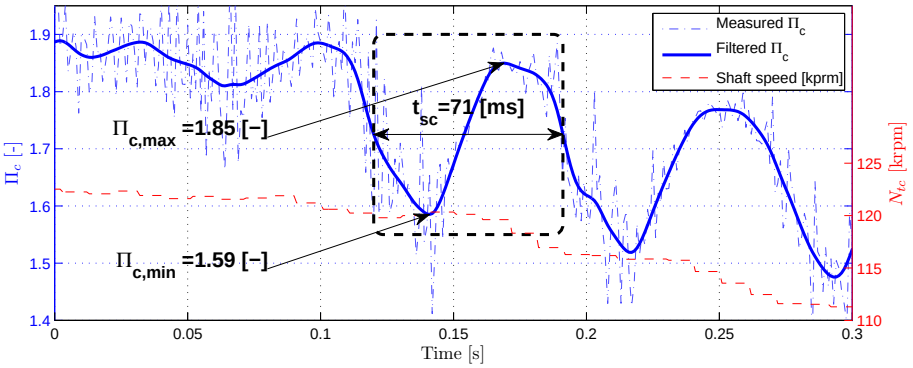

Figure 2: Engine dynamometer measurements showing Π_c for two surge cycles. Solid line is zero phase shift low pass filtered Π_c to easier separate the measurement signal (dash dotted) from the noise. Dashed line shows turbo shaft speed in krpm. The dashed box shows one surge cycle. The surge properties are: $t_{sc} = 71[\text{ms}]$ and $\Gamma_{\Pi_{c,s}} = {}^{(1.85-1.59)}/_{(1.85-1)} = 31[\%]$.

where $\Pi_{c,max}$ and $\Pi_{c,min}$ are largest and smallest Π_c during the surge cycle. These are exemplified using engine test stand measurements in Figure 2, that also shows pressure and shaft speed variations for a typical surge cycle.

2 Compressor model

To include surge capability in the model, the approach in [6] is followed, introducing a state for the compressor mass flow W_c according to

$$\frac{dW_c}{dt} = \frac{\pi D_c^2}{4L_c} \cdot (\hat{p}_c - p_c)\,, \qquad \hat{p}_c = \hat{\Pi}_c \cdot p_{af} \tag{2}$$

where D_c is the compressor diameter, L_c is the duct length, p_c is the pressure in the control volume after the compressor and p_{af} the pressure in the control volume before. $\hat{p}_c$ (and $\hat{\Pi}_c$) is a measure of how much pressure the compressor builds given an operating point.

The compressor model has also other sub models describing: outlet temperature, T_c, and consumed torque, Tq_c

$$\begin{aligned} T_c &= T_{af}\left(\frac{\Pi_c^{\frac{\gamma-1}{\gamma}}-1}{\eta_c}+1\right) \\ Tq_c &= {}^{30}/_{\pi}\frac{(T_c-T_{af})c_pW_c}{N_{tc}} \end{aligned} \tag{3}$$

where γ, c_p are gas properties and η_c is the compressor adiabatic efficiency. The dynamics for the shaft speed N_{tc} is given by the turbo shaft torque balance

$$\frac{d(N_{tc}\pi/30)}{dt} = \frac{1}{J_{tc}}(Tq_t - Tq_c - Tq_{tc,fric}) \tag{4}$$

where Tq_t is torque supplied from the turbine, $Tq_{tc,fric}$ is the shaft friction and J_{tc} is the turbocharger inertia.

3 Ellipse compressor $\hat{\Pi}_c$-model

To model $\hat{\Pi}_c$, a subdivision is made dependent on if W_c is larger or smaller than the SuL mass flow $W_{c,SuL}$, and if $W_c < 0$. SuL for the model is defined as the point on a SpL with positive mass flow that has zero slope.

A normal SpL found in maps has close to zero slope at SuL, and then falls of with increasing slope for increasing W_c. The shape of a SpL is similar to an ellipse. This is used as the basis of the proposed Ellipse model, where the major and minor axis as well as the center point are allowed to vary with N_{tc}. With increasing use of two stage turbo systems, models capable of representing also the flow restriction characteristic of the compressor are needed, see Figure 3. Single stage turbo systems can also operate with $\Pi_c < 1$, e.g. during a transient before the turbo has spun up and built up pressure. The ellipse SpL includes this region. $W_c < 0$ is modeled with a turbine like behavior. The model equations for the three regions are

$$
\begin{cases}
\hat{\Pi}_c & = \left(1 - \left(\frac{W_c - W_{c,SuL}}{W_{c,max} - W_{c,SuL}}\right)^{c_1}\right)^{1/c_2} \hat{\Pi}_{c,SuL} \\
\hat{\Pi}_{c,SuL} & = f_{\hat{\Pi}_{c,SuL}}(N_{tc}) \\
W_{c,SuL} & = f_{W_{c,SuL}}(N_{tc}) \\
W_{c,max} & = f_{W_{c,max}}(N_{tc}) \\
c_j & = f_{c_j}(N_{tc}),\ j = 1,2
\end{cases} \quad W_c > W_{c,SuL}
$$

$$
\begin{cases}
\hat{\Pi}_c & = \hat{\Pi}_{c,0} + b_2 W_c^2 + b_3 W_c^3 \\
\hat{\Pi}_{c,0} & = \hat{\Pi}_{c,SuL} - f_{\Gamma_{\hat{\Pi}_{c,s}}}(N_{tc})(\hat{\Pi}_{c,SuL} - 1) \\
b_2 & = {}^{3(\hat{\Pi}_{c,\mathrm{SuL}} - \hat{\Pi}_{c,0})}/_{\mathrm{W}_{c,\mathrm{SuL}}^2} \\
b_3 & = {}^{-2(\hat{\Pi}_{c,\mathrm{SuL}} - \hat{\Pi}_{c,0})}/_{\mathrm{W}_{c,\mathrm{SuL}}^3}
\end{cases} \quad 0 < W_c < W_{c,SuL}
$$

$$
\begin{cases}
\hat{\Pi}_c & = \hat{\Pi}_{c,0} + \left(1 - \left({}^{\mathrm{W_c}}/_{\mathrm{k_1}}\right)^2\right)^{-1/\mathrm{k_2}} - 1 \\
k_1 & = \frac{W_{c,t}}{\sqrt{1 - \left(\hat{\Pi}_{c,t} - \hat{\Pi}_{c,0} + 1\right)^{-k_2}}}
\end{cases} \quad W_c < 0
\tag{5}
$$

Note that some of the model parameters have a physical meaning: Maximum compressor mass flow at zero pressure ratio ($W_{c,max}$), compressor mass flow at the surge line ($W_{c,SuL}$) and pressure ratio at the surge line ($\hat{\Pi}_{c,SuL}$). The, possibly shaft speed dependent, function $f_{\Gamma_{\hat{\Pi}_{c,s}}}$ describes one of the surge properties proposed in Section 1.4 and determines the pressure build up at zero mass flow, $\hat{\Pi}_{c,0}$. The parameters c_1, c_2 define the ellipse eccentricity. The semi-diameters of the ellipse are given by the points $(W_{c,SuL}, \hat{\Pi}_{c,SuL})$, $(W_{c,SuL}, 0)$ and $(W_{c,max}, 0)$.

The following subsections will describe and motive the functions f_i, were

$$
i \in \left[c_1, c_2, \hat{\Pi}_{c,SuL}, W_{c,SuL}, W_{c,max}, \Gamma_{\hat{\Pi}_{c,s}}\right]
$$

3.1 Ellipse $\hat{\Pi}_c$ parametrization – $W_c > W_{c,SuL}$

Both $W_{c,SuL}$ and $\hat{\Pi}_{c,SuL}$ are expected to increase with shaft speed. Further, for $N_{tc} = 0$ the $W_{c,SuL}$ is expected to be zero, and $\hat{\Pi}_{c,SuL}$ unity respectively. $W_{c,max}$ is expected to converge to a value where choking conditions are reached

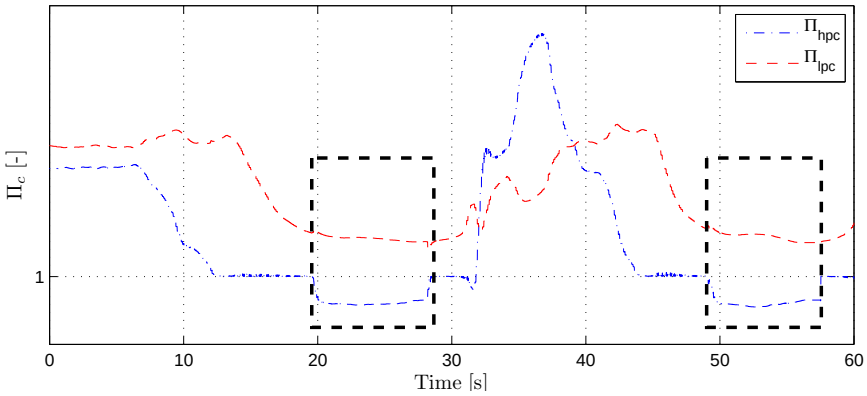

Figure 3: Measured Π_c for both the first and the second stage of a two stage system. Regions having $\Pi_{hpc} < 1$ are marked with boxes. The data motivates the need for a compressor model that also handles $\Pi_c < 1$.

at the compressor inducer. Until choking occurs in the inducer, an increasing trend of $W_{c,max}$ with increasing N_{tc} is expected, see [10].

Functions f_{c_1} and f_{c_2}

The first two parameters of the Ellipse model enable an N_{tc}-dependent eccentricity of the ellipse (compare $\left(\mathrm{W_c - W_{c,s}}/\mathrm{W_{c,max} - W_{c,SuL}}\right)^{c_1} + \left(\hat{\Pi}_{\mathrm{c,s}}/\hat{\Pi}_{\mathrm{c,SuL}}\right)^{c_2} = 1$). To balance model simplicity and descriptive capabilities, the following basis function are proposed

$$\begin{aligned} f_{c_1}(N_{tc}) &= c_{1,0} + c_{1,1}N_{tc} \\ f_{c_2}(N_{tc}) &= c_{2,0} + c_{2,1}N_{tc}^{c_{2,2}} \end{aligned} \tag{6}$$

Function $f_{W_{c,max}}$

For the maximum mass flow a simple first order polynomial is proposed

$$f_{W_{c,max}}(N_{tc}) = W_{c,max,N_{tc}=0} + c_{W_{c,max},1}N_{tc} \tag{7}$$

where $W_{c,max,N_{tc}=0}$ gives a positive flow also for an $N_{tc} = 0$. A minimum selector can be added to physically correspond to a choked inducer flow, W_{ci}, according to

$$\tilde{f}_{W_{c,max}} = min(W_{ci}, f_{W_{c,max}})$$

This was not needed for the compressors of this paper.

Functions $f_{W_{c,SuL}}$ and $f_{\hat{\Pi}_{c,SuL}}$

For surge mass flow

$$f_{W_{c,SuL}}(N_{tc}) = 0 + c_{W_{c,SuL},1}N_{tc}^{c_{W_{c,SuL},2}} \tag{8}$$

and for surge pressure ratio

$$f_{\hat{\Pi}_{c,SuL}}(N_{tc}) = 1 + c_{\hat{\Pi}_{c,SuL},1} N_{tc}^{c_{\hat{\Pi}_{c,SuL},2}} \tag{9}$$

are proposed, where the 0 and 1 emphasize zero flow and unity pressure ratio for $N_{tc} = 0$.

The parameters in (6)-(9) are determined using a nonlinear least square method on a compressor map.

3.2 Ellipse $\hat{\Pi}_c$ parametrization – $W_c < W_{c,SuL}$

First it is recognized that the exact shape of a *SpL* for $W_c \in [0, W_{c,SuL}]$ is not of great importance for the surge behavior, see [11]. It can also be seen in (2), where the change in p_c is given by the emptying and filling dynamic of the downstream control volume, and $\hat{p}_c$ is given by the compressor model. The slope of the compressor characteristic is positive in this region, [6], and the difference $(\hat{p}_c - p_c)$ is therefore large, and the region is traversed fast. The, for surge, important parameter $\hat{\Pi}_{c,0}$ has been recognized in e.g. [12, 13], but is here instead modeled as a function of the parameter $\Gamma_{\hat{\Pi}_{c,s}}$, see (5).

Importance of $\hat{\Pi}_{c,0}$

The motivation for the importance of $\hat{\Pi}_{c,0}$ comes from the fact that the Π_c-trajectory, during deep surge, has to enclose the point $(\hat{\Pi}_{c,0}, W_c = 0)$. This is seen in the second row of (2), i.e.

$$\frac{dW_c}{dt} = \frac{\pi D_c^2}{4L_c} \cdot (\hat{p}_c - p_c)$$

where $\hat{p}_c$ has to lead p_c to increase W_c and take the system out of reversed compressor mass flow. The trajectory is given by the compressor characteristics and the system properties.

To find $\hat{\Pi}_{c,0}$ consider the following. To get $\frac{dW_c}{dt} = 1[kg/s^2]$ a difference of $(\hat{p}_c - p_c) \approx 0.8$kPa is needed, given reasonable values of $D_c = 0.04[m]$, $L_c = 1[m]$. Since $0.8 << 200$kPa, the Π_c-trajectory will pass closely under the $(\hat{\Pi}_{c,0}, 0)$-point, when the compressor is moving out of reversed mass flow. This close connection $\hat{\Pi}_{c,0} \approx \Pi_{c,0}$ means that measurement data of Π_c during surge can be used to assess $\Gamma_{\hat{\Pi}_{c,s}}$. The approximation $\hat{\Pi}_{c,0} \approx \Pi_{c,0}$ needs to be checked for a given application though, since making the $(\pi D_c^2)/4L_c$-factor small means that the difference $(\hat{p}_c - p_c)$ has to be increased, for a given value of $\frac{W_c}{dt}$. Further, the pressure $p_{c,0} = p_{af}\hat{\Pi}_{c,0}$ is the pressure of the downstream control volume needed for the compressor to go from negative to positive W_c, which will affect t_{sc}.

Effect from $\Gamma_{\hat{\Pi}_{c,s}}$, $W_{c,t}$, $\hat{\Pi}_{c,t}$, k_2 on the surge properties

k_1 is given by algebraic constraints (5) forcing all *SpL* through $(W_{c,t}, \hat{\Pi}_{c,t})$. To investigate how the other Ellipse model parameters affect the surge properties

	$\Gamma_{\hat{\Pi}_{c,s}}$	W_{ct}	Π_{ct}	k_2	Param. change
Δt_{sc}	19%(-20%)	-4%(5%)	0%(-1%)	-1%(1%)	+30%(-30%)
	6%(-7%)	-1%(1%)	0%(-0%)	-0%(0%)	+10%(-10%)
$\Delta\Gamma_{\Pi_{c,s}}$	26%(-27%)	1%(-1%)	-0%(0%)	0%(-0%)	+30%(-30%)
	9%(-9%)	0%(-0%)	-0%(0%)	0%(-0%)	+10%(-10%)

Table 1: Sensitivity of the surge properties with respect to changes in the Ellipse model parameters. The parameters are varied $\pm\{10\%, 30\%\}$ from nominal, $t_{sc} = 81$[ms] and $\Gamma_{\hat{\Pi}_{c,s}} = 54\%$.

N_{tc}[krpm]	$mean(W_{th})$[g/s]	$max(\Pi_c)$[-]	$min(\Pi_c)$[-]	$\Gamma_{\Pi_{c,s}}$[-]
80	15.0	1.35	1.17	51%
91	17.8	1.45	1.23	49%
99	21.9	1.53	1.26	51%
110	25.0	1.66	1.33	50%
120	28.5	1.79	1.39	50%
131	30.4	1.96	1.48	50%
140	38.5	2.10	1.54	51%
130	49.0	1.89	1.88	2%
130	42.9	1.90	1.87	3%
131	37.9	1.94	1.82	13%
131	33.0	1.94	1.48	49%
131	30.4	1.96	1.48	50%

Table 2: Surge test stand measurements in normal and continuous surge operation. Upper part: full surge at different N_{tc}. $\Gamma_{\Pi_{c,s}} \approx 50\%$ independent of N_{tc}. Lower part: one N_{tc} with different $mean(W_{th})$. The two last rows show that, for full surge, an increase in $mean(W_{th})$ with 10% only decreases $\Gamma_{\Pi_{c,s}}$ with $< 1\%$.

from Section 1.4, a model of the surge test rigg is used. Each of the parameters $\Gamma_{\hat{\Pi}_{c,s}}, W_{c,t}, \hat{\Pi}_{c,t}, k_2$ are varied $\pm\{10\%, 30\%\}$ from nominal values of $\Gamma_{\hat{\Pi}_{c,s}} = 49\%$, $W_{c,t} = -0.059$, $\hat{\Pi}_{c,t} = 10$ and $k_2 = 0.5$. The resulting sensitivity in the surge properties are summarized in Table 1 and measured surge is compared to a simulation with the nominal values in Figure 7. The most important parameters are found to be $\Gamma_{\hat{\Pi}_{c,s}}$ and $W_{c,t}$.

Surge rigg experimental data

$\Gamma_{\Pi_{c,s}}$ is calculated from continuous surge measurements. Some of the data is presented in Table 2. $\Gamma_{\Pi_{c,s}}$ is found to be $\approx 50\%$ for a wide range of N_{tc} for this compressor. Further, if several data sets with $N_{tc} = const$ are studied in more detail, it is found that once deep surge is established, $\Gamma_{\Pi_{c,s}}$ shows only a small dependence of mean mass flow. The third last row of Table 2 shows $\Gamma_{\Pi_{c,s}}$ for mild surge.

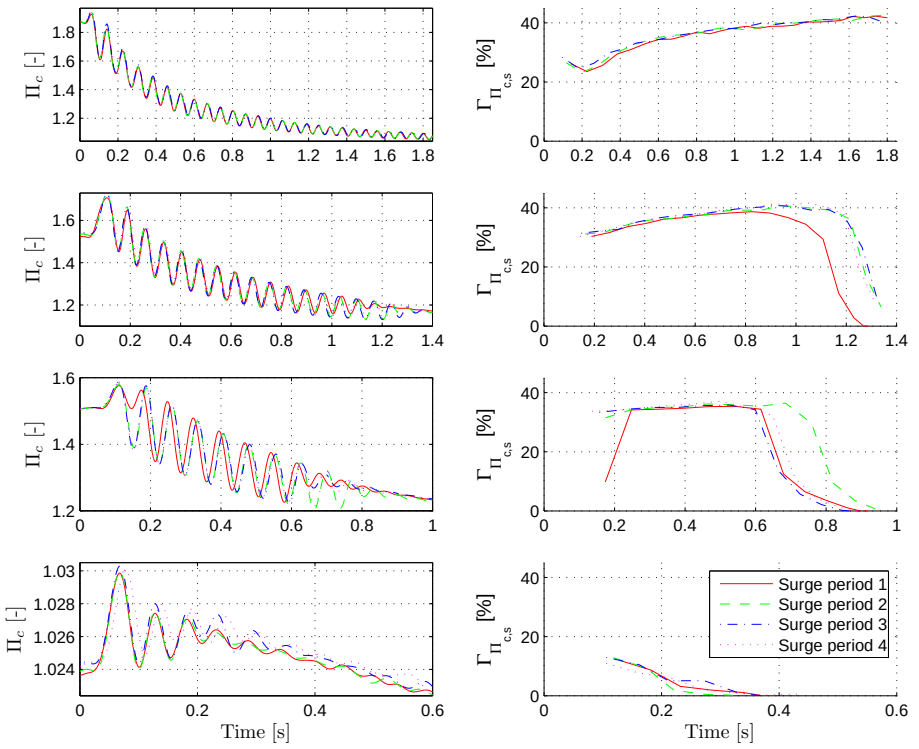

Figure 4: Measured surge in an engine test stand. Each row shows multiple surge periods initiated from the same engine operating point. Initial Π_c decreases from top to bottom. Left: Π_c-traces. Right: Calculated $\Gamma_{\Pi_{c,s}}$. The surge repeatability is remarkable.

Engine test stand experimental data

Figure 4 presents typical surge measurements at tip-out from an engine test stand. It can be seen that when deep surge is established, surge is repeatable with remarkable accurary, although the behavior of the first and last cycles of the surge periods can differ, where some cycles show a mild surge behavior. The right plots shows $\Gamma_{\Pi_{c,s}}$, where a increasing trend in $\Gamma_{\Pi_{c,s}}$ for decreasing Π_c can be seen. When the surge period is over $\Gamma_{\Pi_{c,s}}$ goes to zero. Since N_{tc} decreases during the tip-outs, it is not possible to get a correct value of $\Gamma_{\Pi_{c,s}}$. $max(\Pi_c)$ of Section 1.4 is here taken as the peak following an associated $min(\Pi_c)$-value, giving an approximation of $\Gamma_{\Pi_{c,s}}$. The motivation for choosing the peak afterward is that N_{tc} is approximately constant during the time from a Π_c-dip to the following Π_c-peak, see Figure 8. An increasing trend in $\Gamma_{\Pi_{c,s}}$ can be seen for decreasing Π_c.

No surge data

The experimental data indicates that $\Gamma_{\hat{\Pi}_{c,s}} \approx 35\%$ is a good approximation if no surge data exists. For compressor maps having points with lower mass flow

than (8), another method can be used to shape the speed lines. Given the model structure from (5), nonlinear optimization can be used to find the parameters of $f_{\Pi_{c,0}}$ to obtain best fit to the map points.

4 η_c-model

η_c models can be found in e.g. [14]. However, the six parameter efficiency model, $\eta_{c,6p}$, presented in [4] is used in this paper

$$\begin{cases} \eta_{c,6p} &= \eta_{c_{max}} - \chi^T Q \chi \\ \chi &= \begin{bmatrix} W_c - W_{c_{\eta_{max}}} \\ \sqrt{\Pi_c - 1} - \left(\hat{\Pi}_{c_{\eta_{max}}} - 1\right) \end{bmatrix} \\ Q &= \begin{bmatrix} Q_{11} & Q_{12} \\ Q_{21} & Q_{22} \end{bmatrix},\ Q_{12} = Q_{21} \end{cases} \tag{10}$$

where $W_{c_{\eta_{max}}}, \hat{\Pi}_{c_{\eta_{max}}}, \eta_{c_{max}}, Q_{ii}$ are model parameters. $\eta_{c,6p}$ decreases rapidly outside the normal operating region of the compressor.

For the restriction operating region ($\Pi_c < 1$), and for the surge region a constant efficiency, $\eta_{c,restr./surge}$, is assumed to maintain simplicity of the model. The rapid decrease of the $\eta_{c,6p}$-model outside the normal operating region of the compressor is used to further maintain simplicity of the full η_c-model. For the η_c-model, restrictive or surging operation is assumed when $\eta_{c,6\ param} < \eta_{c,restr./surge}$. The efficiency model can therefore be made up by taking the maximum value of $\eta_{c,restr./surge}$ and $\eta_{c,6p}$. A continuous η_c-function is also obtained. The complete efficiency model is given by

$$\eta_c = max(\eta_{c,6p}, \eta_{c,restr./surge}) \tag{11}$$

4.1 η_c parametrization

Normal and restrictive region

$W_{c_{\eta_{max}}}, \hat{\Pi}_{c_{\eta_{max}}}, \eta_{c_{max}}$ and Q_{ii} of the efficiency model are estimated using nonlinear optimization on compressor maps.

Looking at available data for the region $\hat{\Pi}_c < 1$, a small temperature increase can in fact be seen. This increase is however rather small, $2-4$K. Since the gas expands through the compressor a temperature decrease is expected but this can be counteracted by heat transfer effects. A constant efficiency of 20% is used here, which is also supported in [15].

Surge region

Hints for the compressor efficiency in the surge region can be found in compressor inlet temperature measurements as well as by studying the shaft speed variations during surge. However, a good estimate is hard to achieve due to the slow temperature sensors. This paper proposes to model the efficiency as a constant, since this is found to produce temperature signals with good agreement with measurements. A constant efficiency of 20% is assumed here, which is also supported in [16].

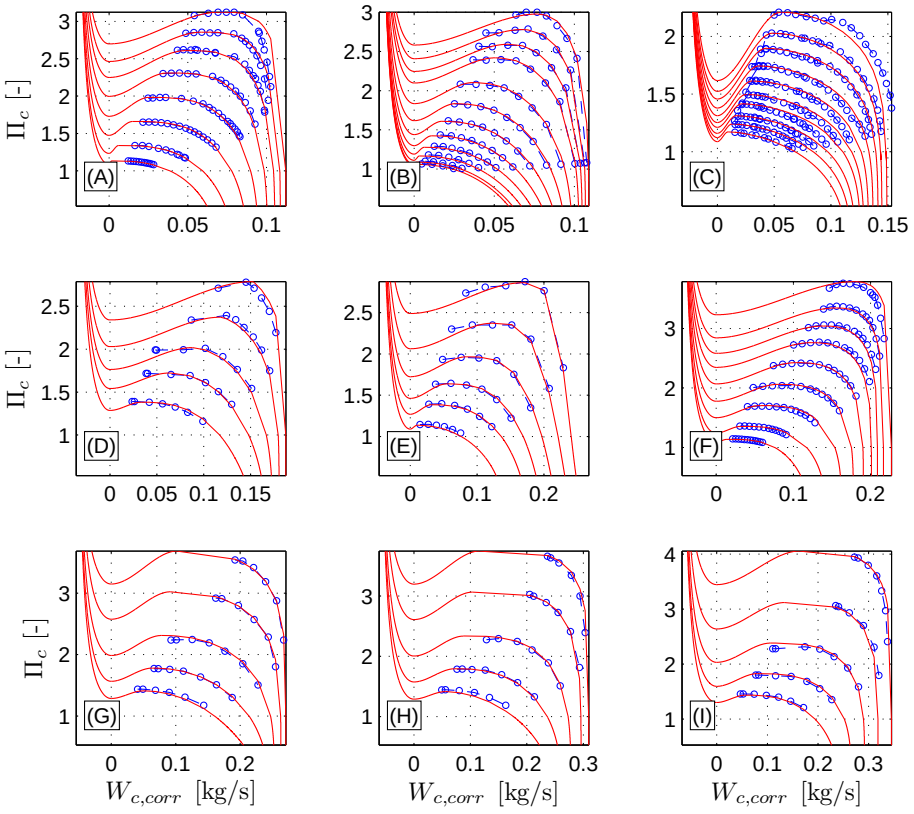

Figure 5: Validation of Ellipse model on nine compressor maps. The presented compressor maps (A-I) range from small (≈ 100g/s) compressors to large (≈ 350g/s) and from both single as well as two stage setups. The overall performance of the model is good over the entire normal operating region.

5 Validation

The validation process is divided into compressor model validations for $\hat{\Pi}_c$ and η_c followed by a full system validation. Due to data availability the same data set is used for both parametrization and validation.

5.1 Ellipse $\hat{\Pi}_c$ validation

$\hat{\Pi}_c$ — Normal region

The Ellipse model performance is presented for nine static compressor maps in Figure 5. The figure is further summarized in Table 3. The automated scripts produce a model with an average relative error of less than 1%, for most points. The largest errors are found for choked mass flows, where the error can be up to 20%.

	$\eta_c > 60\%$			$\eta_c < 60\%$		
Map	mean(e)	std(e)	max(|e|)	mean(e)	std(e)	max(|e|)
(A)	0.43%	0.05%	0.49%	0.31%	0.08%	0.40%
(B)	1.11%	0.27%	1.45%	1.09%	0.00%	1.09%
(C)	-1.14%	0.65%	2.09%	-2.74%	2.66%	8.77%
(D)	-0.10%	1.58%	2.21%	NaN%	NaN%	%
(E)	2.57%	0.50%	3.02%	2.03%	1.56%	3.76%
(F)	0.33%	0.23%	0.77%	0.56%	0.32%	0.79%
(G)	2.04%	0.44%	2.64%	4.53%	0.00%	4.53%
(H)	3.37%	1.58%	5.72%	8.15%	0.00%	8.15%
(I)	1.50%	0.45%	2.23%	2.53%	0.00%	2.53%

Table 3: Mean, standard deviation and magnitude of relative error ($e = (\hat{\Pi}_{\text{Ellipse}} - \hat{\Pi}_{\text{map}})/\hat{\Pi}_{\text{Ellipse}}$) between modeled Π_c and compressor map data, for nine compressor maps. Left: Points with $\eta_c > 60\%$. Right: Points with $\eta_c < 60\%$. The model performance is good, with increasing discrepancy for points with lower efficiency. Map (D) did not contain any points with $\eta_c < 60\%$.

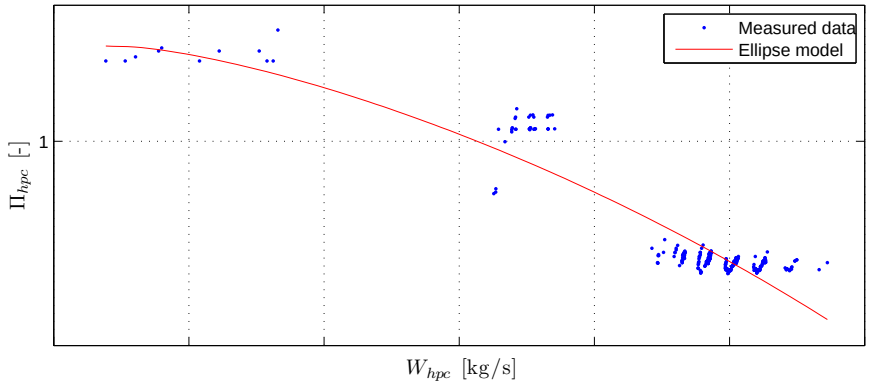

Figure 6: Measurements and simulation of $\Pi_c < 1$ operation. The model representation for $\Pi_c < 1$ is good.

$\hat{\Pi}_c < 1$ – Restriction quadrant

There does not exist much data from compressors operated in this region. The Ellipse model performance is shown in Figure 6, where the agreement with measured data is shown to be good.

5.2 Efficiency model validation

Efficiency – Normal region

To validate the η_c model, the same compressor maps as in Figure 5 are used. Table 4 presents the results. Good performance is obtained for the normal region with $\eta_c > 60\%$, with increasing discrepancy for points with lower efficiency.

	$\eta_c > 60\%$			$\eta_c < 60\%$		
Map	mean(e)	std(e)	max(|e|)	mean(e)	std(e)	max(|e|)
(A)	-0.29%	1.82%	4.76%	0.68%	4.01%	8.11%
(B)	0.04%	4.48%	10.85%	20.38%	30.82%	76.66%
(C)	0.10%	2.36%	8.39%	0.06%	7.64%	24.40%
(D)	-0.50%	3.06%	8.44%	1.24%	4.33%	8.25%
(E)	0.00%	3.83%	8.65%	0.18%	10.09%	24.16%
(F)	-0.37%	2.16%	6.77%	1.21%	3.57%	8.78%
(G)	-0.29%	1.86%	5.56%	1.50%	6.83%	9.90%
(H)	-0.35%	3.55%	12.63%	1.77%	6.42%	10.35%
(I)	-0.33%	2.41%	6.70%	1.76%	7.50%	10.40%

Table 4: Mean, standard deviation and magnitude of relative error ($e = {}^{(\eta_{c,\mathrm{model}} - \eta_{\mathrm{map}})}/_{\eta_{c,\mathrm{model}}}$) between modeled η_c, and compressor map data for nine compressor maps. Left: Points with $\eta_c > 60\%$. Right: Points with $\eta_c < 60\%$. The model performance is good. Data set (B) contains SL points measured down to the flow characteristics of the gas stand, with small values of η_c, while the model has a maximum selector, limiting minimum $\eta_{c,modeled}$ to $\eta_{c,restr./surge}$.

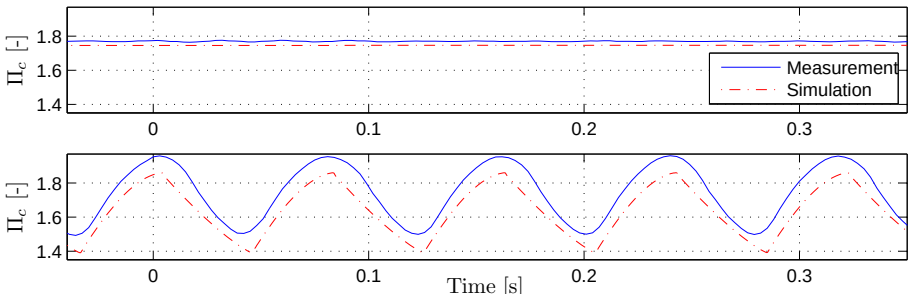

Figure 7: Modeled and measured Π_c, for a constant N_{tc} = 130krpm for two W_{th}. Upper: W_{th} close to surge. Lower: Operating point with full surge. The modeled t_{sc} and $\Gamma_{\Pi_{c,s}}$ are in good agreement.

5.3 Integration performance validation

The developed and parametrized compressor model is incorporated into the MVEM structure developed in [3]. The MVEM library components are combined to build a model of the surge test stand as well as to design a full TCSI engine model.

Surge test stand

The surge test stand model consists of a compressor, two control volumes and a restriction. These are parametrized to correspond to the geometries and physical behavior from measurements. The results are shown in Fig. 7, where it is seen that both t_{sc} and $\Gamma_{\Pi_{c,s}}$ are in good agreement.

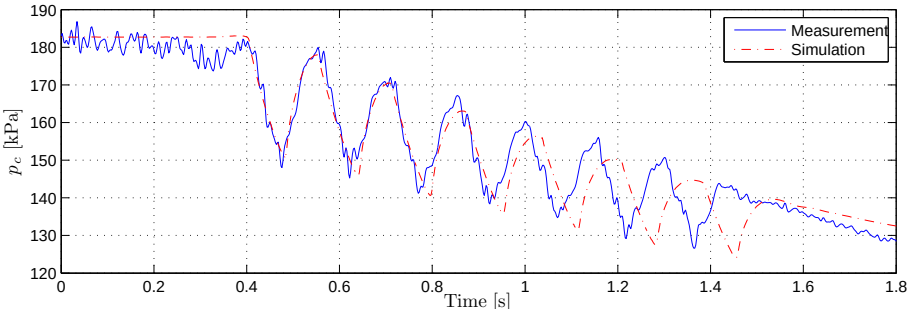

Figure 8: Engine test stand measured and MVEM simulated compressor control volume pressure for a surge transient. The pressure oscillations are well modeled both in amplitude and frequency.

Full engine MVEM surge

The full TCSI MVEM developed in [4] is extended with the Ellipse compressor model. The same engine used to parametrize the MVEM, was driven in surge and measured. These measurements are here compared to the extended MVEM. The measured and modeled compressor control volume pressure are in good agreement, see Figure 8.

6 Conclusions

Normal and choke compressor operation can be modeled using ellipses, and extended to also describe surge operation. The parametrization can be automated given a compressor map and data from surge. The proposed basis functions for the curve fitting are validated on a database of compressor maps, and give good description for a wide range of automotive compressors, both single stage, as well as two stage. The set of basis function are physically motivated, and ensures a sound extrapolation capability. The ellipse model has good performance for normal operation, as well as for surge and operation with pressure ratio of less than unity.

The conclusions of the surge rigg and engine test stand experiments are: If no available surge data exists, a constant value of $\Gamma_{\Pi_{c,s}} \in [30, 50]\%$ will suffice. Further, deep surge cycles are highly repeatable. $\Gamma_{\Pi_{c,s}}$ shows only a small dependency of mean mass flow. Surge pressure oscillations can be seen in measured data down to pressure ratios of close to unity, and is not limited to high pressure ratios/high shaft speeds. Turbo shaft speed is almost constant when going from negative to positive compressor mass flow. The deep surge cycle frequency is mainly given by the emptying and filling dynamics in combination with the compressor characteristics, where pressure build up at zero mass flow is most important.

References

[1] Paul Moraal and Ilya Kolmanovsky. Turbocharger modeling for automotive control applications. SAE Technical Paper 1999-01-0908, March 1999.

[2] Lars Eriksson, Lars Nielsen, Jan Brugård, Johan Bergström, Fredrik Pettersson, and Per Andersson. Modeling of a turbocharged SI engine. *Annual Reviews in Control*, 26(1):129 – 137, 2002.

[3] Lars Eriksson. Modeling and control of turbocharged SI and DI engines. *Oil & Gas Science and Technology - Rev. IFP*, 62(4):523–538, 2007.

[4] P. Andersson. *Air Charge Estimation in Turbocharged Spark Ignition Engines*. PhD thesis 989, Department of Electrical Engineering, Linköpings Universitet, Linköping, Sweden, 2005.

[5] J. Bergström and O. Leufven. Surge modeling and control of automotive turbochargers. Master's thesis LiTH-ISY-EX-3999, Department of Electrical Engineering, Linköpings Universitet, Linköping, Sweden, June 2007.

[6] E. M. Greitzer. The stability of pumping systems - The 1980 Freeman Scholar Lecture. *ASME Transactions Journal of Fluids Engineering*, 103:193–242, June 1981.

[7] J. Andersen, F. Lindström, and F. Westin. Surge Definitions for Radial Compressors in Automotive Turbochargers. *SAE International Journal of Engines*, 1(1):218, 2008.

[8] SAE. SAE J1826 – Turbocharger Gas Stand Test Code. SAE standard, 1995.

[9] SAE. SAE J922 – Turbocharger Nomenclature and Terminology. SAE standard, 1995.

[10] J.T. Gravdahl and O. Egeland. Speed and surge control for a low order centrifugal compressor model. In *Control Applications, 1997., Proceedings of the 1997 IEEE International Conference on*, pages 344 –349, 5-7 1997.

[11] K. E. Hansen, P. Jorgensen, and P. S. Larsen. Experimental and theoretical study of surge in a small centrifugal compressor. *ASME Journal Fluids Engineering*, (103):391–395, 1981.

[12] G. Theotokatos and N.P. Kyrtatos. Diesel engine transient operation with turbocharger compressor surging. 2001.

[13] J.T. Gravdahl, O. Egeland, and S.O. Vatland. Active surge control of centrifugal compressors using drive torque. In *Decision and Control, 2001. Proceedings of the 40th IEEE Conference on*, volume 2, 2001.

[14] J.-P. Jensen, A.F. Kristensen, S.C. Sorenson, N. Houbak, and E. Hendricks. Mean value modeling of a small turbocharged diesel engine. SAE Technical Paper 910070, Detroit, USA, Februar 1991.

[15] M. Müller, S. Sumser, P. Fledersbacher, K. Rößler, K. Fieweger, and HJ Bauer. Using the Centrifugal Compressor as a Cold-Air Turbine. In *8th international conference on turbochargers and turbocharging, Imperial College London*, 2005.

[16] Panagiotis Grigoriadis. *Experimental Erfassung und Simulation instantionärer Verdichterphänomene bei Turboladern von Fahrzeugmotoren*. PhD thesis, Technischen Universität Berlin, 2008.

PAPER 4

Investigation of compressor correction quantities for automotive applications[†]

Oskar Leufven and Lars Eriksson

Vehicular Systems, Department of Electrical Engineering
Linköping University, SE-581 83 Linköping, Sweden.

4

Abstract

Turbo performance is represented using maps, measured for one set of inlet conditions. Corrections are then applied to scale the performance to other inlet conditions. A turbo compressor for automotive applications experiences large variations in inlet conditions, and the use of two stage charging increases these variations. The variations are the motivation for analyzing the correction quantities and their validity. The corrections reveals a novel surge avoidance strategy, where the result is that a reduction in inlet pressure increases the surge margin for eight maps studied. The method to investigate the applicability of the strategy is general.

An experimental analysis of the applicability of the commonly used correction factors, used when estimating compressor performance for varying inlet conditions, is presented. The experimental campaign uses measurements from an engine test cell and from a gas stand, and shows a small, but clearly measurable trend, with decreasing compressor pressure ratio for decreasing compressor inlet pressure. A method is developed, enabling measurements to be analyzed with modified corrections.

An adjusted shaft speed correction quantity is proposed, incorporating also the inlet pressure in the shaft speed correction. The resulting decrease in high altitude engine performance, due to compressor limitations, are quantified and shows a reduction in altitude of $200 - 600$ m, for when engine torque has to be reduced to due limited compressor operation.

[†]This is a formatted version of "Investigation of compressor correction quantities for automotive applications" by Oskar Leufven and Lars Eriksson, submitted to the International Journal of Engine Research.

1 Introduction

Turbocharging and downsizing is a common way to increase engine efficiency, and the turbo performance is important to retain vehicle drivability and consumer acceptance. Turbo compressor performance is characterized by a map, describing the properties of the compressor. The goal with the map, is to describe turbocharger performance, so that it covers the full operating region of the compressor. However, when turbocharger performance is measured, the characteristics obtained are valid for the inlet conditions under which the measurements were conducted. To overcome this deficiency, different correction factors are applied to scale the performance variables to cover other inlet conditions.

The correction factors are based on dimensional analysis of the compression system [1], and are used in the SAE standards [2, 3]. The SAE standards for measuring and correcting turbo data is commonly used in the automotive community. This paper investigates compressor inlet variations and evaluates the accuracy of the SAE correction quantities for the compressor side.

1.1 Outline and contributions

Section 1.2 presents compressor maps, the commonly used inlet corrections, and a compressor model used in the paper. Section 2 contributes with an investigation of inlet conditions for automotive compressors, showing that compressors, especially in a two stage system, experience large variations in correction quantities. Section 2.2 highlights the increase of up to 50 % in air filter pressure drop, due to the decreasing ambient gas density with altitude.

Section 3 contributes with a novel surge avoidance method, and presents altitude dependent engine torque lines, using the nominal corrections. Section 4 presents measurements of compressor performance, at different inlet conditions, from an engine test stand and a gas stand. Section 5 proposes modifications to the commonly used correction quantities, based on the experimental findings and develops a method for analyzing measured data, if the correction quantities are changed. The key result is that an increased fit to measured data is found if also inlet pressure is included in the compressor shaft speed correction.

The effect on the altitude dependent engine torque lines, due to modifications of the corrections are quantified in Section 6. A reduction in altitude of 200 − 600 m, for when engine torque has to be reduced to due limited compressor operation is found.

1.2 Compressor map and inlet correction

A compressor map presents compressor performance data normalized to a reference standard compressor inlet temperature, T_{std} and pressure, p_{std}. These reference conditions are a key component of the map, and must be provided with the map. Frequently used standard conditions are $p_{std} = 100$ kPa and $T_{std} = 298$ K. Standardization documents for how to measure and present corrected map data are given in e.g. [2, 4], and Figure 1 presents an example of a compressor map. The basis for these correction factors come from dimensional analysis (see e.g. [5]), and derivations of the correction factors can be found in

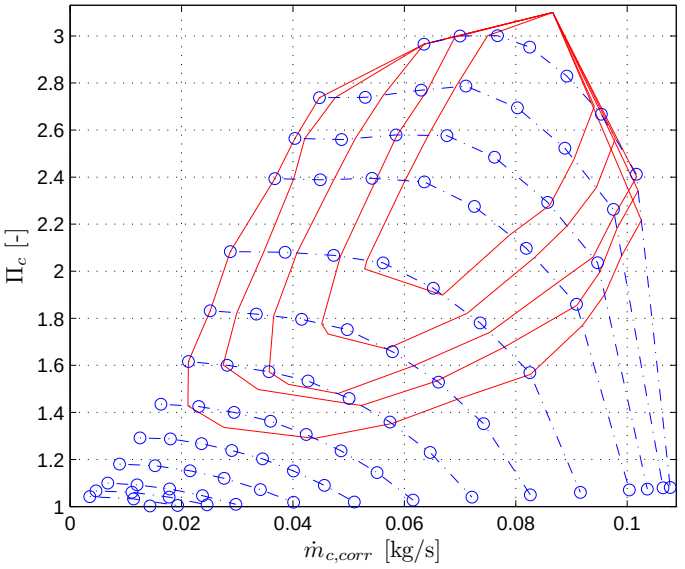

Figure 1: Compressor speed lines shown as dash dotted lines, connecting map points $(\dot{m}_{c,corr}, \Pi_c)$, marked with circles, with equal corrected compressor speed $N_{tc,corr}$. Solid lines show contours of constant compressor adiabatic efficiency η_c.

e.g. [6, 7]. The ratio of actual inlet pressure and temperature to these standard states are used to adjust the performance variables, and are here defined

$$\begin{aligned} \delta &= {}^{\mathrm{p}_{01}}/_{\mathrm{p}_{\mathrm{std}}} \\ \theta &= {}^{\mathrm{T}_{01}}/_{\mathrm{T}_{\mathrm{std}}} \end{aligned} \tag{1}$$

where p_{01} and T_{01} are the compressor inlet pressure and temperature, respectively. Compressor pressure ratio is given by

$$\Pi_c = \frac{p_{02}}{p_{01}} \tag{2}$$

where p_{02} is the outlet pressure. The corrected compressor mass flow is given by

$$\dot{m}_{c,corr} = \dot{m}_c \frac{\sqrt{{}^{\mathrm{T}_{01}}/_{\mathrm{T}_{\mathrm{std}}}}}{({}^{\mathrm{p}_{01}}/_{\mathrm{p}_{\mathrm{std}}})} = \dot{m}_c \frac{\sqrt{\theta}}{\delta} \tag{3}$$

where $\dot{m}_c$ is the compressor mass flow. The corrected compressor speed is given by

$$N_{tc,corr} = N_{tc} \frac{1}{\sqrt{{}^{\mathrm{T}_{01}}/_{\mathrm{T}_{\mathrm{std}}}}} = N_{tc} \frac{1}{\sqrt{\theta}} \tag{4}$$

with actual turbo speed N_{tc}. Points of equal $N_{tc,corr}$ in the compressor map, are usually connected to form what is known as a compressor speed line. Speed lines are measured from the surge line, to the left in the compressor map, to a choked flow, or until η_c has dropped too much, to the right. Connecting the points of each speed line with lowest mass flow approximates the surge line of the

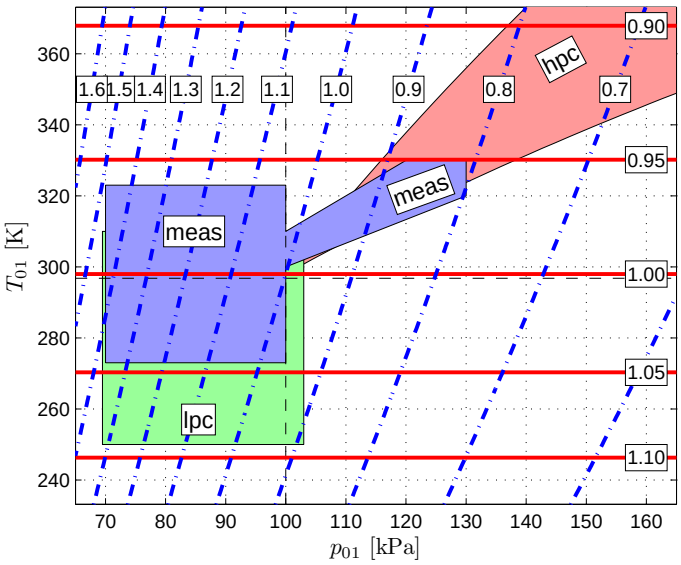

Figure 2: Isolines of compressor performance variable scaling values, as function of inlet conditions. Solid, horizontal, lines show $1/\sqrt{\theta}$ and dash dotted lines show $\sqrt{\theta}/\delta$. The standard reference states $p_{std} = 100$ kPa and $T_{std} = 298$ K are also marked as dashed lines. Corrected and actual quantities are equal only at the intersection of these lines. Inlet conditions associated with a significant coverage of single stage automotive compressors is marked with "lpc", and high pressure stage compressor operation (for a two stage system) is marked "hpc". The region marked with "meas" is the grid for measurements in Section 4.

compressor, and indicates the boundary of stable compressor operation. Turbo shaft speeds are measured up to the maximum allowable, $N_{tc,max}$. Raising the speed further, known as over speeding [8], can destroy the turbo.

The adiabatic efficiency, η_c, is also presented for each point, describing how efficiently the compression process is, compared to an adiabatic. Contours of constant η_c are superimposed on the speed lines in Figure 1.

The connection between inlet conditions and correction quantities is shown in Figure 2, where solid lines show constant mass flow scaling factor $\sqrt{\theta}/\delta$, and dash dotted lines show constant shaft speed scaling factor $1/\sqrt{\theta}$, as function of inlet conditions.

Compressor speed line modeling

An Ellipse compressor model [9, 10] will be used in the following sections. The equation to model a single speed line is

$$\Pi_c = \left(1 - \left(\frac{\dot{m}_{c,corr} - c_4}{c_3 - c_4}\right)^{c_1}\right)^{1/c_2} c_5 \tag{5a}$$

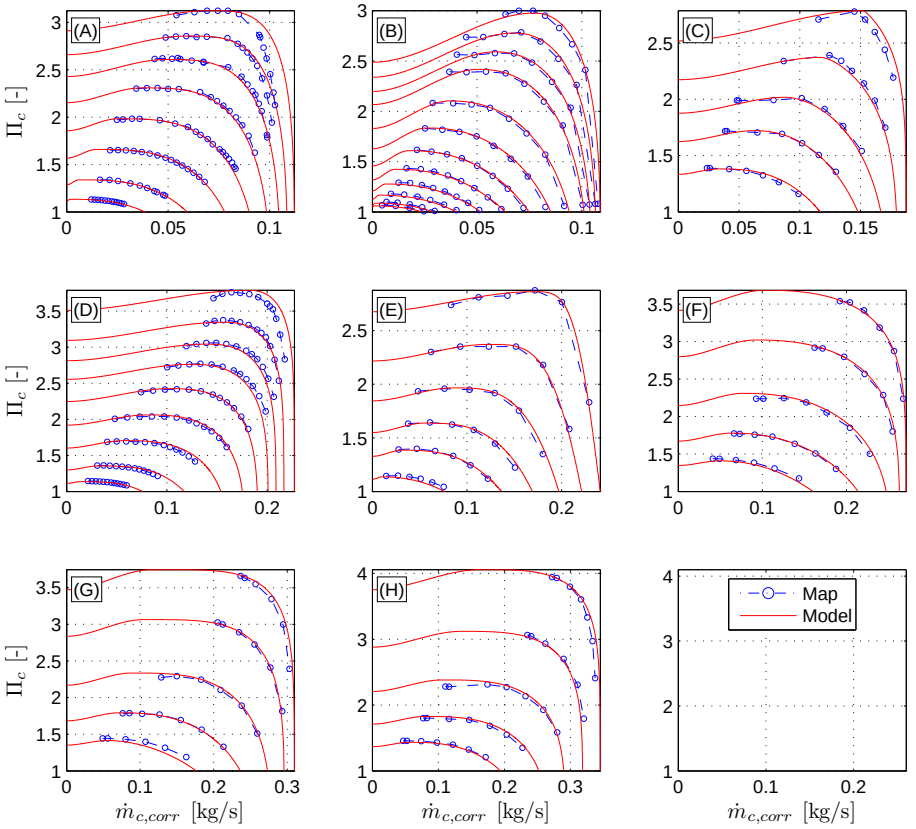

Figure 3: Eight compressor maps shown with circles connected by dash dotted lines, and the fit of the Ellipse model in (5a-f).

where the $c_i,\ i \in [1,5]$ are the speed line model parameters. A complete compressor model results, if c_i are instead basis functions according to

$$c_1 = c_{1,0} + c_{1,1} N_{tc,corr} \tag{5b}$$
$$c_2 = c_{2,0} + c_{2,1} N_{tc,corr}^{c_{2,2}} \tag{5c}$$
$$c_3 = c_{3,0} + c_{3,1} N_{tc,corr} \tag{5d}$$
$$c_4 = 0 + c_{4,1} N_{tc,corr}^{c_{4,2}} \tag{5e}$$
$$c_5 = 1 + c_{5,1} N_{tc,corr}^{c_{5,2}} \tag{5f}$$

where $c_{i,j}$ are the 11 model parameters for a compressor model (5a-f). Eight compressor maps (A-H) will be used in the analysis, in the following sections. In Figure 3 the compressor model fit to the eight maps is shown to be good. The maximum mass flow for the maps, range from $\approx$0.1 kg/s (A), up to $\approx$0.3 kg/s (H).

2 Inlet conditions for automotive compressors

The compressor inlet gas state depends on both changes in ambient conditions, as well as on the engine subsystems affecting the gas before the compressor inlet.

2.1 Variations in ambient conditions

In order to find what values of (p_{amb}, T_{amb}) that are common for automotive turbochargers one needs to know how and where the system is used.

Ambient pressure variations

Roads are found at altitudes from below -400 m to more than 5000 m. Most vehicles are found at less extreme altitudes, and for a significant coverage of automotive engine applications

$$h_{sig} \in [-100, 3000] \text{ m} \tag{6}$$

is assumed to be sufficient. This smaller interval also helps reducing the cost of an experimental campaign that covers the interval. The close connection between altitude and pressure can be modeled [11]

$$p_{amb}(h) = p_{\{h=0\}}(T_b/(T_b - L_b(h - h_b)))^{\left(\frac{g_0 M}{R L_b}\right)} \tag{7}$$

with $p_{\{h=0\}} = 101.3$ kPa, $T_b = 288.15$ K, $R = 8.31$ J/(mol K), $h =$ altitude m, $h_b = 0$ m, $g_0 = 9.807$ m/s^2, $L_b = -0.0065$ K/m and $M = 0.02896$ J/(kg K). The ambient pressure variations due to altitude can be found using (7), and for the interval (6) this is

$$p_{amb,sig} \in [70, 103] \text{ kPa} \tag{8}$$

The result of using (7) for the interval in (6) is further presented in Figure 3.4(b). It is seen that $p_{amb}(h)$ is approximately a straight line. Normal ambient pressure variations due to weather, are smaller than those due to altitude, see Figure 3.4(a), and are for the following investigations considered to be included in the interval (8).

Ambient temperature variations

Extremes in measured ambient temperature shows values of $T_{amb} \in [184, 331]$ K. Significant coverage of engine operations is reached for a narrower temperature interval

$$T_{amb,sig} \in [250, 310] \text{ K} \tag{9}$$

Ambient temperature can be modeled [12]

$$T_{amb} = T_{ref,sea} + L_b h \tag{10}$$

where $T_{ref,sea} = 293.15$ K. The result of using (10) for the intervall given in (6) is presented in Figure 3.4(b), and is a straight line. Figure 3.4(a) further presents an example of a temperature trace for one year, of Malmen meteorological station.

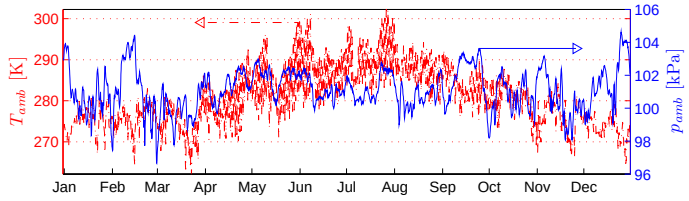

(a) Measurements of ambient conditions during one year.

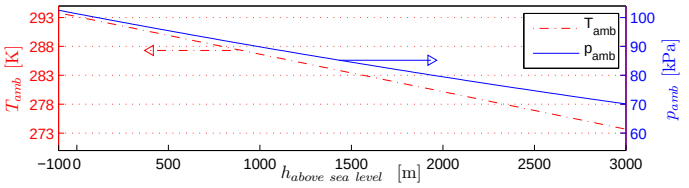

(b) $T_{amb}(h)$ and $p_{amb}(h)$ according to (7) and (10).

Figure 4: Summary of the variations in ambient pressures and temperature due to altitude and seasonal changes. Upper: Measurements of ambient conditions of Malmen meteorological station. Both T_{amb} and p_{amb} vary approximately 10% over the year. Lower: Temperature and pressure vs. altitude using (7) and (10).

Two stage system

For a two stage system the quotient between the pressure ratio of the high pressure stage, Π_{hpc}, and the pressure ratio of the low pressure stage, Π_{lpc}, is defined

$$\Gamma = \Pi_{\mathrm{hpc}}/\Pi_{\mathrm{lpc}} \tag{11}$$

and the total compression system pressure ratio is given by the ratio of high pressure stage outlet pressure p_{hpc} to first stage inlet pressure p_{01}

$$\Pi_{tot} = \Pi_{lpc} \cdot \Pi_{hpc} = \mathrm{p_{hpc}}/\mathrm{p_{01}} \tag{12}$$

where p_{01} is the total pressure at the first stage inlet. The Γ-value describes how much of the total pressure increase that is done by the second stage compared to the first. To avoid a pressure loss over either of the compressor stages, the following must hold

$$\frac{1}{\Pi_{tot}} < \Gamma < \Pi_{tot} \tag{13}$$

Compressor outlet temperature, T_{01}, can be modeled

$$T_{02} = \left(\frac{\Pi_c^{\frac{\gamma-1}{\gamma}} - 1}{\eta_c} + 1 \right) T_{01} \tag{14}$$

with $\Pi_c = p_{02}/p_{01}$. Temperature and pressure after the first compressor stage, are the inlet conditions of the second stage. Figure 2 shows inlet conditions for the second stage compressor marked with hpc, calculated as first stage outlet states using (14) with $\eta_c \in [40, 90]$ %, $p_{01} = p_{std}$ and $T_{01} = T_{std}$.

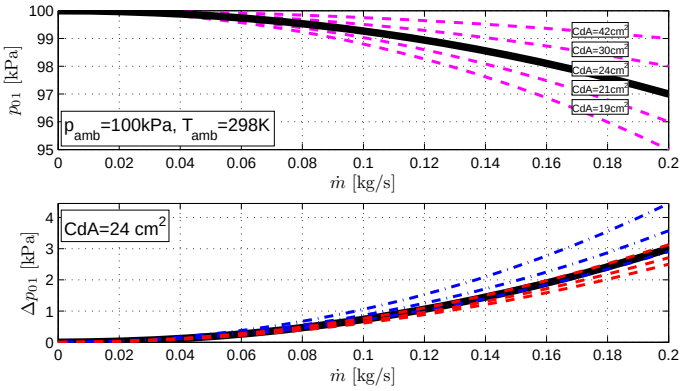

Figure 5: Pressure drop from ambient to compressor inlet, $\Delta p_{af} = p_{amb} - p_{01}$. Upper plot: p_{01} as function of mass flow for different C_dA-values and constant (p_{amb}, T_{amb}). Lower plot: dash dotted line shows Δp_{af} as a function of different $p_{amb} \in [70, 103]$ kPa (with $T_{amb} = 298$ K), and dashed as a function $T_{amb} \in [250, 310]$K (with $p_{amb} = 100$ kPa). The thick solid line in both plots is for $C_dA = 24\,cm^2$, $p_{amb} = 100$ kPa and $T_{amb} = 298$ K as a reference.

2.2 Air filter and intercooler

Apart from changes in p_{amb} and T_{amb}, the engine installation also affects the gas on its way to the compressor inlet. p_{01} for automotive applications, is expected to be slightly lower than p_{amb}, because the air filter and pipes between compressor inlet and ambient restrict the air flow, resulting in a pressure loss $\Delta p_{af} = p_{amb} - p_{01}$. A general restriction for a compressible flow [7] can be used to model an air filter restriction as

$$\dot{m} = \frac{C_d A p_{amb}}{\sqrt{RT_{amb}}} \left(\frac{p_{01}}{p_{amb}}\right)^{\frac{1}{\gamma}} \sqrt{\frac{2\gamma}{\gamma - 1}\left(1 - \left(\frac{p_{01}}{p_{amb}}\right)^{\frac{\gamma-1}{\gamma}}\right)} \tag{15}$$

where C_dA is normally lumped together and referred to as effective flow area, and it is important to note that the resulting pressure drop depends on the ambient gas state. The pressure drop, for a system having $\Delta p_{af} = 3$ kPa at $T_{amb} = T_{std}$, $p_{amb} = p_{std}$, increases 50 % at $p_{amb} = 70$ kPa, due to the decreased ambient gas density. The largest increase in Δp_{af} from varying T_{amb} according to (9), is 7 %.

The upper plot of Figure 5 shows the result of (15) for different values of C_dA as a function of $\dot{m}$, with $p_{amb} = 100$ kPa and $T_{amb} = 298$ K. Values of Δp_{af} can be found in the literature [13, 14, 15], and are usually in the range of $\Delta p_{af} \in [3, 8]$ kPa.

Also the intercooler and pipes after the compressor are important when establishing the map operating point. The temperature of the gas after the compressor depends on the operating point, according to (14). Values of pressure drops caused by the intercooler can be found in the literature [13, 14], and are usually in the range of $\Delta p_{ic} \in [5, 15]$ kPa.

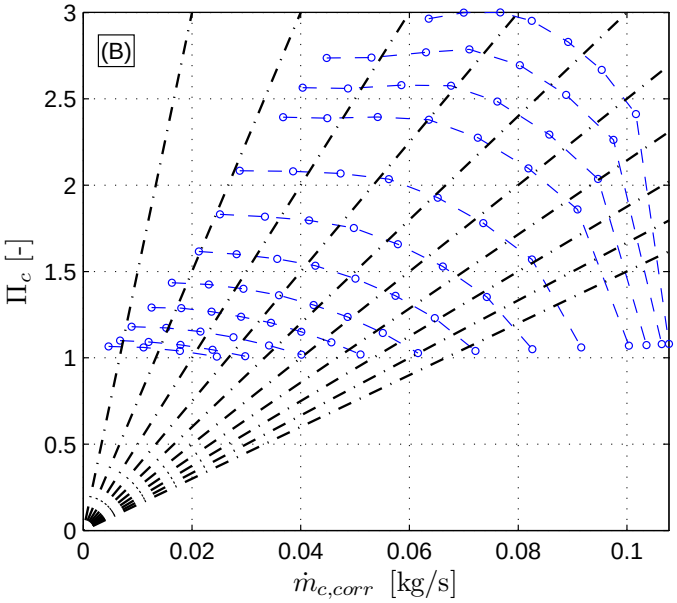

Figure 6: The dash dotted lines represent the translation asymptote in a map, due to a change in p_{01}, and are superimposed on Compressor map (B).

3 Automotive examples

The corrections (3) and (4) and a map have direct automotive control implications, and this section exemplifies it through two applications. Opportunities for a novel way to control surge is presented first. Secondly, the investigations from Section 2, and a map, are used to calculate an altitude dependent engine torque line. Three different limits are taken into account: Compressor surge (CS), turbo over speed (TOS), and the extreme point where the maximum allowable pressure ratio of the map is utilized (Π_{max}). Π_{max} is always at the TOS-limit and at max Π_c of the map. The second example is used again in Section 6, with modified corrections (3) and (4).

3.1 Opportunities for novel surge control

The change in operating point coming from a decrease in p_{01} is given by (2) and (3), and the dash dotted lines in Figure 6 show the associated translation in the map. It is seen that the lines have a large positive slope, and all go through $(\dot{m}_{c,corr}, \Pi_c) = (0, 0)$ for $p_{01} = \infty$. The lines also reveal that decreasing p_{01} can give a novel way to increase the margin to the surge line. If a new operating point, after a decrease in p_{01}, is further away from the surge line depends on the surge line slope, for the studied Π_c.

The question is whether there exist map points, where a decrease in p_{01} increases the surge margin. The method to answer this question is as follows. Find the line from Figure 6, that has the same slope as the surge line, for the studied Π_c-range. Superimpose this line on the compressor map, and any point

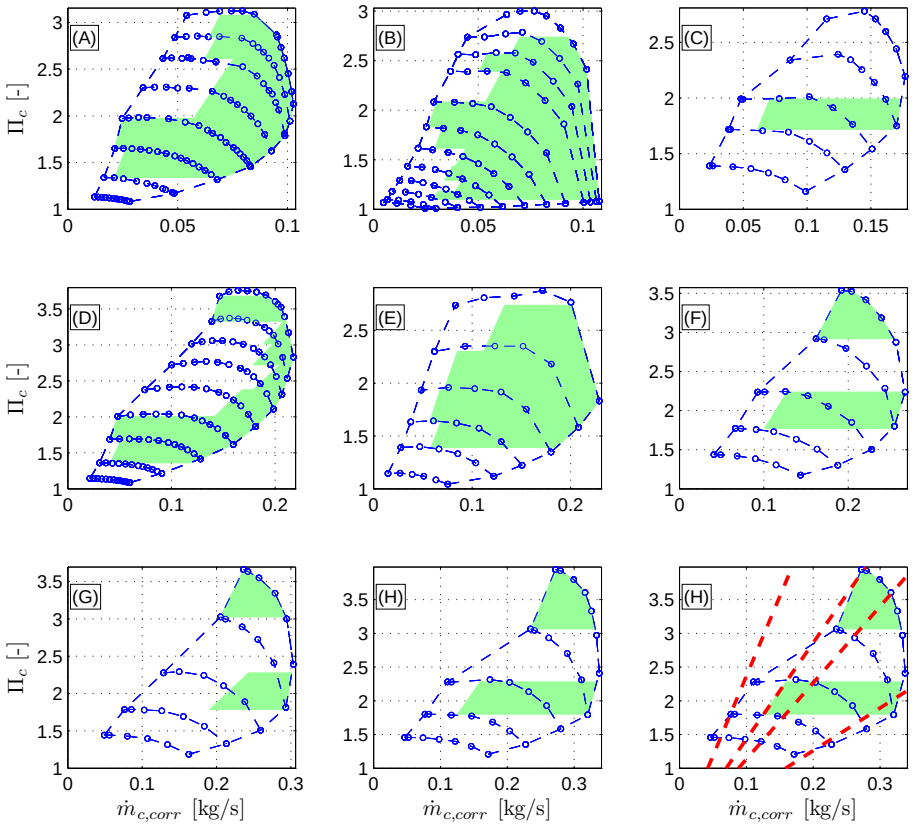

Figure 7: Map areas were the points are such that a decrease in p_{01} increases the surge margin. The lower right plot shows the lines with the same slope, as the straight lines making up the surge line, for map (H), but originating in (0,0). Corresponding lines are used to assess the marked areas of all maps (A-H).

in the map, that is right of this dash dotted line, for the studied Π_c-range, will see an increase in surge margin for a decrease in p_{01}. Figure 7 presents areas, for maps A-H, were the surge margin is increased for a decrease in p_{01}. It can be seen that such areas exist, also close to the surge line. The method to use the dash dotted lines of Figure 6 and a map is general, and can be used for any map.

3.2 Max torque line vs. altitude

The compressor map can be used to calculate an altitude dependent maximum engine torque line, using a volumetric efficiency engine model. This section presents such calculations with the correction quantities given by (3) and (4) for the maps (A-H). This issue will be returned to in Section 6, where modified corrections are used. The allowable map region, giving the potential engine torque, is limited by CS, TOS and Π_{max}. p_{amb} and T_{amb} are connected to altitude using (7) and (10).

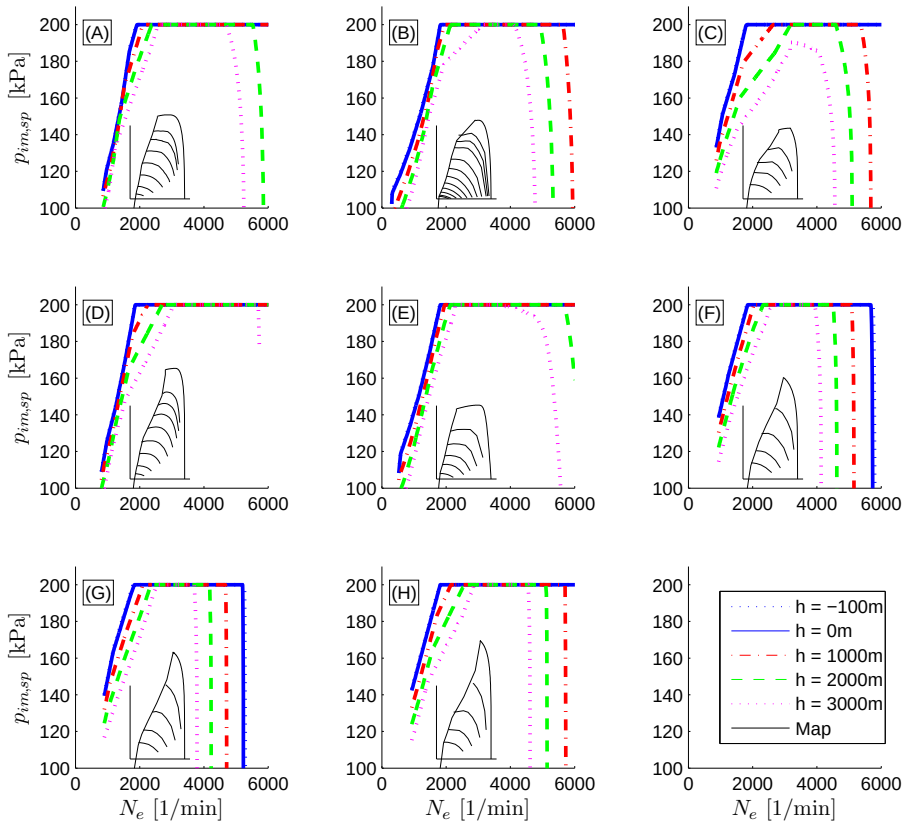

Figure 8: Lines showing for which N_e a $p_{im,sp} = 200$ kPa is achievable as a function of altitude $h \in [-100, 0, 1000, 2000, 3000]$ m. Each subplot contains a picture of the corresponding map, to show the close coupling of the allowable map region and the achievable $p_{im,sp}$.

The outer contour of the stable compressor operating region, gives the maximum allowable Π_c, for a mass flow. The outer contour consists of the maximum allowable corrected shaft speed, $N_{tc,corr,max}$ and the surge line. Maximum allowable corrected shaft speed is given by $N_{tc,corr,max} = {}^{N_{tc,max}}/\sqrt{{}^{T_{01}}/_{T_{std}}}$, and depends on T_{01}. This speed line is modeled using (5a). The surge line is given by each map.

Maximum engine torque is assumed achievable, if an intake manifold pressure set point of $p_{im,sp} = 200$ kPa, is achievable. Different engine models, based on volumetric efficiency, are assumed for each map (A-H). The volumetric efficiency is assumed to give an mass flow, $\dot{m}_{2k}$, at an engine speed of $N_e = 2000$ 1/min and at $p_{im,sp} = 200$ kPa. $\dot{m}_{2k}$ is taken from each map (A-H), as 110 % of the surge mass flow at $\Pi_c = 2, \theta = 1, \delta = 1$. The volumetric efficiency is further assumed to give $2.5 \cdot \dot{m}_{2k}$ at $N_e = 5000$ 1/min and $p_{im,sp} = 200$ kPa. This N_e-range corresponds to torque/speed characteristics commonly found in modern TC engines. Π_c is given by air filter and intercooler models according to Section 2.2.

Table 1: Altitude where engine torque is reduced, due to the limits (CS, TOS, Π_{max}) discussed in Section 3.2, for maps (A-H).

Map limits		(A)	(B)	(C)	(D)	(E)	(F)	(G)	(H)
CS	m	480	1240	230	460	1310	820	610	620
TOS	m	2660	1900	1490	4040	2650	1150	390	2200
Π_{max}	m	3840	3290	2550	5510	3030	4920	5210	5870

Figure 8 shows the resulting engine torque lines, along with a small map in each subplot, to emphasize the coupling of the allowable map region and the achievable $p_{im,sp}$. Table 1 presents the altitudes where engine torque has to be reduced, due to the CS, TOS, or Π_{max}-limit. CS gives the altitude where $p_{im,sp}$ no longer can be reached for $N_e = 2000$ 1/min, TOS the corresponding value for $N_e = 5000$ 1/min and Π_{max} finally gives the limit where $p_{im,sp}$ has to be reduced independent of $N_e \in [2000, 5000]$ 1/min. CS restricts engine torque before $h = 3000$ m, for all maps. TOS restricts all but map (D). Map (C) is restricted by the Π_{max}-limit before $h = 3000$ m. A narrow map width means difficulties with a wide mass flow range, e.g. map (G). The maps with best estimated low engine speed torque, have a surge line with steep positive slope, e.g. map (B) or (E). To be least limited by Π_{max}, a map needs a large maximum Π_c at $N_{tc,max}$, e.g. map (F).

It is important to note that these calculations are given by, not only the compressor map, but also by the corrections (3) and (4).

4 Experimental investigation of correction quantities

This section presents speed lines, measured at different compressor inlet conditions. An engine test stand measurement is first presented, focusing on the low pressure stage inlet conditions from Section 2. A presentation of measurements, from an independent gas stand, focusing on high pressure stage inlet conditions, then follows.

4.1 Engine test stand measurements

The test setup consists of a 2L spark ignited direct injected engine with a two stage turbo system installed in an engine test cell. A schematic picture of the laboratory and measurement setup, used to vary compressor inlet conditions, is presented in Figure 9.

Low inlet temperature measurements are achieved using cold outside air. High inlet temperatures are created using electrical heating. Compressor inlet pressures are reduced using an extra throttle upstream the compressor inlet. An air filter follows the extra throttle. A straight pipe, approximately 80 cm in length, then leads up to the first stage compressor inlet. The instrumentation for the first stage inlet conditions is fitted to the straight pipe, to minimize influence from uneven distributed flow. Multiple sensors $(p, T, \dot{m})$ were fitted, to enable diagnose of the sensors. Pressure and temperature after the first compressor

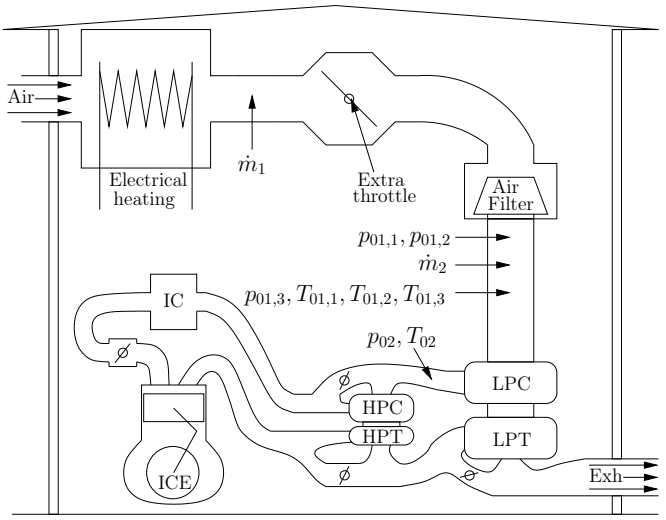

Figure 9: Schematic picture of the laboratory and engine test stand setup. Ambient air comes in from top left and can be electrically heated. The extra throttle is used to decrease p_{01}. An air filter is followed by three pressure ($p_{01,i}$) and temperature sensors ($T_{01,i}$), and a mass flow sensor ($\dot{m}_2$) before the compressor inlet. An extra mass flow sensor is installed before the extra throttle for diagnosis purposes. p_{02} and T_{02} are measured at the lpc outlet. The air flow runs through the engine, catalyst and the exhaust is expelled to the outside.

stages are measured using a single pair of sensors, since the sensor placement is limited due to packaging constraints. Further, the degrees of freedom are reduced when measuring compressor speed lines in an engine test stand [16].

It is not possible to increase p_{01} during the engine test stand measurements. The pipes and air filter cause a pressure drop, see Section 2.2. This means that it is difficult to reach $p_{01} = 100$ kPa for large mass flows, and the pressure drop is up to 5 kPa.

Low pressure compressor stage - lpc

The speed lines are measured for different combinations of $T_{01} \in [273, 323]$ K and $p_{01} \in [70, 100]$ kPa. All speed lines are measured with constant $N_{tc,corr}$, calculated using (4). The measured grid is schematically shown in Figure 2 and the resulting speed lines are shown in Figure 10 with corresponding gas stand speed lines as reference. The compressor performance differs between the engine test stand measurements and in the reference gas stand map. Installation dependent compressor performance is frequently encountered, and is also reported in [8, 17, 18]. The data for the two speed lines presented here, is summarized in Table 2. It can be seen that the mean absolute relative error for the shaft speeds presented was 0.2%, or lower. These small deviations are adjusted for using the techniques, based on dimensionless numbers, developed in [16] (i.e $\Delta\Phi = 0, \Delta\Psi = 0$ for small $\Delta N_{tc} = N_{tc,meas} - N_{tc,sp}$).

The lower speed line of Figure 10, is limited to measurements with compres-

Table 2: The corrected shaft speeds measured in the engine test stand $N_{tc,corr,sp}$, number of points measured #, and measured grid of inlet conditions. The two last columns show mean absolute relative error $|(\mathrm{N_{tc,corr,sp}}/\mathrm{N_{tc,corr,meas}}) - 1|$, and standard deviation.

$N_{tc,corr,sp}$	#	p_{01} [kPa]	δ [-]	T_{01} [K]	θ [-]	mean	std
103869	275	70–100	0.7–1	273–323	0.92–1.08	0.20%	0.26%
77064	179	80–100	0.8–1	273–323	0.92–1.08	0.18%	0.26%

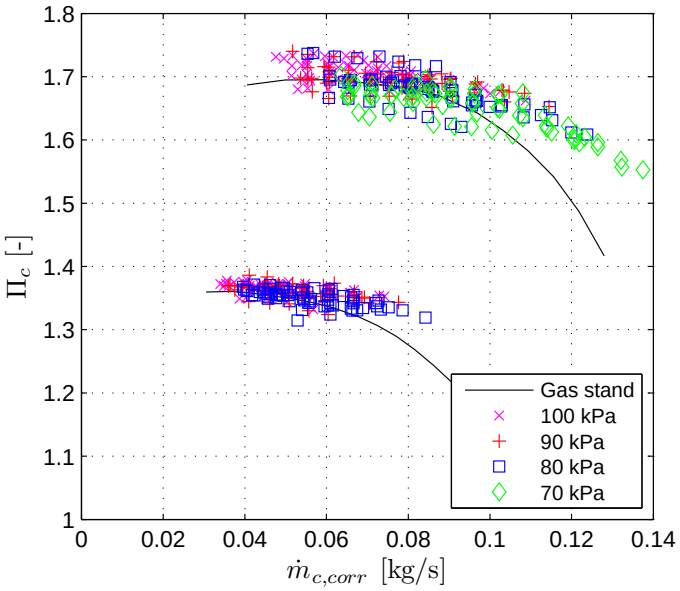

Figure 10: Measured map points from the engine test stand, at different inlet conditions. Solid line are gas stand speed lines as reference. Points with equal $p_{01} = \{70, 80, 90, 100\}$ kPa are marked by equal symbol. The upper speed line will be referred to as the large shaft speed, and the lower as the small shaft speed.

sor inlet pressure $p_{01} > 80$ kPa, since otherwise $p_{01} \cdot \Pi_c < p_{amb}$, which causes the soft pipes of the engine intake system to collapse as discussed in [16]. Not all T_{01} of the $T_{01,grid}$ of Table 2 are measured for both shaft speeds presented here, a total of nine different T_{01} are measured within the $T_{01,grid}$.

Speed line dependence on p_{01} and T_{01}

The result of the analysis of the measurements show that, if the measured speed lines are given different symbols for different p_{01} as in Figure 10, points with lowest p_{01} are generally below these of the second smallest p_{01}, with the trend also visible for the larger p_{01}-points. The speed line model (5a) is therefore used to investigate and visualize a potential p_{01}-dependence. The parameters $c_i, i \in [1, 5]$ of (5a) are fitted to measurements with equal p_{01}, but different T_{01}, to see if there are any trends in the modeled speed lines. The resulting

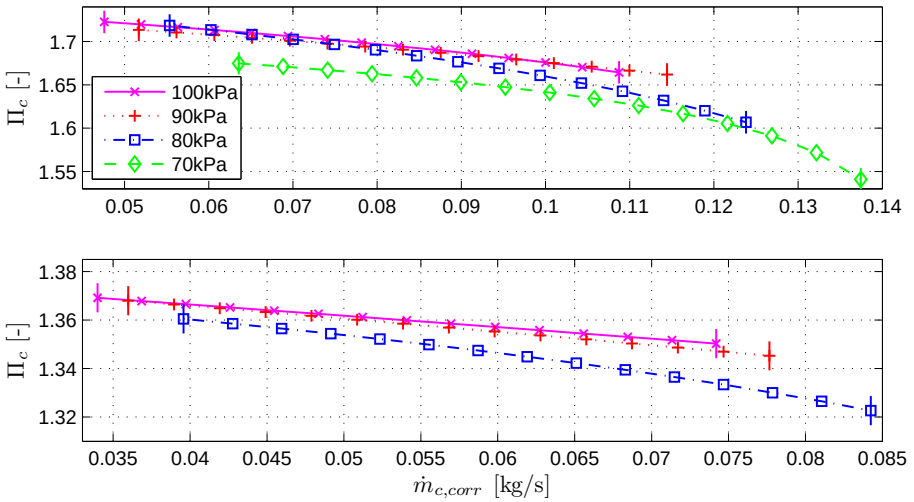

Figure 11: Speed line models (5a) fitted to measured data with constant $(N_{tc,corr}, p_{01})$, for the large and small shaft speed presented in Figure 10. The extra vertical lines on each modeled speed line shows the range of data points for that particular p_{01}. There is a small discrepancy between Π_c for different p_{01} with the general trend showing larger Π_c for larger p_{01}.

speed lines are presented in Figure 11. The data shows a clear trend; for the smallest corrected shaft speed the $p_{01} = 100$ kPa-model has the largest Π_c, and the $p_{01} = 80$ kPa-model has the lowest Π_c. The larger $N_{tc,corr}$-lines display the same trend, largest Π_c is found for largest p_{01} given a $\dot{m}_{c,corr}$.

Applying the same methodology to points with equal T_{01}, reveals no trends. For the small corrected shaft speed the lowest temperature line is at the bottom, but then the second highest temperature line follows. The same mixed order is also found for the large corrected speed.

Points with $(\dot{m}_{c,corr}, N_{tc,corr}) = const$

Π_c for points with equal $(\dot{m}_{c,corr}, N_{tc,corr})$, but with different (p_{01}, T_{01})-pairs, are compared to further investigate possible trends in Π_c. Automotive compressors have small speed line slopes over a wide range of mass flows. The data is therefore divided into groups at multiples of 5 g/s, where map points with $\Delta\dot{m}_{c,corr} = \pm 1.5$ g/s around the desired multiple of 5 g/s, are accepted, i.e. for the 70 g/s case, points with $\dot{m}_{c,corr} \in [68.5, 71.5]$ g/s. A model is estimated, for each $\dot{m}_{c,corr}$-group using

$$a_0 = a_1 p_{01} + a_2 T_{01} + a_3 \Pi_c \tag{16}$$

to make any trend in Π_c, for changing p_{01} and/or T_{01}, more prominent. The intersection between the model (16) and the axes of the plot is given in Figure 12. The equations for the planes were bias adjusted for better visibility, which does not alter the conclusions, since it is the slope that is of interest.

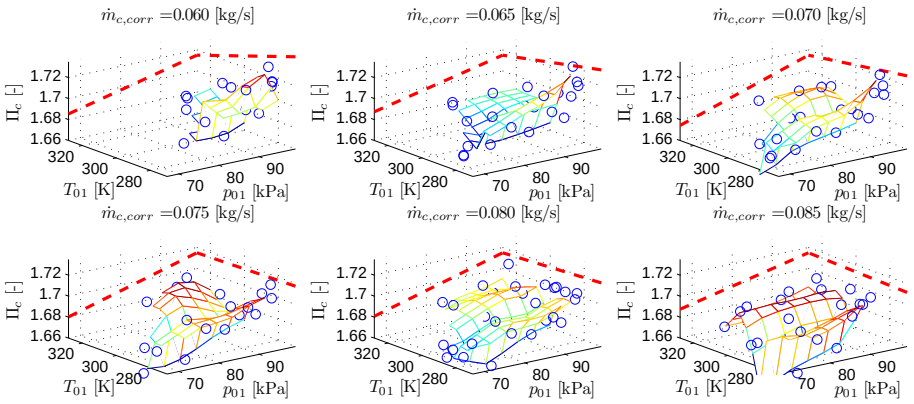

(a) Large shaft speed

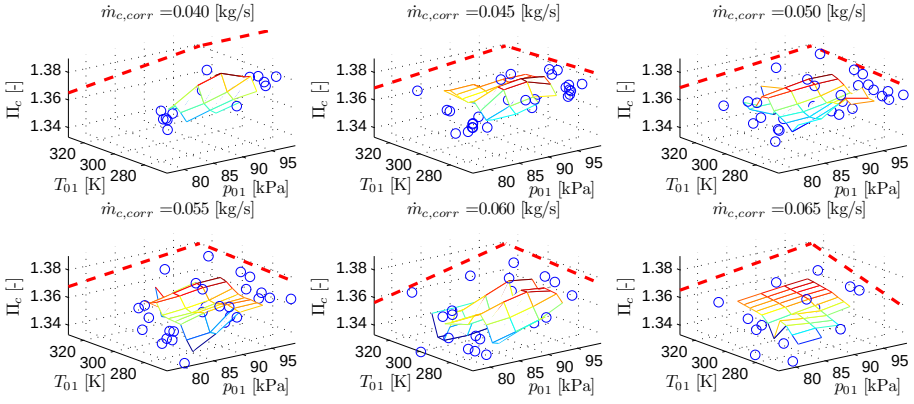

(b) Small shaft speed

Figure 12: Variations in measured Π_c for different $(\dot{m}_{c,corr}, p_{01}, T_{01})$ for two shaft speeds. A trend with decreasing Π_c for decreasing p_{01} is seen. The dashed line gives a bias adjusted LSQ-fitted plane (16), and its intersection with the axes, to better visualize trends.

The result from the investigation is that for both corrected shaft speeds measured, a decreasing trend in Π_c for decreasing p_{01} is found, supporting the results from previous section. No clear trend in T_{01} is found. A large positive slope of the model (16) with T_{01} is found for the smallest corrected mass flow point presented for the small corrected shaft speed. The opposite case if found for the same corrected shaft speed, for the largest corrected mass flow presented.

4.2 Gas stand data

The gas stand data is measured independently and according to industrial practice (see e.g. [2, 3, 4]), and more details are found in [19]. The same two stage system as in the engine test stand, but another individual, is used. Two different data sets are measured. The first consists of individual maps of the two stage system compressors, measured with inlet conditions $\theta \approx 1, \delta \approx 1$. The

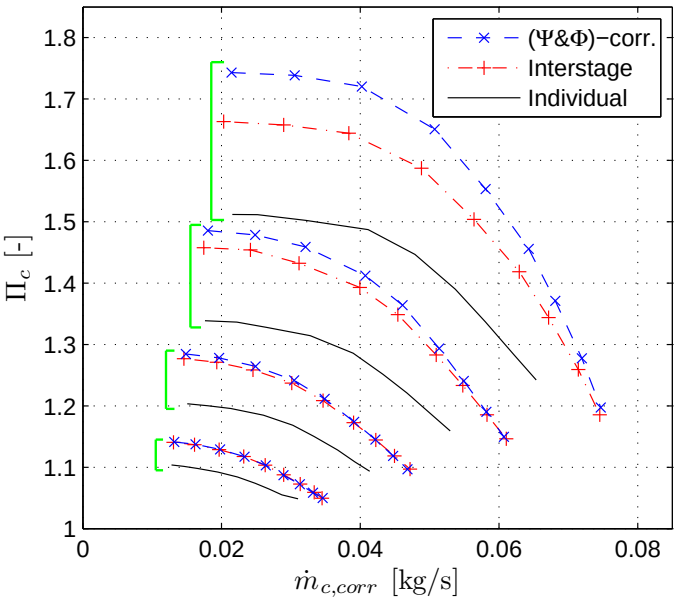

Figure 13: Dash dotted lines show underlying interstage measurement, which is measured at constant N_{tc}. Dashed line: adjusted interstage measurement using the techniques in [16], to give the corresponding $N_{tc,corr}$-line of the dash dotted line. The solid line presents the individual gas stand map as reference. The square brackets indicate which speed lines that should be compared.

two turbos are then mounted together for the second data set, and second stage speed lines are measured for small Γ, see (11). This map has inlet conditions $\theta > 1, \delta > 1$, see Section 2.1, and will be referred to as the interstage map.

The individual high pressure stage map, referred to as the individual map, will be compared to the interstage high pressure map in this section, since they are maps of the same turbo, but with different inlet conditions.

High pressure compressor stage - hpc

The interstage temperature is measured in close proximity to the second stage impeller, which, for mass flows close to surge, can show an increase in temperature [20]. This is indeed seen for the smallest mass flow point of each speed line, which has a temperature increase of $15 - 20$ K, compared to the second smallest mass flow point. The temperature for the smallest mass flow point is therefore adjusted, and set equal to the temperature of the second smallest mass flow point on that speed line. The interstage data is further measured at constant N_{hpc} and not constant $N_{hpc,corr}$. The (Ψ&Φ)-approach in [16] is therefore used to adjust the measurements. The result is shown in Figure 13, where the solid lines show the individual gas stand map as a reference. The dashed dotted line represents the performance map calculated using the modeled inlet temperature, and measured inlet pressure, but with $N_{hpc} = const.$ The dashed line represents the $N_{hpc,corr} = const$ speed lines calculated using

Table 3: Measured shaft speeds, number of points #, and inlet conditions for the interstage hpc-map, presented with dash dotted lines in Figure 13.

N_{tc}	#	p_{01} [kPa]	δ [-]	T_{01} [K]	θ [-]
144597	9	118–128	1.18–1.28	318–331	1.09–1.13
118795	9	107–113	1.07–1.13	308–317	1.05–1.08
92959	9	102–106	1.02–1.06	303–310	1.04–1.06
67081	9	100–102	1.00–1.02	302–308	1.03–1.05

the (Ψ&Φ)-approach.

The inlet conditions for the interstage map are presented in Table 3, and represent from left to right, low to high shaft speed. A large discrepancy exists between the individual and the interstage hpc-map. Since $T_{01} > T_{std}$, i.e. $\theta > 1$, of the hpc inlet, the corresponding $N_{tc,corr}$ of the interstage map, is smaller than for the individual hpc-map, given the same N_{tc}-line. Even so, all interstage speed lines have larger Π_c given a $\dot{m}_{c,corr}$ than the corresponding lines measured in the individual hpc-map.

5 Modifying the corrections

The correction factors are applied to scale the compressor performance variables, to cover also different inlet conditions, than those used during the performance measurement. Π_c of two points, with the same corrected mass flow (3) and corrected shaft speed (4), measured at different inlet conditions should be equal. This is not the case for the measurements presented in the previous sections.

This section investigates if the corrections, (3) and (4), can be modified, to better fit the measured data. The corrections are modified separately. This reduces the analysis complexity, and is deemed as an adequate approach to find trends in the data without risking over fitted parameters. Further, the structure of the corrections is kept, and the following shaft speed correction is proposed

$$N_{tc,corr,K} = \frac{N_{meas}}{\theta^m}\delta^n \tag{17}$$

where, compared to (4), also δ is included, and the parameters (m, n) are allowed to vary, and $K \in \{\text{I,II,III,IV}\}$ represents the different corrections that are tested, and are further presented in Section 5.2. A case with $m = 0.5, n = 0$ corresponds to the nominal correction (4). For the mass flow correction the following modification is proposed

$$\dot{m}_{c,corr,J} = \dot{m}_{c,meas}\frac{\theta^r}{\delta^s} \tag{18}$$

where a case with $r = 0.5, s = 1$ corresponds to the nominal correction (3). The $J \in \{\text{I,II,III,IV}\}$ are further presented in Section 5.2. Assuming that most maps are measured with $\theta \approx 1, \delta \approx 1$, this correction structures also have the advantage that no change is needed to most maps. To avoid unreasonable correction quantities, (m, n) and (r, s) are allowed to vary in the range $[-2, 2]$.

5.1 Connecting a change $dN_{tc,corr}$ to a change $d\Pi_c$

In order to see how a modification to the shaft speed correction, changes a map point, the modification needs to be connected to either, or both, of the other variables of the map: $\dot{m}_{c,corr}$ and Π_c. This section connects $dN_{tc,corr}$ to $d\Pi_c$, and develops a tool to adjust measured Π_c, due to a modified shaft speed correction.

For any function $\tilde{f} = \tilde{f}(\dot{m}_{c,corr}, N_{tc,corr}, \Pi_c) = 0$, e.g. using (5a-f)

$$\tilde{f} = \Pi_c - \left(1 - \left(\frac{\dot{m}_{c,corr} - c_4}{c_3 - c_4}\right)^{c_1}\right)^{1/c_2} c_5 = 0 \tag{19}$$

where the c_i are functions of $N_{tc,corr}$ according to (5b-f), the implicit function theorem can be used to calculate the quantity $dN_{tc,corr}/d\Pi_c$, according to

$$d\tilde{f} = \frac{\partial \tilde{f}}{\partial \Pi_c} d\Pi_c + \frac{\partial \tilde{f}}{\partial \dot{m}_{c,corr}} d\dot{m}_{c,corr} + \frac{\partial \tilde{f}}{\partial N_{tc,corr}} dN_{tc,corr} = 0 \tag{20}$$

The variation of interest is how a speed line changes, for a given $\dot{m}_{c,corr}$. This variation can be deduced by setting $d\dot{m}_{c,corr} = 0$ in (20), giving the sensitivity

$$\left.\frac{dN_{tc,corr}}{d\Pi_c}\right|_{\dot{m}_{c,corr}} = -\frac{\frac{\partial \tilde{f}}{\partial \Pi_c}}{\frac{\partial \tilde{f}}{\partial N_{tc,corr}}} \tag{21}$$

An analytical derivation of (21), for the model (5a-f), is found in the Appendix. A change $dN_{tc,corr}$ can thus be connected to a change $d\Pi_c$ for constant $\dot{m}_{c,corr}$. This means that a point measured at erroneous $N_{tc,corr}$ can be adjusted vertically in the map, if the partial derivatives can be calculated. The quantity, given by (21), gives the corrected shaft speed change associated with a unit increase in Π_c, for a point in the map.

Also $dN_{corr}/d\dot{m}_{c,corr}$ can be calculated. This is however neglected, due to the high sensitivity caused by the small slopes of the speed lines, pointed out in [14, 16].

Modeling $dN_{tc,corr}/d\Pi_c$

The model (5a-f) is used to calculate (21) for the eight maps (A-H) presented in Figure 3. The calculations show that the largest values of (21) are found at the surge line of the lowest speed line for all maps, and decreasing for increasing $\dot{m}_{c,corr}$. The sensitivity (21) is also decreasing with increasing shaft speeds, and found to be approximately affine in corrected mass flow, given a $N_{tc,corr}$. Equation (21) is always positive, since speed lines never cross.

An affine model in $\dot{m}_{c,corr}$ according to

$$\frac{dN_{tc,corr}}{d\Pi} = d_1 \dot{m}_{c,corr} + d_0 \tag{22}$$

where (d_1, d_0) are model parameters, is proposed to model (21). Figure 14 presents four models (22) parametrized to the four corrected shaft speed of the individual hpc-map, and the model fit is good. The model (22) is used in the next sections to analyze modifications of the corrections according to (17) and (18).

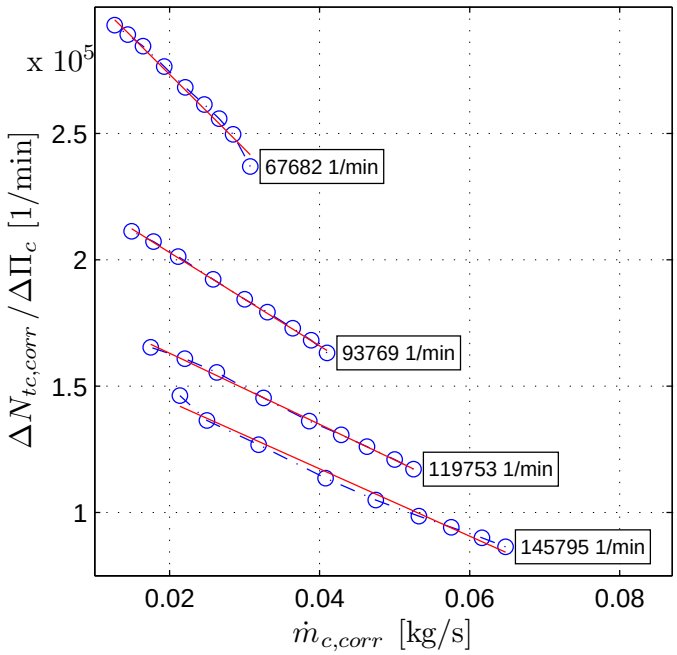

Figure 14: Modeled $dN_{tc,corr}/d\Pi_c|_{\dot{m}_{c,corr}}$ as a function of $\dot{m}_{c,corr}$ for the individual hpc map. An affine function in $\dot{m}_{c,corr}$ is also shown for each line to motivate the simple model used in the investigation of the correction quantities.

5.2 Low pressure stage data

The low pressure stage data is analyzed first, since this data is more comprehensive than the high pressure stage data. The high pressure stage data is then used to confirm the results from the low pressure stage measurement.

The objective with the investigation presented in this section, is to estimate a speed line with unknown shape and corrected shaft speed, modeled using (5a). Note that the engine test stand measured speed lines are not compared to the reference gas stand speed lines. The (d_1, d_0) from (22) are calculated using the reference gas stand speed lines, and are considered representative also for the engine test stand speed lines. The parameters (d_1, d_0) can be included in the estimation, but was neglected here, due to the increase the numbers of parameters to fit to the data.

Modifying the shaft speed correction

This section assumes that (3) is valid, and investigates if there are gains in modifying (4), according to (17). Four shaft speed corrections were tested, $K \in \{\text{I,II,III,IV}\}$. Correction I uses $m = 0.5, n = 0$, and corresponds to the nominal correction quantity (4). Correction II has $m \in [-2, 2], n = 0$, Correction III $m = 0.5, n \in [-2, 2]$, and Correction IV varies both parameters, $m \in [-2, 2], n \in [-2, 2]$. Given a desired corrected shaft speed $N_{tc,corr,sp}$, it is possible to correct

Table 4: Changes in fit of measured data to a speed line model (5a), for modified shaft speed corrections (17). It is seen that an enhancement of the fit is achieved if also δ is included in the correction. An even better fit is obtained if also the θ-exponent is allowed to change, the increased fit associated is though small. The most notable increase in fit comes from going from Correction II to Correction III, meaning that also δ is included in the calculation of $N_{tc,corr}$.

Corr.		m	n	$N_{tc,corr,sp}$	mean($\|e\|$)	std(e)	$\sum(\|e\|)$
103869	I	0.5	0	103867	0.0156	0.0206	4.30
	II	0.540	0	103870	0.0155	0.0203	4.27
	III	0.5	0.041	103862	0.0140	0.0190	3.85
	IV	0.562	0.045	103862	0.0140	0.0184	3.84
77064	I	0.5	0	76973	0.0078	0.0102	1.39
	II	0.460	0	77039	0.0074	0.0100	1.33
	III	0.5	0.053	77025	0.0066	0.0094	1.18
	IV	0.476	0.051	76995	0.0064	0.0093	1.14

the measured Π_{meas} using (22)

$$\Pi_{corr} = \Pi_{meas} + \frac{dN_{tc,corr}}{d_1 \dot{m}_{c,corr} + d_0} \tag{23}$$

where (d_1, d_0) are parametrized using a speed line model (5a), for the reference gas stand map data and

$$dN_{tc,corr} = N_{tc,corr,sp} - N_{tc,corr,K} \tag{24}$$

A non linear least squares estimation method is used to find $(m, n, N_{tc,corr,sp})$ and $c_i,\ i \in [1, 5]$ of (5a), minimizing

$$e = (\Pi_{mod} - \Pi_{corr}) \tag{25}$$

or more explicit

$$\left(1 - \left(\frac{\dot{m}_{c,corr} - c_4}{c_3 - c_4}\right)^{c_1}\right)^{\frac{1}{c_2}} c_5 = \Pi_{meas} + \frac{N_{tc,corr,sp} - \mathrm{N_{meas}}/(\mathrm{T_{01}}/\mathrm{T_{std}})^{\mathrm{m}} \left(\mathrm{p_{01}}/\mathrm{p_{std}}\right)^n}{d_1 \dot{m}_{c,corr,meas} + d_0} \tag{26}$$

The fitted parameters $(m, n, N_{tc,corr,sp})$ of (26), are given in Table 4, along with standard deviation and mean for the error e (25). A better fit to the speed line model (5a) is found, when the shaft speed correction also contained p_{01}. The most notable increase in fit come from going from Correction II to Correction III, meaning to allow $n \neq 0$ and thus also include δ in the shaft speed correction. The best fit values for n are small and positive, corresponding to a correction with decreasing corrected shaft speed with decreasing inlet pressure.

Modifying the mass flow correction

This section modifies the mass flow correction (3) according to (18). The objective is to improve the fit to a speed line model (5a), for the engine test stand

Table 5: Change in fit of measured data to an Ellipse speed line if the mass flow correction factor (3) is changed according to (18), with the error to be non linear least squares minimized given by (27).

Corr.		r	s	mean($\|e\|$)	std(e)	$\sum(\|e\|)$
103869	I	0.5	1	0.0131	0.0174	3.60
	II	0.393	1	0.0131	0.0174	3.60
	III	0.5	0.974	0.0131	0.0174	3.60
	IV	0.361	0.944	0.0131	0.0174	3.60
77064	I	0.5	1	0.0070	0.0093	1.25
	II	-0.753	1	0.0061	0.0088	1.10
	III	0.5	1.725	0.0066	0.0091	1.18
	IV	-0.711	1.327	0.0060	0.0088	1.07

measured speed lines. $N_{tc,corr}$ is assumed to be constant, see Table 2. Four mass flow corrections are tested, $J \in \{\text{I,II,III,IV}\}$. Correction I has $r = 0.5, s = 1$, which is the standard correction (3), Correction II: $r \in [-2, 2], s = 1$, Correction III: $r = 0.5, s \in [-2, 2]$, and Correction IV varies both parameters $r \in [-2, 2], s \in [-2, 2]$.

A minimization of $e = \Pi_{mod} - \Pi_{meas}$ with Π_{mod} given by (5a) using the different versions of (18) is first investigated. The estimation problem is formulated; find the parameters of the speed line model (5a), and m and n minimizing

$$e = \Pi_{meas} - \left(1 - \left(\frac{\dot{m}_{c,corr,J} - c_4}{c_3 - c_4}\right)^{c_1}\right)^{\frac{1}{c_2}} c_5 \tag{27}$$

where $\dot{m}_{c,corr,J}$ is given by (18).

The result is presented in Table 5, and shows that the increase in fit to the speed line model, from allowing (r, s) to vary, is minimal. The deviations in (r, s) from standard values $(r = 0.5, s = 1)$ are large for the small shaft speed. The large shaft speed shows smaller deviations in (r, s), compared to the standard values. The estimated r with best fit, for the small shaft speed, are negative, while positive for the large shaft speed. These inconclusive results are connected to the high parameter sensitivity caused by the small slope of the speed lines, discussed in [14, 16].

A mass flow correction modification can also be analyzed, if the causality of (5a) is changed according to

$$\dot{m}_{c,corr,mod} = \left(1 - \left(\frac{\Pi_c}{c_5}\right)^{c_2}\right)^{1/c_1} \cdot (c_3 - c_4) + c_4 \tag{28}$$

and (18) is formulated as

$$\dot{m}_{c,mod} = \frac{\dot{m}_{c,corr,mod}}{\frac{\theta^r}{\delta^s}} \tag{29}$$

The error between the measured $\dot{m}_c$ and the modeled $\dot{m}_{c,mod}$

$$e = \dot{m}_c - \dot{m}_{c,mod} \tag{30}$$

Table 6: Change in fit of measured data to a speed line model (5a), for modified mass flow corrections (3), using the error e (30).

Corr.		r	s	mean($\|e\|$)	std(e)	$\sum(\|e\|)$
103869	I	0.5	1	0.0148	0.0184	4.07
	II	0.197	1	0.0144	0.0179	3.95
	III	0.5	0.611	0.0129	0.0160	3.56
	IV	-0.404	0.664	0.0121	0.0151	3.32

is used in the analysis. This corresponds to a horizontal translation of the measured points, in order for the points to better fit the speed line shape given by (5a).

Table 6 presents the result for the large shaft speed, since the investigation of the small shaft speed is too sensitive to initial parameter values, and is therefore discarded. The small slope of the speed lines, means that the horizontal translation in the map has to be large, to move a point close to the speed line modeled using (5a). The fit can be improved if $s < 1$.

5.3 High pressure stage data

Both the interstage data and the individual map data are measured for the same compressor in the gas stand. Therefore, compared to Section 5.2, this section investigates the corrections needed to minimize the vertical distance between the interstage speed lines and the speed lines of the individual map. Note however, that there are other inlet/outlet geometries associated with the two stage setup, for the interstage data, compared to the individual measured map. Different surrounding systems can lead to different compressor performance [8, 17, 18].

The parameters (d_1, d_0) of (22) are estimated using the individual hpc-map. Compared to Section 5.2, due to the large discrepancy between the individual hpc-map and the interstage map, the parametrization of (22) using the individual hpc-map can lead to substantial modeling errors for (21). The parameters (d_1, d_0) can be included in the parameter estimation, but this is discarded to avoid over fitting.

Further, since all speed lines from the interstage map have larger Π_c, investigating horizontal translation is neglected and only modifications to the shaft speed correction are investigated in this section.

Modifying the shaft speed correction

This section does not modify (3), and investigates potential gains in modifying (4) according to (17). A model of (21) according to (22), is used.

The objective is to minimize $e = \Pi_{mod} - \Pi_{corr}$. Each individual hpc map speed line is used to parametrize (5a), giving Π_{mod}. The individual hpc map can be used in the parametrization, independent of tested correction, since $\theta \approx 1$ and $\delta \approx 1$, for the individual hpc map, in combination with the structure of the tested corrections (17), as discussed in the ingress of Section 5. The speed line model fit to the individual map speed lines is excellent, which is expected since 5 parameters are fitted to the 9 data points. A good model fit is needed to

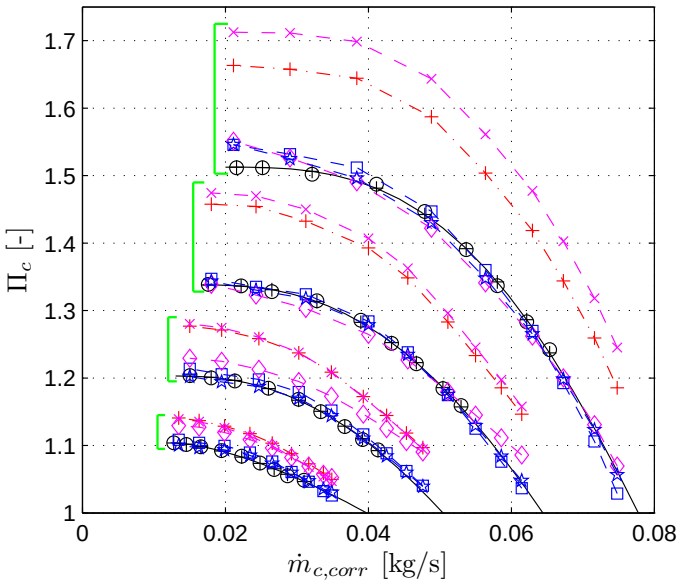

Figure 15: Resulting speed lines from modified shaft speed corrections (17) for the hpc-data. The Corrections I-IV are shown with: cross (I), square (II), diamond (III), and pentagram (IV). Plus represents the interstage speed lines, measured at constant N_{tc}. The individual hpc-map is shown with circles, and the solid line is the fit of the speed line model (5a). The square brackets indicate which lines that are comparable.

calculate Π_{mod} for the $\dot{m}_{c,corr}$ found in the interstage map, since the $\dot{m}_{c,corr}$ of the interstage map is larger than the $\dot{m}_{c,corr}$ found in the individual hpc map, and the model thus extrapolates the corresponding Π_c.

Π_{corr} is calculated using (23) with different parameters (m, n) in (17). The four Corrections I-IV presented in Section 5.2 are used in this investigation.

As seen in Figure 13, the interstage speed lines need to be shifted vertically downwards to minimize the distance to the individual map speed lines. Since (21) always is positive, a shift downwards is produced only if (24) is negative. Due to $\theta \approx 1$ and $\delta \approx 1$, for the individual hpc-map, $N_{tc,corr,sp}$ is readily found in the individual map, independent of shaft speed correction. Since $\theta > 1$ and $\delta > 1$ for the interstage map (see Table 3), the shaft speed corrections estimated are expected to be $m < 0$ and $n > 0$.

The result of modifying the shaft speed corrections for the hpc-data is presented in Figure 15, and Table 7 gives the numerical values. Correction I corresponds to, adjusting the measurements, using the default shaft speed correction (4). The line is shifted upwards, since the data is measured with $\theta > 1$. Note the close coupling between the (Ψ&Φ)-corrected dashed line in Figure 13 and Correction I marked with crosses in Figure 15. Correction I does not, however, adjust $\dot{m}_{c,corr}$. Corrections II and IV show $m < 0$ for all speed lines presented.

Since θ and δ are closer to unity for the smaller interstage shaft speeds (see

Table 7: The estimated parameters m, n using Corrections I-IV from Section 5.3, for the high pressure stage measurements. The small (δ, θ) of the interstage speed lines, see Table 3, combined with the large discrepancy between the individual and the interstage hpc-map give the large magnitudes of m and n. Estimated m is always negative.

N_{tc}	Corr.	m	n	mean($\|e\|$)	std(e)	$\sum(\|e\|)$
144597	I	0.5	0	0.1991	0.0076	1.7914
	II	-0.885	0	0.0177	0.0217	0.1589
	III	0.5	0.696	0.0134	0.0181	0.1205
	IV	-0.150	0.418	0.0107	0.0148	0.0967
118795	I	0.5	0	0.1244	0.0102	1.1192
	II	-1.856	0	0.0062	0.0072	0.0561
	III	0.5	1.543	0.0142	0.0192	0.1277
	IV	-1.391	0.350	0.0028	0.0033	0.0250
92959	I	0.5	0	0.0680	0.0062	0.6102
	II	-2.000	0	0.0088	0.0022	0.0796
	III	0.5	2.000	0.0362	0.0124	0.3261
	IV	-2.000	0.418	0.0032	0.0038	0.0289
67081	I	0.5	0	0.0299	0.0067	0.2691
	II	-2.000	0	0.0055	0.0044	0.0498
	III	0.5	2.000	0.0273	0.0020	0.2453
	IV	-2.000	1.548	0.0040	0.0035	0.0358

Table 3), the magnitude of m and n are larger for these shaft speeds. Since (21) is large for small shaft speeds (see Figure 14), a large $dN_{tc,corr}$ of (23) is needed to adjust the measurements, and thus a large exponent of the tested shaft speed correction quantities is needed. That is, if $T_{01}/T_{std} = 1.02$, a large m is needed to make any adjustment of the interstage measurement. The analysis of the smaller shaft speeds is therefore more sensitive to measurement errors, or an errors in the parameters (d_1, d_0) of (22), and the parameter estimations converge to the tested limits (-2 and 2).

6 Engine torque line with modified correction quantities

The same investigations of engine torque line versus altitude, as presented in Section 3.2, is presented here, with modified correction quantities. The change in altitude where the engine torque has to be reduced due to the limits, correlated to the safe compressor operation region, is discussed and quantified. The result is presented in Table 8, where the result from Table 1 is repeated in the first part of the table, to simplify the comparison. The next part of the table is calculated using adjusted shaft speed corrections and are discussed in the next section. The last part of the table use modified mass flow corrections and are discussed section following.

Table 8: Altitude where engine torque is reduced, due to the compressor limits (CS, TOS, Π_{max}) discussed in Section 3.2, for maps (A-H), shown in Figure 3. The first part repeats the results of Table 1 for convenience, followed by a part where the shaft speed correction is modified. The last part presents calculations using two modified mass flow corrections.

m/n	r/s	Map limits		(A)	(B)	(C)	(D)	(E)	(F)	(G)	(H)
std/std	std/std	CS	m	480	1240	230	460	1310	820	610	620
		TOS	m	2660	1900	1490	4040	2650	1150	390	2200
		Π_{max}	m	3840	3290	2550	5510	3030	4920	5210	5870
1/0.05	std/std	CS	m	490	1230	220	460	1350	860	610	610
		TOS	m	2450	1740	1360	3810	2430	1090	360	2110
		Π_{max}	m	3560	3080	2380	5030	2810	4500	4690	5280
1/0.7	std/std	CS	m	620	1220	170	380	1280	890	590	1030
		TOS	m	1140	740	540	1980	1150	560	90	1200
		Π_{max}	m	1890	1660	1280	2520	1490	2230	2240	2540
std/std	0.5/0.6	CS	m	330	830	200	390	810	560	450	500
		TOS	m	3100	2560	2000	4810	2680	2010	1030	3600
		Π_{max}	m	3680	3070	2400	5150	2960	4540	4710	5290
std/std	-0.7/1	CS	m	660	1810	240	520	1860	1110	760	720
		TOS	m	2380	1660	1320	3460	2480	970	330	1850
		Π_{max}	m	3900	3380	2630	5640	3070	5050	5370	6080

6.1 Modified shaft speed correction

The θ-exponent m of (17) is found to be slightly smaller than the standard value of $m = 0.5$ for the engine test stand measurements, and largely negative for the gas stand data. The negative values of m from the gas stand data are neglected, since no such clear trend is found in the more comprehensive engine test stand data. Further, the gas stand data contained only $\theta > 1$ measurements, while the engine test stand has $\theta \in [0.92, 1.08]$. The δ-exponent n of (17) is found to be between $n = 0.05$ for the engine test stand measurements, and $n = 0.7$ for the gas stand measurements.

Two combinations of (m, n): $(0.5, 0.05)$ and $(0.5, 0.7)$, are thus investigated. The resulting engine torque calculations are presented in the second section of Table 8. The calculations generally shows that, if also p_{01} is included in the shaft speed correction, through a non-zero n, a decrease in estimated engine performance with increasing altitude results.

$n = 0.05$-case

Compared to the case with nominal correction presented in the first section of Table 8, the low engine speed torque is not affected much, since the surge line is defined in Π_c and $\dot{m}_{c,corr}$. The map limits connected to the maximum corrected shaft speed, TOS and Π_{max}, are affected by the modification of shaft speed correction. Compared to the nominal case also map (E) is limited by the largest Π_c available before $h = 3000$ m is reached. High engine speed torque is severely affected by the modifications. It is only map (D) that can reach the

maximum torque for $N_e = 5000$ 1/min at $h = 3000$ m. If Table 8 is compared to Table 1, it can be seen that the largest altitude, where it is at all possible to reach maximum torque, is reduced by approximately $200 - 600$ m.

Larger n

For the case where n is increased to $n = 0.7$ from Table 7, an even worse estimated engine performance is found. The reduction in maximum corrected shaft speed coming from using (17) with a constant max N_{tc} gives severely restricted high altitude performance. The restriction comes mainly from the reduced maximum shaft speed, meaning that engine torque has to be reduced due to TOS and Π_{max}. The change in altitude for when CS restricts engine torque is much smaller, except for map (H).

6.2 Modified mass flow correction

For the mass flow correction, contradicting trends were found. Two different combinations of (r, s) are used in the analysis. The first case use $r = -0.7$ and $s = 1$ from Table 5. The second uses $r = 0.5$ and $s = 0.6$ from Table 6.

6.3 Modifying θ-exponent

A reduction in corrected mass flow results from reducing s in (18) from 1 to 0.6. This reduces the CS-limiting altitude, but increases the TOS-limiting altitude. This is so since the map operating points are moved left in the map, and thus closer to the surge line, and away from the TOS-line. The altitude where the Π_{max}-limit affects engine torque is also reduced for the maps studied.

6.4 Modifying δ-exponent

The large modification of (18), in going from a $r = 0.5$ of the standard mass flow correction (3), to a negative $r = -0.7$ increases the altitude for when CS restricts engine torque, since the operating point change in the map is away from the surge line. The TOS-limiting altitude is reduced by $50 - 600$ m, and the altitude when Π_{max} restricts engine torque is increased slightly compared to the altitude calculated using the standard mass flow correction.

7 Conclusions

The importance of having correct inlet condition correction for the compressor performance variables were discussed and motivated, especially for a two stage system where the correction quantities are large, due to large ratio between inlet and standard states. The additional increase in air filter pressure drop, due to the reduced ambient gas density with increasing altitude, was up to 50 %. The novel surge avoidance method presented, using the increase in corrected mass flow coming from a decrease in compressor inlet pressure, was shown to be applicable to increase the surge margin of eight compressor maps.

Engine test stand measurements showed a trend of decreasing Π_c for decreasing p_{01}, for two shaft speeds presented. No clear trends in Π_c was found for variations in T_{01}. A remarkable discrepancy existed between the interstage map and the individual map from the gas stand measurements. The interstage map have larger Π_c given a $\dot{m}_{c,corr}$, for all four speed lines presented.

An affine model in corrected mass flow was sufficient to model the sensitivity $dN_{tc,corr}/d\Pi_c$, given constant corrected mass flow, and could be used to adjust measured speed lines if the mass flow correction or shaft speed correction were modified. The sensitivity calculated for all eight maps showed largest values for the smallest corrected mass flow at the smallest shaft speed, and then decreased with increasing mass flow and corrected shaft speed. Further, the sensitivity was positive for all points in the eight maps.

Modifications to the standard mass flow and shaft speed corrections were presented and, using the proposed structure of the modifications, maps measured at standard conditions need no adjustment. A better fit to the measured maps, for both low pressure and high pressure stage, could be found if also compressor inlet pressure ratio δ was included in the shaft speed correction quantity. A good fit to the measurements was obtained if the factor $\delta^{0.05}$ was included in the shaft speed correction.

Already the small modification $\delta^{0.05}$ to the shaft speed correction, was shown to have large impact on an altitude dependent engine torque line. Reductions in engine torque were encountered at altitudes $200 - 600$ m below the altitudes calculated using the standard shaft speed corrections. Modifications to the mass flow correction, based on the measured data, also had large impact on engine performance limits.

References

[1] R. I. Lewis. *Turbomachinery Performance Analysis.* Arnold, 1996.

[2] SAE. SAE J1826 – Turbocharger Gas Stand Test Code. SAE standard, 1995.

[3] SAE. SAE J922 – Turbocharger Nomenclature and Terminology. SAE standard, 1995.

[4] ASME. PTC 10-1997, Performance test code on compressors and exhausters. American Society of Mechanical Engineers, New York, 1997.

[5] Edward S. Taylor. *Dimensional analysis for engineers.* Clarendon Press, Oxford, 1974.

[6] N. Watson and M.S. Janota. *Turbocharging the internal combustion engine.* MacMillan London, 1982.

[7] J.B. Heywood. *Internal Combustion Engine Fundamentals.* McGraw-Hill series in mechanical engineering. McGraw-Hill, 1988.

[8] Jan-Ola Olsson. Boost limitation in a torque based engine management system. 5th IFAC Symposium on Advances in Automotive Control, 2007.

[9] Oskar Leufven and Lars Eriksson. Time to surge concept and surge control for acceleration performance. IFAC World Congress, Seoul, Korea, 2008.

[10] O. Leufven and L. Eriksson. Surge and choke capable compressor model. Submitted to IFAC World Congress, Milano, Italy, 2011.

[11] NASA. U.S. standard atmosphere, 1976. NASA standard, 1976.

[12] International Civil Aviation Organization. ICAO Doc 7488-cd – manual of the ICAO standard atmosphere (extended to 80 kilometres (262 500 feet)), ISBN 92-9194-004-6. ICAO standard, 1993.

[13] P. Andersson. *Air Charge Estimation in Turbocharged Spark Ignition Engines*. PhD thesis 989, Department of Electrical Engineering, Linköpings Universitet, Linköping, Sweden, 2005.

[14] Lars Eriksson, Lars Nielsen, Jan Brugård, Johan Bergström, Fredrik Pettersson, and Per Andersson. Modeling of a turbocharged SI engine. *Annual Reviews in Control*, 26(1):129 – 137, 2002.

[15] Merten Jung, Richard G. Ford, Keith Glover, Nick Collings, Urs Christen, and Michael J. Watts. Parametrization and transient validation of a variable geometry turbocharger for mean-value modeling at low and medium speed-load points. SAE Technical Paper 2002-01-2729, October 2002.

[16] O. Leufven and L. Eriksson. Engine test bench turbo mapping. SAE Technical Paper 2010-01-1232, 2010.

[17] G Benvenuto and U Campora. Dynamic simulation of a high-performance sequentially turbocharged marine diesel engine. *International Journal of Engine Reasearch*, 3(3):115–125, 2002.

[18] J. Galindo, H. Climent, C. Guardiola, and A. Tiseira. On the effect of pulsating flow on surge margin of small centrifugal compressors for automotive engines. *Experimental Thermal and Fluid Science*, 33(8):1163 – 1171, 2009.

[19] F. Westin and R. Burenius. Measurement of interstage losses of a twostage turbocharger system in a turbocharger test rig. SAE Technical Paper 2010-01-1221, 2010.

[20] J. Andersen, F. Lindström, and F. Westin. Surge Definitions for Radial Compressors in Automotive Turbochargers. *SAE International Journal of Engines*, 1(1):218, 2008.

A Nomenclature

Variables and parameters		Subscripts	
a, d	model parameters	01	compressor inlet
C_dA	effective area	02	compressor outlet
c_i	speed line model param.	af	air filter
$c_{i,j}$	compressor model param.	amb	ambient
e	error	c	compressor
h	altitude	$corr$	corrected
$\dot{m}$	mass flow	e	engine
m, n	model parameters	hpc	high pressure stage compr.
N	speed	ic	intercooler
p	total absolute pressure	im	intake manifold
r, s	model parameters	lpc	low pressure stage compr.
R	gas constant	max	maximum
T	total absolute temperature	$meas$	measurement
Γ	quotient of pressure ratios	mod	modeled
γ	ratio of specific heats	ref	reference
δ	inlet temperature ratio	sig	significant
η	adiabatic efficiency	sp	set points
θ	inlet pressure ratio	std	standard
Π	pressure ratio	tc	turbocharger
Φ	Dimensionless flow param.		
Ψ	Head coefficient		

B Derivation of $\left.\frac{dN_{tc,corr}}{d\Pi_c}\right|_{\dot{m}_{c,corr}}$

The sensitivity $\left.\frac{dN_{tc,corr}}{d\Pi_c}\right|_{\dot{m}_{c,corr}}$ is used in Section 5, and is interesting since it gives information about how a change in $N_{tc,corr}$ is connected to a change in Π_c. Defining $\tilde{f}$ using the Ellipse model structure (5a-f) gives the following $\tilde{f}$

$$\tilde{f} = \Pi_c - \left(1 - \left(\frac{\dot{m}_{c,corr} - c_4}{c_3 - c_4}\right)^{c_1}\right)^{1/c_2} c_5 = 0 \tag{31}$$

where $c_i(N),\ i \in [1, 5]$. With $\frac{\partial \tilde{f}}{\partial \Pi_c} = 1$, and using $d\dot{m}_{c,corr} = 0$, (20) becomes

$$1 \cdot d\Pi_c + \frac{\partial \tilde{f}}{\partial N_{tc,corr}} dN_{tc,corr} = 0 \tag{32}$$

which gives the following expression for (21)

$$\left.\frac{dN_{tc,corr}}{d\Pi_c}\right|_{\dot{m}_{c,corr}} = -\frac{1}{\frac{\partial \tilde{f}}{\partial N_{tc,corr}}} \tag{33}$$

Defining the following functions

$$K(N_{tc,corr}, \dot{m}_{c,corr}) = \frac{\dot{m} - c_4(N_{tc,corr})}{c_3(N_{tc,corr}) - c_4(N_{tc,corr})} \tag{34}$$

$$H(N_{tc,corr}, \dot{m}_{c,corr}) = 1 - K^{c_1(N_{tc,corr})} \tag{35}$$

$$G(N_{tc,corr}, \dot{m}_{c,corr}) = H^{1/c_2(N_{tc,corr})} = \Pi_c / c_5 \tag{36}$$

and the derivative is then calculated according to

$$-\frac{\partial \tilde{f}}{\partial N_{tc,corr}} = \frac{\partial c_5}{\partial N_{tc,corr}} G + c_5 \frac{\partial G}{\partial N_{tc,corr}} \tag{37}$$

We now have

$$\frac{\partial G}{\partial N_{tc,corr}} = G \left(-\frac{1}{c_2} \frac{\partial c_2}{\partial N_{tc,corr}} \ln(G) + \frac{1}{c_2 H} \frac{\partial H}{\partial N_{tc,corr}} \right) \tag{38}$$

$$\frac{\partial H}{\partial N_{tc,corr}} = -K^{c_1} \left(\frac{\partial c_1}{\partial N_{tc,corr}} \ln(K) + \frac{c_1}{K} \frac{\partial K}{\partial N_{tc,corr}} \right) \tag{39}$$

with

$$\frac{\partial K}{\partial N_{tc,corr}} = \frac{\frac{\partial (\dot{m}_{c,corr} - c_4)}{\partial N_{tc,corr}} (c_3 - c_4) - (\dot{m}_{c,corr} - c_4) \frac{\partial (c_3 - c_4)}{\partial N_{tc,corr}}}{(c_3 - c_4)^2} \tag{40}$$

where $\frac{\partial \dot{m}_{c,corr}}{\partial N_{tc,corr}} = 0$ gives

$$\frac{\partial K}{\partial N_{tc,corr}} = \frac{(c_4 - \dot{m}_{c,corr}) \frac{\partial c_3}{\partial N_{tc,corr}} - c_3 \frac{\partial c_4}{\partial N_{tc,corr}}}{(c_3 - c_4)^2} \tag{41}$$

Combining (38)-(41) and inserting it into (37) together with the partial derivatives of the basis functions $c_i,\ i \in [1, 5]$ from (5b-f) gives the following

$$\begin{aligned} -\frac{\partial \tilde{f}}{\partial N_{tc,corr}} = c_{5,1} c_{5,2} N_{tc,corr}^{c_{5,2}-1} G - \frac{\Pi_c}{c_2} \Bigg[& c_{2,1} c_{2,2} N_{tc,corr}^{c_{2,2}-1} \ln(G) \\ & + \frac{1}{H} K^{c_1} \Bigg(c_{1,1} \ln(K) \\ & + \frac{c_1}{K} \frac{(c_4 - \dot{m}_{c,corr}) c_{3,1} - c_3 c_{4,1} c_{4,2} N_{tc,corr}^{c_{4,2}-1}}{(c_3 - c_4)^2} \Bigg) \Bigg] \end{aligned} \tag{42}$$

which now can be used to calculate $\frac{dN_{tc,corr}}{d\Pi_c}\Big|_{\dot{m}_{c,corr}}$.